Abstract

Title: Calibration of Analog Sensors for the alignment of muon chambers in the CMS experiment.

Author: Marion Ripert

Major Advisor: M.Hohlmann, Ph.D.

The CMS experiment at the Large Hadron Collider requires a continuous and accurate monitoring of the position of muon chambers on the muon Endcap. Wire extension and linear motion potentiometers, and inclinometers will monitor the movement of CMS muon chambers for the purpose of alignment. These results have important implications for the corrections in the reconstruction of muon tracks. It is therefore important to ensure a high accuracy in the correlation between the Sensor Response and the distance moved a given sensor. For this thesis project, a semi-automated calibration bench was developed for all sensors. LabVIEW based control and readout system, troubleshooting, and calibration procedure and achieved precisions, as well as first calibration results are discussed.

Table of Contents

List of Figures

List of Tables

Acknowledgments

I would like to express my gratitude and my appreciation to Dr.Hohlmann for supervising this research, providing financial assistance, and serving as my thesis advisor.

My gratitude goes out to my committee members, who took time for their busy schedules to assist me, and I would especially like to thank Dr.Mantovani for his scientific and technical advice and his patience during the proofreading of the manuscript. Also, I would like to thank Dr.Baksay for encouraging me to do research. I will always remember as cheerful in disposition, and forever kind.

Particular appreciation is extended to Dr.Caraway whose support was vital to this project in the design of the experimental apparatus. Technical assistance, scientific consultation and advice were also provided by: David Eartly, Jim Gering and Vladimir Sknar.

A special thanks to Klaus Dehmelt, Samir Guragain, Georgia Karagiorgi and Thomas Moschoutis for their friendship and invaluable contribution to this project.

Last, but certainly not least, the author would like to express thanks to her family and to her friends for their moral support, without which this research would not have been possible.

To my parents and family, for all of your encouragements

Chapter 1 Overview

1.1 Introduction

Our knowledge of the Universe and of elementary particles is incomplete. The best classification of the elementary particles is called the Standard Model. This Standard Model has been checked for example by experiments at CERN and Fermilab. However, many questions such as the origin of the masses of the particles, the unification of the weak force and the strong force haven't been yet resolved. These mysteries affect our comprehension of the universe, such as the fact that there is another particle or substance under which more than 2/3 of the mass of the cosmos hide.

The work presented here is concerned with the alignment of the Cathode Strip Chambers in the detector named Compact Muon Solenoid. The CMS like 4 other experiments is associated with the Large Hadron Collider, an accelerator of protons. The topic of my research is the analog sensors and their calibration. My task has been to develop a semi-automated bench for the calibration of these various sensors.

1.2 Introduction to Particle Physics

Particle physics studies the basic components of matter, their properties as well as the forces controlling them. The standard model contains this theoretical knowledge. The three types of interactions (electromagnetic, strong and weak) are described by the quantum field theory in which the particles are modeled by fields. All these forces arise from the same principle of invariance known as the Gauge principle. In these theories, the forces are exerted on the fermions (electrons, neutrinos, quarks...) by the exchange of bosons (photons, gluons, W and Z bosons). These last particles are often called "gauge particles ".

Each interaction (electromagnetic, strong and weak) associated with a field is due to the exchange of particles which are the quanta of the field (Table 1.2). For example, the electromagnetic force is associated the exchange of photons. The other intermediate bosons are: eight varieties of gluons (strong interactions), W and Z bosons (weak interactions). The standard model (Table 1.1) describes 2 types of particles (or field): Fermions which are particles of spin ½; Gauge bosons which are particles of spin 1 (W, Z, photon and gluons).

FORCE	RANGE	ACTION ON	Exchange Particle	Manifestation s
Electromagnetic	Infinity	any charged particle	Photon	Light, atoms, molecules, chemical reactions
Strong	10^{-13} cm	Quarks,	Gluons	Protons, neutrons, nuclear reactions
Weak	10^{-16} cm	Quarks, Leptons	W, Z Boson	Disintegration of neutrons, diffusion of neutrinos
Gravity	Infinity	All	Graviton	Planets, stars, galaxies, cosmology

Table 1.1: Table of the four fundamental forces [1]

QUARKS		LEPTONS		Generations
up	down	e - neutrino	elect	I
charm	strange	μ - neutrino	muo	II
top	bottom	τ - neutrino	tau	III

Table 1.2 Table of Fermions [2]

The quarks u and d as well as the electron constitute the fundamental particles of the known stable matter. The particles of generations II and III, replica of the fundamental particles with higher masses, were discovered due to collisions at high energy. However, these replicas cannot be components of the normal matter because they are unstable. Why does Nature propose two replicas of the fundamental particles?

The standard model is far from satisfactory since it explains "theoretically" why the majority of the particles have a mass, or the differences between these masses by the Higgs mechanism but physicist haven't yet discovered the Higgs boson experimentally. Electromagnetism and β-decay are different demonstrations of the electroweak force. However, the mass of the particle associated with electromagnetism, the photon, is zero whereas the particles connected to the radioactivity, the bosons W and Z, have enormous masses, close to that of a large atom. The standard model advances the assumption of a new field called the Higgs field. This field pervades all space and explains the mass of the photon and bosons Z and W. Photons have a zero mass since they don't interact with this field, as opposed to the W and Z bosons which have enormous masses (91 GeV). The Higgs boson, the missing part of the standard model, would produce a mechanism for generating a mass for each particle of the standard model.

Among the unsolved problems is the existence of the graviton. The standard model describes the force of gravitation by the exchange of a boson mediator called the graviton. The graviton should be the equivalent of the photon in a still non-existent theory of the quantum gravitation. The detection of the graviton is for the moment a challenge for physicists!

1.3 CERN: The world's largest particle physics laboratory

One of the four experiments associated with the Large Hadron Collider at CERN is the Compact Muon Solenoid which has, among other objectives, to discover Higgs boson. CERN, the European Organization for the Nuclear Research, was created in 1954 by a convention of 12 European states. Today, CERN is composed of 20 member states and 8 observer states. CERN was founded with an aim of building a laboratory having the most advanced scientists and technical resources. The accelerators and the detectors are the tools necessary for the physicists to study the basic components of our universe.

1.3.1 The Large Hadron Collider is a proton - proton collider

Two types of experiments can typically be conducted: the collision of particles with a fixed target or the head-on collision with a similar beam of opposite direction (Figure 1.1)

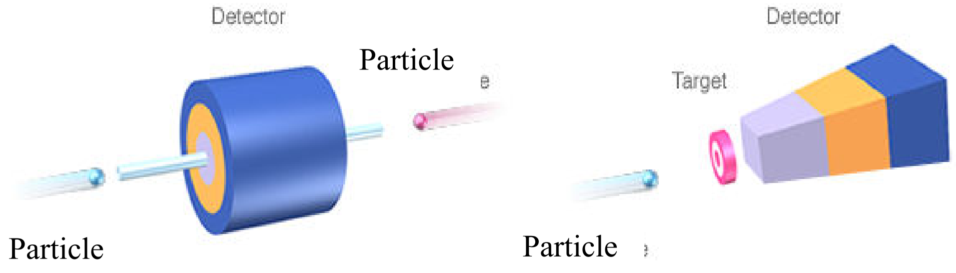

Figure 1.1 Collider experiment versus head-on collision [2]

The detectors localize and identify particles. To discover new particles, physicists use high energy at the time of the collisions by bringing the particles to speeds increasingly close to that of light. This increase in energy allows probing matter more and more closely. In order to provide all the energy supplied to an interaction, a head–on collision is used, because the collisions on a fixed target present the disadvantage that a part of the energy of the beam is lost to the displacement of the centre of mass. In the collision of two similar beams but of opposed directions, all energy is used for the production of new particles.

For the moment the Tevatron in Fermilab is the collider with the highest energy. It collides protons with anti-protons with energies of a little less than 2 TeV at the centre of mass. The Large Hadron Collider will collide beams of protons at a center of mass energy of 14 TeV. The LHC will be the accelerator with the highest energy and with the highest "bunch crossing frequency" (40 million times per seconds).

1.3.2 The Compact Muon Solenoid

The acronym CMS means "Compact Muon Solenoid " (Figure1.2). The name summarizes the essential characteristics of the instrument. The compact muon solenoid emphasizes the identification of muons.

The detector includes a magnetic system to facilitate the measurement of the momentum of the charged particles. CMS will use a large superconductive solenoid of 4 Teslas (approximately 100000 times the magnetic field of the Earth), 13 meters length, and radius of 2.95 meters. In each collision, called an event, each sub-detector recognizes and measures the various particles according to their charge, their momentum and their energy. Two main types of sub-detectors are used: Tracking Chambers measure the path of the charged particle. Calorimeters measure the energy lost by a particle that goes through it.

In general, a detector presents four structures laid out in the following way: a first set of tracking chambers then two sets of calorimeters and finally a second unit of tracking chambers, each particle leaves a different trace in this detector (Figure 1.3).

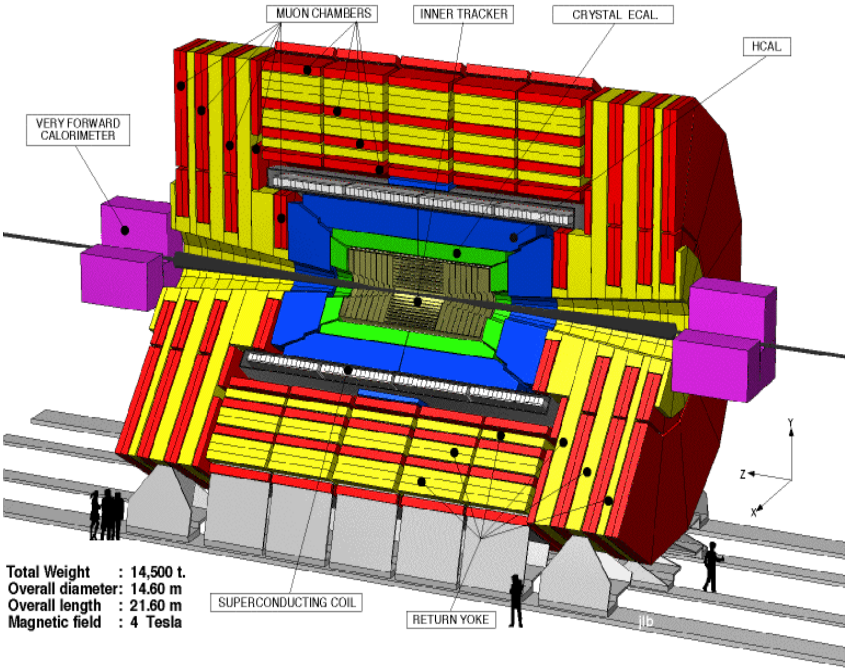

Figure 1.2 The Compact Muon Solenoid [2]

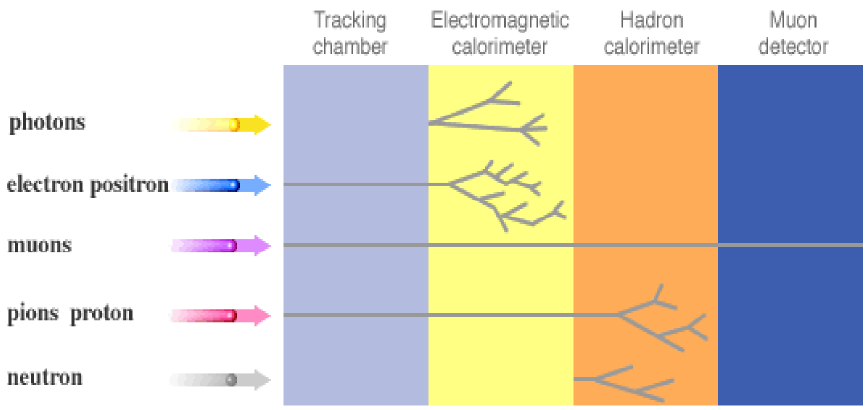

Figure 1.3 The different components of a detector [2]

A muon is a particle which passes through calorimeters without interacting much, but which leaves a track of its passage in the internal and external tracking chambers. This is why the external detector is called a Muon detector.

Electrons leave a signal in the inner detectors then deposit their energy in the electromagnetic calorimeter, whereas photons do not leave any trace in the internal detectors, but deposit their energy in the electromagnetic calorimeter.

Charged Hadrons ($K^{\pm}$, $\pi^{\pm}$ ...) leave a signal in the inner detectors then deposit their energy in the hadronic calorimeter; few neutrons are produced in the proton-proton collision, but they deposit energy in the hadronic calorimeter.

A particle which emerges from the collision will meet first the tracking system made of silicon detectors (pixels and strips). The positions of the particles crossing them will be measured with precision, which will be used for the reconstruction of the trajectory. The first layer of calorimeter (the electromagnetic calorimeter) is designed to measure electrons and photons.

Hadrons, participating in the strong interaction, deposit their energy in the hadron calorimeter (HCAL). Muons crossing HCAL without stopping are then tracked by muon chambers in the Barrel and the Endcap (Figure 1.4).

Neutrinos, barely interacting, will escape from all direct detections. Some of the data will account for their presence: while adding all the momentum of all the particles detected by the CMS, the physicists can determine where the neutrinos passed.

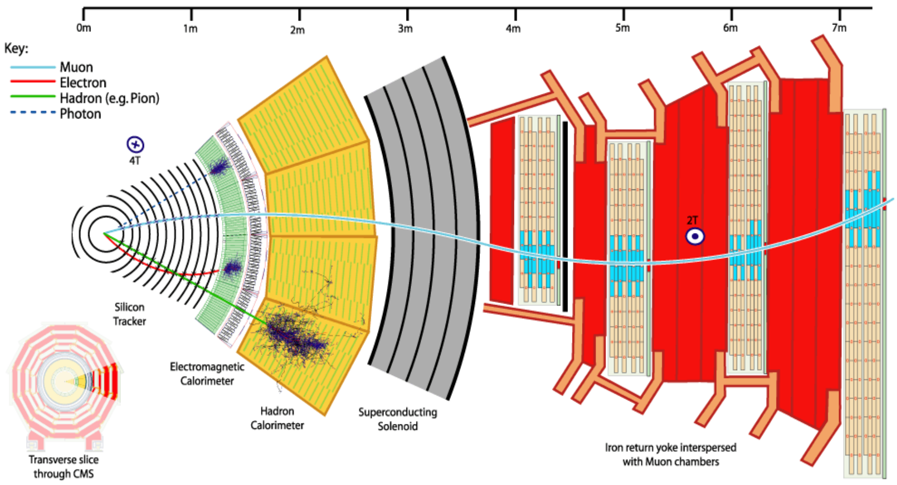

Figure 1.4 A view of the particle track after collision [2, 3]

The Compact Muon Solenoid, situated 100 meters underground, will be operational for at least 11 years. For that, a perfect resolution of the position of the Cathode Strip Chambers in the Endcap (and also in the Barrel) and long-term stability are necessary. Various types of sensors (linear movement, angular movement) will be installed on the CSC and calibrated before. The study of the tolerance and the repetition of the reading of the sensors will improve the estimate of the position of the CSC which will be used in the reconstruction of the tracks followed by the particles.

Particle detectors cannot really "see" the particle. Physicists use tracking chambers in order to make visible the traces of the particles (Figure 1.5). There are several old types of tracking chambers: bubble chambers, cloud chambers, spark chambers. The majority of the modern tracking chambers produce weak electronic signals which are recorded in a data base. A computer makes it possible thereafter to reconstruct the traces and to display them on a screen.

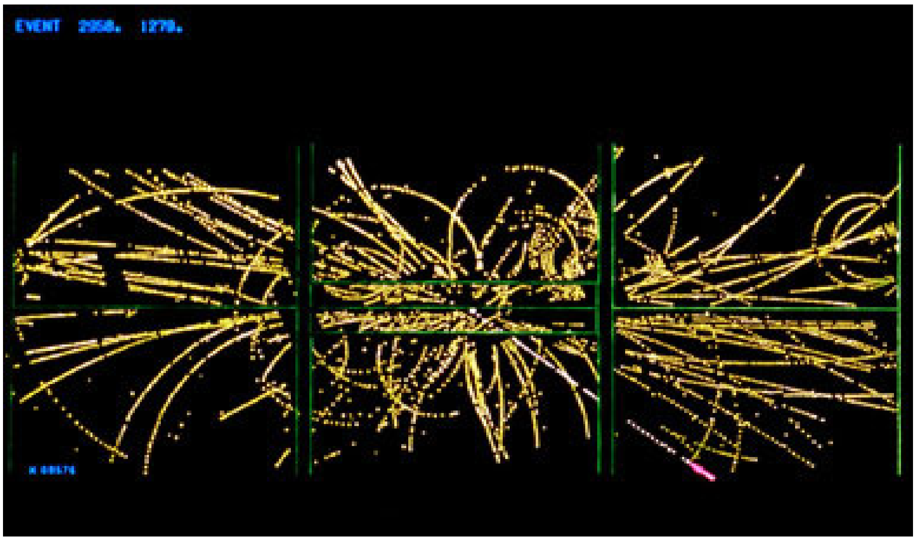

Figure 1.5 One example of the reconstruction of the paths of particles [2]

The trace of the particle provides much information such as the charge of the particle and the momentum of the particle. Tracking makes it possible to distinguish the particles with high momentum, propagating in straight lines, and the particles with weak momentum, creating tight spirals.

To obtain more information, a calorimeter is associated with a tracking chamber. Calorimeters are very important since they measure the energy by stopping and absorbing completely most of particles produced in the interaction of the primary particle with the detector material. As described previously, Muons (but also neutrinos) often escape from a calorimeter (Figure 1.3). The CMS and the three other LHC detectors (ATLAS, LHCb and ALICE) are based on the model described above.

A solenoid is primarily a cylinder around which solenoidal electric wire is wound. The passage of an electrical current in the electric wire creates a magnetic field that curves the trajectory in the central barrel area. Most of the interesting events will produce one or more muons. The area of the Endcap of the CMS thus has as much importance as the area of the barrels. In the Endcap (Figure 1.6), the Muons are measured by the detection of particles track with the Cathode Strip Chambers.

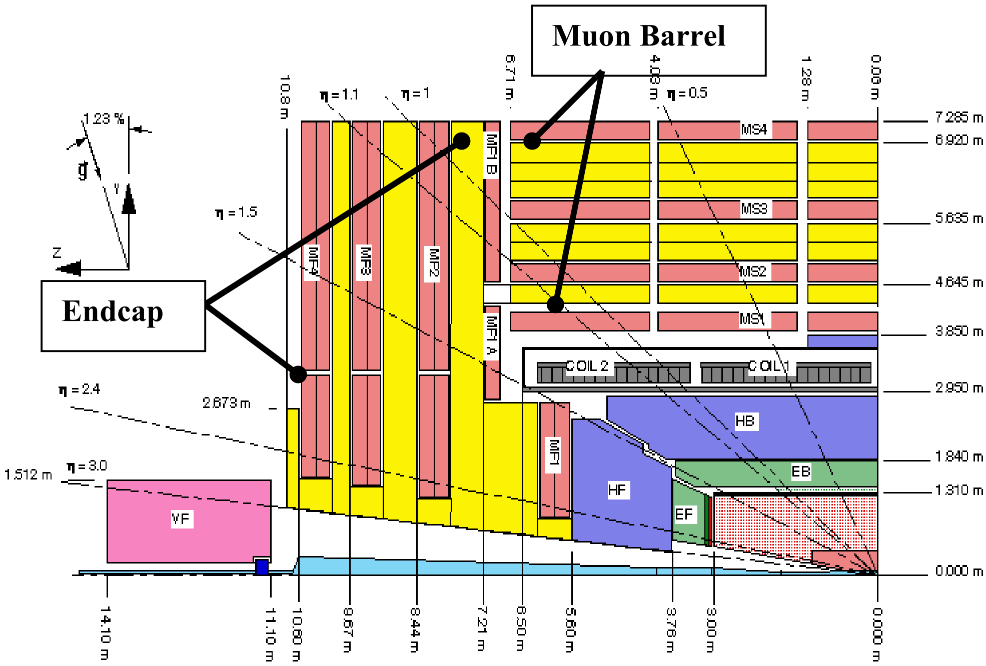

Figure 1.6 A longitudinal view of a quarter of the Compact Muon Solenoid [4]

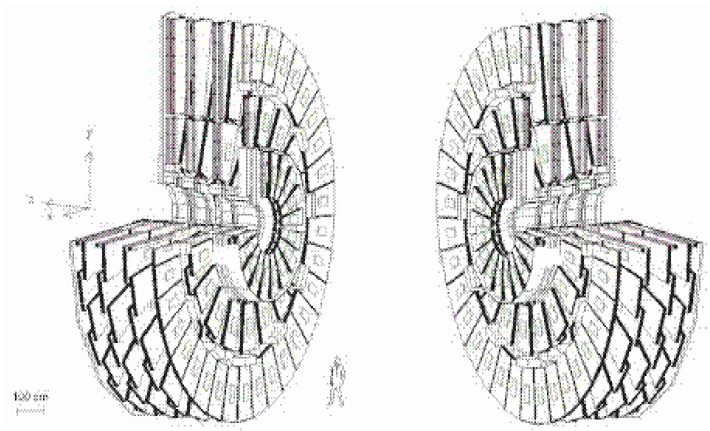

Figure 1.7 The Compact Muon Solenoid Endcap system [4]

1.3.3 The Cathode Strip Chambers on the CMS Endcap disks

The Cathode Strip Chambers (Figure 1.8) are designed as trapezoidal objects and laid out in four discs; they form the principal system of detection of the Muon Endcap, where the magnetic field is very intense, but inhomogeneous. Each CSC consists of 6 trapezoidal planes with a maximum length of 3.4 m for a maximum width of 1.5 m (Figure 1.9). The Endcap is made of four layers of chambers, placed behind the calorimeters and the coil, inserted into the big red disks called the iron yoke plates (Figure1.10), which return the magnetic field.

These layers are composed of three different types of detector:

Drifts tubes (DT) in the central part of the Barrel, Cathodes Strip Chambers (CSC) in the Endcap and Resistive Plates Chambers (RPC) in the Barrel and the Endcap. DT and CSC are used to obtain a precise measurement of the position – i.e. the momentum of the muons - whereas the RPC provide fast information (a few nanoseconds) used for the first level of triggering.

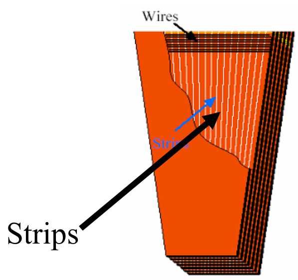

Figure 1.8 A Cathode Strip Chamber composed of anode wires and strips [5]

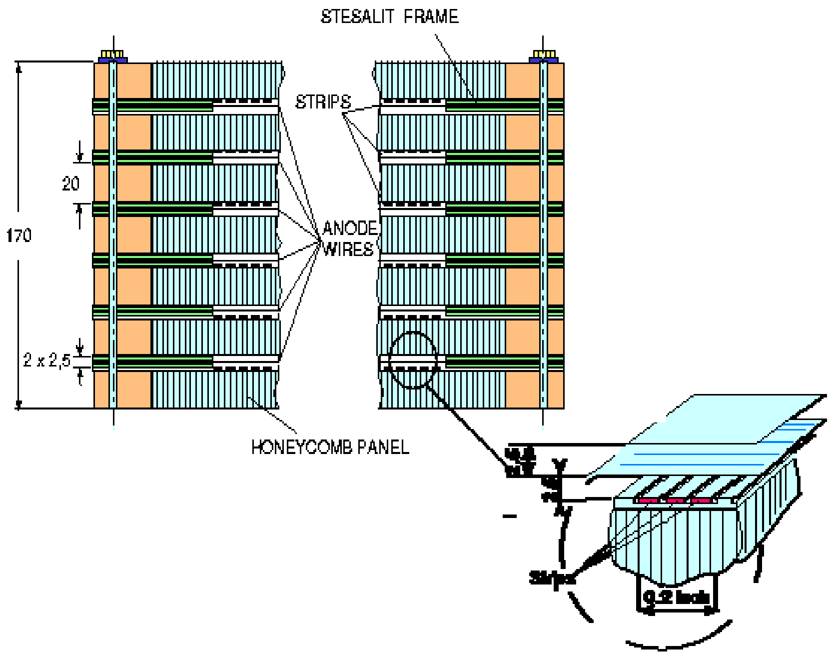

Figure 1.9 A close up view of a Cathode Strip Chambers [5]

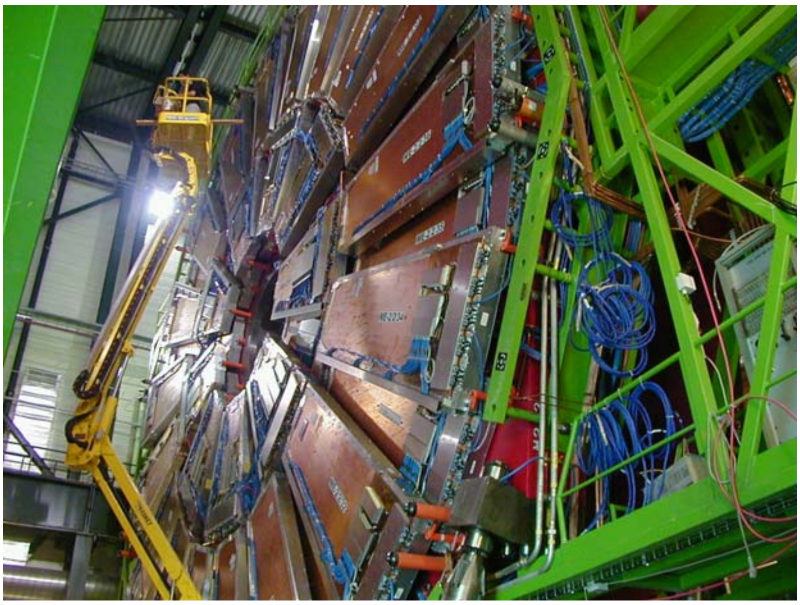

Figure 1.10 Fifty-four Cathode Strip Chambers installed on the ME+2 disk of the CMS detector [2]

The position of the Cathode Strip Chambers on each disc (ME±2, ME±3, and ME±4) forms two concentric rings: the inner and outer ring composed successively of 18 and 36 chambers, respectively. Disc ME±1 is made of three rings of 36 chambers (Appendix A). The chambers overlap so that 100% of the volume of the detector is covered to detect the track of the incident particles. The supports of muon chambers on the 15 m diameter Endcap yoke disks are positioned to an accuracy of 0.2 mm.

1.3.4 Composition of Cathode Strip Chambers

The Cathode Strip Chambers are proportional chambers made up of a very large number of parallel anode wires. Each wire acts like an individual detector. A muon passing through a chamber will produce a signal on the nearest wire. This signal will be proportional to the amount of ionization created (Figure 1.11).

In these multi-wire chambers, the plane of the cathode is segmented in strips orthogonal to the anode wires. When a muon crosses the CSC, the atoms of the gas are ionized. The atoms split into a negatively charged electron and a positively charged ion. The electrons released in the gas migrate towards the area of the wire whereas the ions migrate towards the cathode (Figure 1.12).

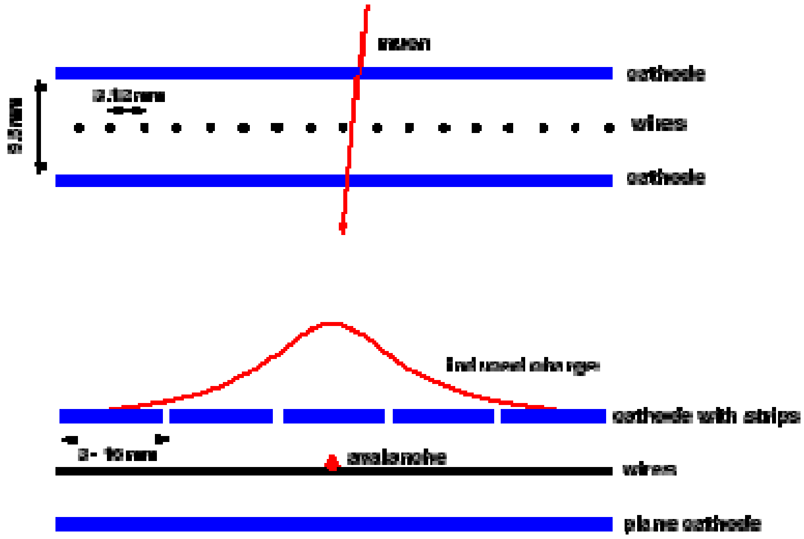

Figure 1.11 The process of ionization by collision is the basis of avalanche multiplication [6, 7]

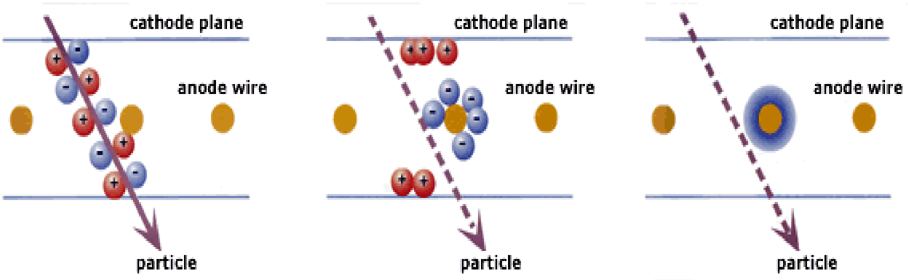

Figure 1.12 Avalanche Multiplication [6,7]

The higher the electric field is, the greater the electrons will move towards anode wires causing more ionized gas and more released electrons. These new free electrons which in their turn ionize gas and create new electrons generate an "avalanche" of electrons. This avalanche, developed around the anode wire, indicates the passage of the particles by inducing a charge in the field of the cathode, allowing a reading in two dimensions.

Chapter 2 Experimental Details

2.1 Sensors

Sensors are devices (electronic, mechanical, optical...) which can translate a movement, a light, a frequency into an electric signal. This electric signal will be used for calibrating the sensors. The various sensors used for aligning the CSCs are mechanical sensors indicating a linear displacement or an angular displacement. The analog electric signal is extracted from a linear movement applied to the sensors, which is also of an analog type.

2.1.1 Potentiometric sensors: principle of operation

The resistive track is placed on the fixed part of the sensor and the mechanical movement is coupled with a wiper which moves on the fixed part. The displacement of a sensor moves the wiper of a potentiometer (Figure 2.1). Thus, resistance (or voltage) between a fixed point and the moving part of the potentiometer is a function of the position to be measured.

The main component (Figure 2.2) is the element influenced by the linear movement of the stepper motor which is transformed into an intermediate electric signal, interpreted by the sensing device of the sensor. In the case of a linear potentiometer of type R (Figure 2.3), the main component of the sensor is the capstan associated with the axis of rotation of the sensor.

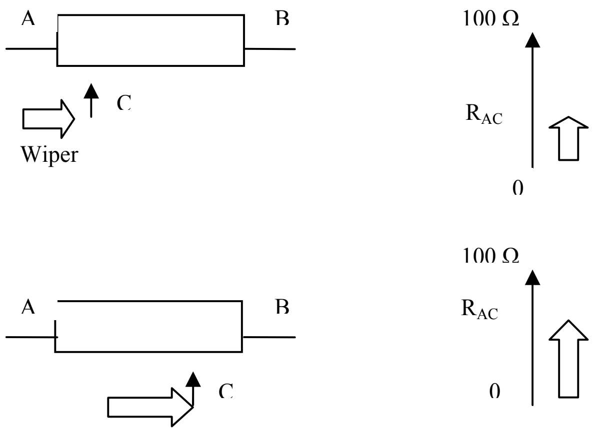

Figure 2.1 Potentiometric displacement sensor [8]

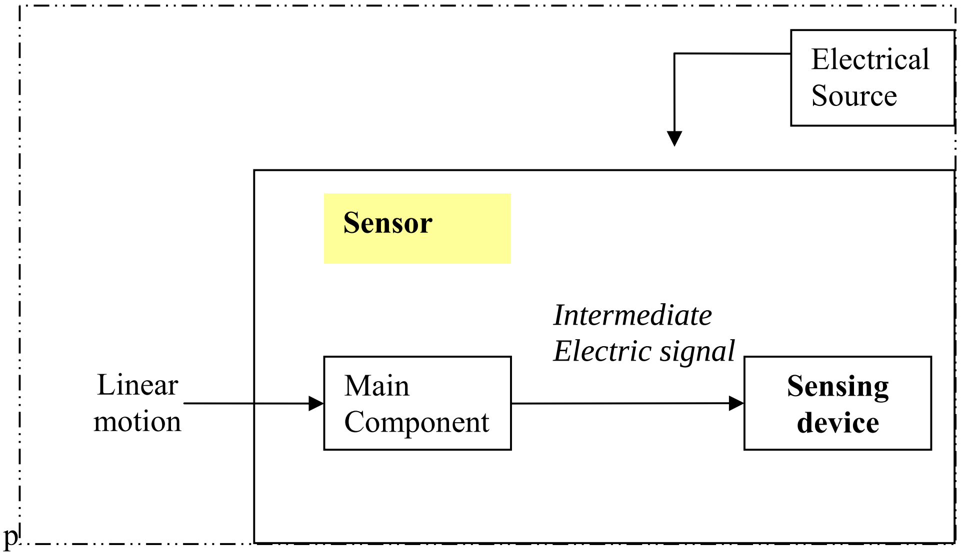

Figure 2.2 Operation of a sensor [8]

2.1.2 Linear position sensors

The linear position sensors are rectilinear potentiometers. Two types of linear potentiometers are calibrated:

2.1.2.1 R Sensors - Wire extension potentiometers

They consist of a stainless steel displacement cable placed around an internal capstan that is directly coupled to a precision potentiometer (Figure 2.3). Operationally, the extension cable is attached to a moving table (Figure 2.4) and, the position transducer is mounted in a fixed position.

As movement occurs, the cable extracts and retracts rotating a capstan and sensing device that produce an electric signal proportional to the linear extension of the cable. The tension on the wire rope extension is maintained with an internal spring.

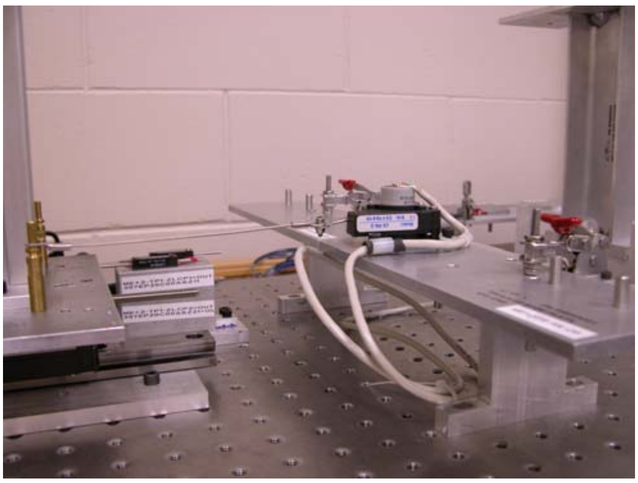

Figure 2.3 Wire extension potentiometers

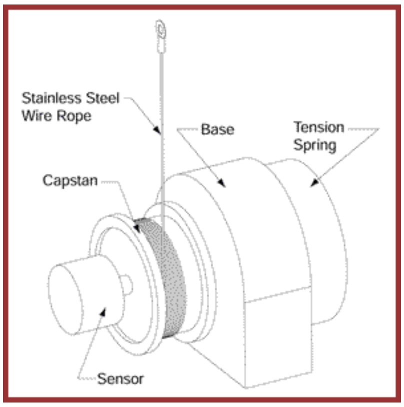

Figure 2.4 Structure of R sensor [9]

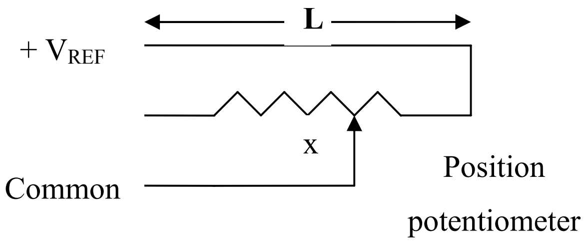

Figure 2.5 Circuit Diagram [9]

According to their electrical source, one distinguishes between active and passive sensors. The three types of sensors used are passive sensors because they require an external source of energy. An internal spring maintains the tension on the cable and is used as a mechanism of retraction.

The circuit diagram (Figure 2.5) describes a potentiometer with 3 terminals. The specific sensor used is the model LX - PA-2 which has an effective linear range of 50 mm. The specified accuracy of the LX-PA-2 sensors measured as a percentage of the full scale of measurement ± 1.0%.

When the sensors will be positioned on the Cathode Strip Chambers, the scientists and engineers will be interested to obtain the "absolute" position.

Two types of R sensors are used in the alignment system of the Endcap. R1 sensors provide the connections between inner (IN) and outer (OUT) ring of Cathode Strip Chambers (Figure 2.6) whereas the R2 sensor connects the outer ring of CSCs to the transfer plate, which is the mechanical connection between R and Z coordinates (Figure 2.7).

The wire rope is attached to a fixed point called R-Post (Figure2.7). When movement occurs in the detector, in order to know the absolute position of each CSC with respect to the transfer plate or another CSC, each R1 and R2 sensor is positioned on a plate or raised tower with respect to a referenced dowel pin on that plate or tower. These sensors will give the radial distance of the Cathode Strip Chamber (referenced by a dowel pin) compared to the fixed R-post.

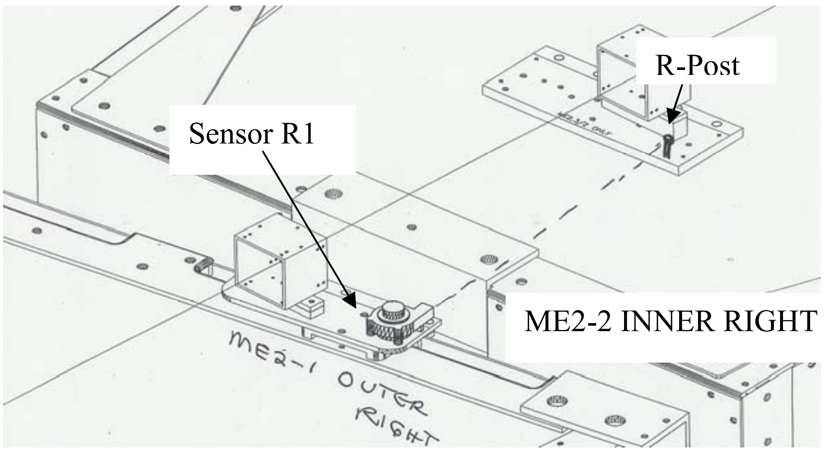

Figure 2.6 Close-up view - R1 sensor placed between the Inner Cathode Strip Chamber (ME+2-2) and the Outer one (ME+2-1) for the ME+2 disk. [10]

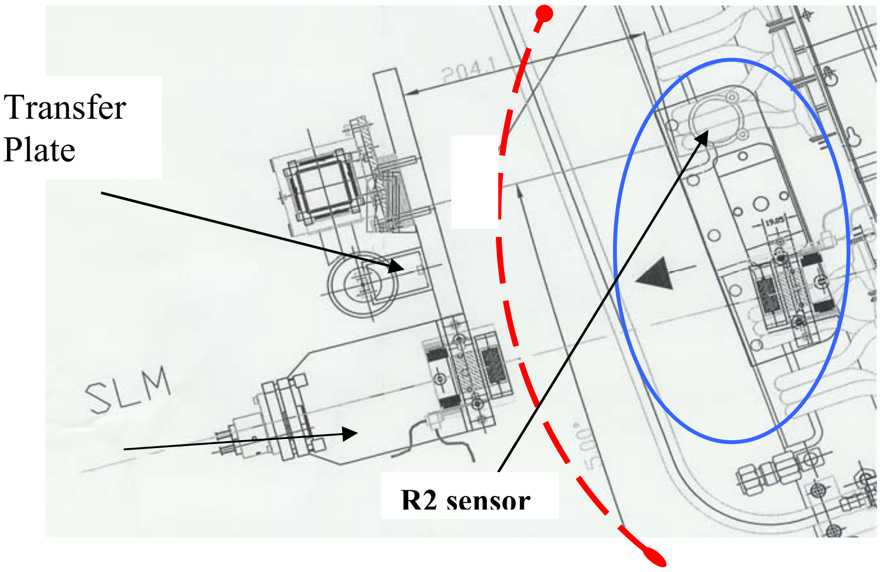

Figure 2.7 Close view of the position of R2 sensor between ME2/2 Outer and the Transfer Plate [10]

2.1.2.2. Z sensors

Z sensors (Figure 2.8) are linear potentiometers with high speed tracking conductive plastic providing good resolution. In order to forestall occasional shocks and vibrations a platinum alloy wiper composed of multi finger wipers is used. Series LCP8 refers to the smallest linear potentiometer characterized by a life expectancy estimated at 20 million strokes.

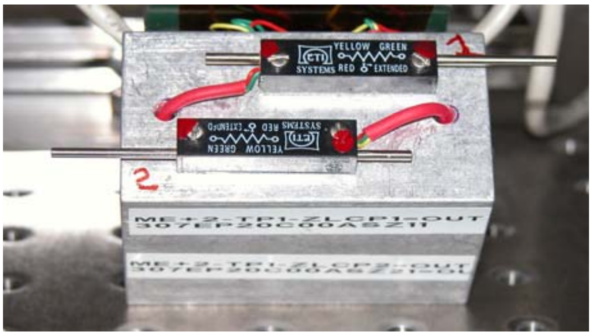

Figure 2.8 Linear potentiometer «Z» sensors. Model LCP8S-10-10K [11]

Theoretically, the electrical resistance of a material increases with length. As a slider is moved along the potentiometer, the displacement is deduced from the measurement of the resistance. A linear potentiometer is simply a voltage divider, with L being the total length of the resistor, and x being the displacement to be measured, as sketched in figure 2.5.

As displacement, x, changes, the slider moves along the resistor. Type LCP8 is characterized by a slider, guided by a rail and a stainless steel shaft (including a spring return). If we refer to Figure 2.9, the main component in this case is the conductive plastic provided with multi-finger wipers. Due to the movement of the slider on the conductive plastic, the platinum alloy is scraped on the conductive plastic (Figure 2.9). This alloy is selected for its long life and low noise. Additionally marked by an anti backlash wave washer and a durable plastic housing, this makes a powerful and stable potentiometer with a stroke length of 10 millimeters. These potentiometers are fairly accurate, but wear out eventually due to the physical contact at the slider. The contact point itself can be electrically noisy.

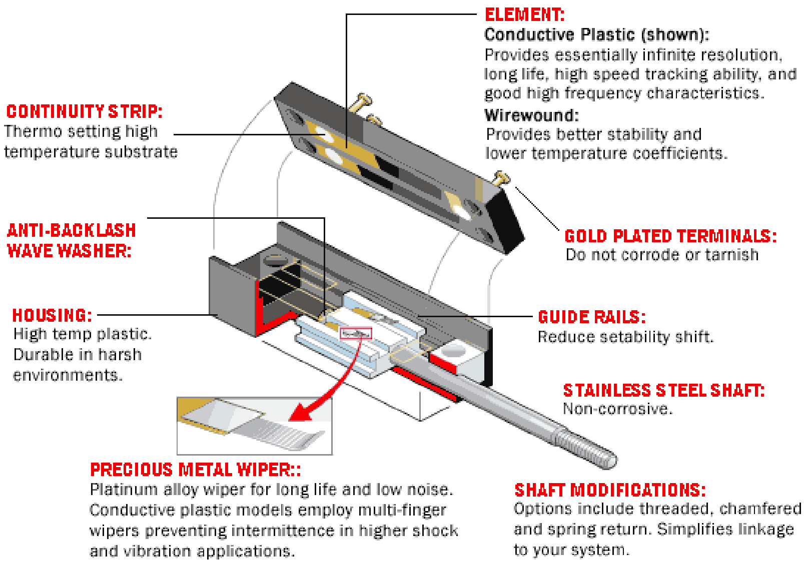

Figure 2.9 Construction of linear motion potentiometer LCP8S-10-10K [11]

Around each ME disk at six different positions, the Z coordinate is measured with these sensors. At the farthest end from the transfer plate, aluminum tubes touching Z sensors will record the Z coordinate for each EMU station.

2.1.2.3 Angular sensors – Inclinometers

The dual axial Model 900 H sensor (Figure 2.10), manufactured by Applied Geomechanics Incorporated (AGI) [12], is an inclinometer with wide range (±10 degrees) and is specified for high repeatability over 0.02 degrees of arc at constant temperature. This device measures angular position in two axes with a resolution of ±0.01 degrees using a precision electrolytic level sensor.

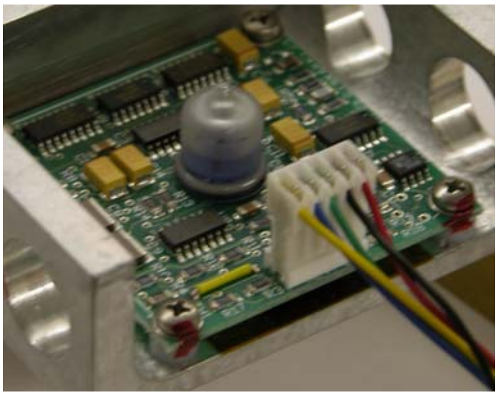

Figure 2.10 Inclinometers

As shown in figure 2.10, the sensing element is the glass half filled with a conductive liquid. When the “0” level is achieved the fluid covers 5 internal electrodes to equal depth. When the sensor is tilted, the depth of fluid on the 5 electrodes changes varying the resistance between pairs of electrodes. Electronics detect changes in resistivity between electrodes that are caused by motion of the gas bubble. This device converts these changes to a DC output that is proportional to the tilt angle.

Inclinometers measure angles with respect to the vertical gravity vector. The bubble, in the liquid glass case, will always orient itself perpendicular to the gravity vector.

Inclinometers are placed around each ME station at six different locations representing the six different types of clinometers (15º, 45º, 75º, -15º, -45º, -75º) which have to be calibrated for ME+2/-2/+3/-3/4/-4. However, three different types (20º, 40º, 60º) will be mounted for ME+1/2 and ME+1/-2.

2.2 Design of a semi-automated test bench

The objective is to calibrate angular and linear position response of the sensors. The calibration bench must be powerful and stable allowing a measurement of the sensors on the order of a few micrometers. Reproducibility of the calibration must be tested. Their repetitions and their improvements will require a complete and optimized Data Acquisition Solution for system monitoring, control and instrument characterization.

2.2.1 The concept of the calibration system

The objective is to calibrate the output response of these various analog sensors previously described and study the achievable absolute position resolution which is determined by the calibration uncertainty. After conditioning an analog signal through an analog interface card provided by Fermilab, the signal will be acquired by a DAQ Unit, Agilent HP 34970A, which converts the signal from analog to digital and transmits to a computer. With the software Igor-Pro, the signal will be analyzed.

All sensors mounted on their plate are screwed on their respective stand. A stepper motor drives the linear mover with a step size of 6 µm (Figure 2.11). As movement occurs, sensors in contact with the extension cable or with surface are calibrated. For the R sensors, the cable is attached to the fixed R post; as the stepper motor rotates, the cable is fed out and the potentiometer an electric output signal proportional to the prolongation of the cable.

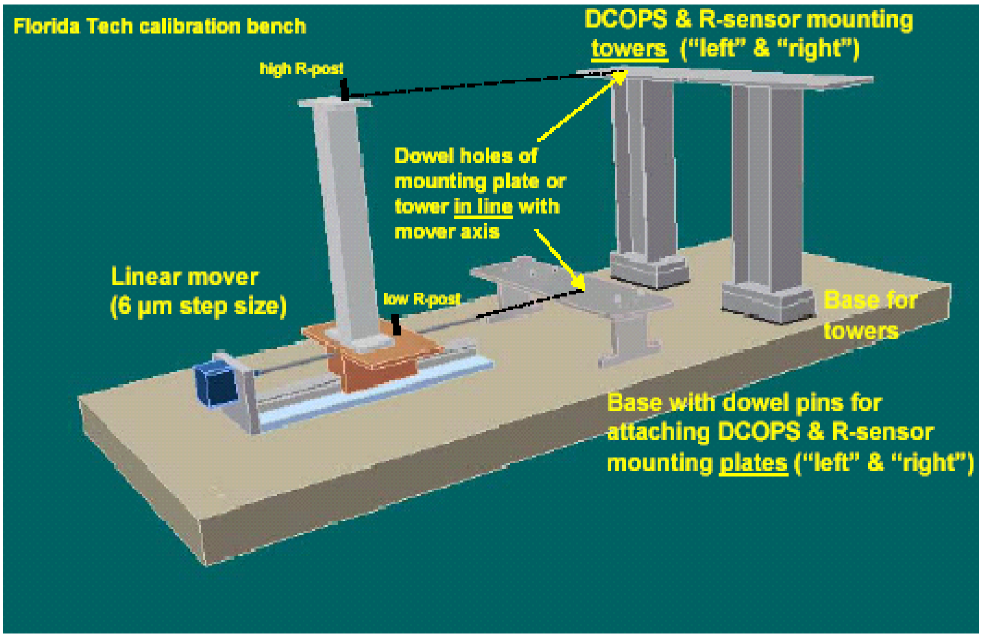

Figure 2.11 Florida Tech Calibration Bench

We must make certain that the instrumentation (Stepper motor, DAQ unit) we are using is calibrated. The DAQ unit has been operated through its 6 ½ digits resolution (Appendix C). The calibration of the stepper motor will be described in more details in the next section. Our calibration system provides an absolute measurement by quantifying for each individual distance and angular sensors the linearity of their output response and the corresponding calibration uncertainty.

2.2.2 The structure of the Acquisition System

As shown in figure 2.12, the analog signal acquisition is controlled by Virtual Instrumentation, with National Instruments (NI) data acquisition hardware. A National Instruments multifunction (E Series) Data Acquisition board was used for the control of the stepper motor. The acquisition of the output from the sensors is controlled by a National Instrument PCI-GPIB interface, an Agilent Data

Acquisition Unit (HP-34970A), and an analog board from Fermilab. Specifications of these components can be found in Appendix D-1.

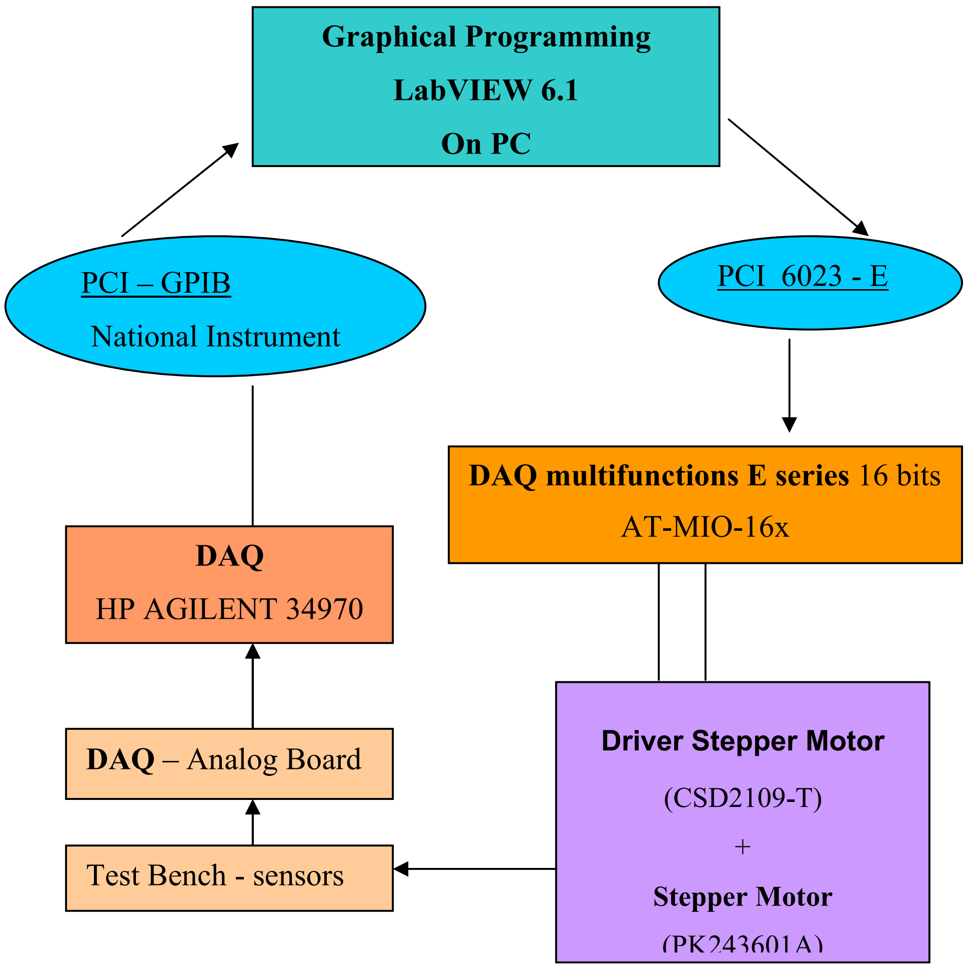

Figure 2.12 The Structure of the Virtual Instrumentation

The computer for the system is a 400MHz Pentium III, running Windows 2000, with a total of 256 MB of RAM. The stepper motor is controlled through the PCI 6023 E via the SCB-68 connector. All sensors are connected to the Fermilab analog board. The sensor response is digitized using the DAQ Agilent HP-34970A connected to the 34901A multiplexer channel which has a system speed of 60 channels/sec. The Agilent 34970A allows for data logging and transfer through 20 channels simultaneously via a PCI-GPIB interface, sufficient to transfer data at about 8 MB/s at maximum transfer rate. This instrument was acquired specifically for this purpose. Once the DAQ unit scans and loads the output sensor, the measurement process will start. All the measurement data is stored and analyzed using Igor Pro

2.2.3 Characteristic of PCI -6023 E

The PCI boards are "Plug and Play" analog, digital and timing I/O boards for the PCI bus computer. This board features 12 bit ADCs with 16 analog inputs, eight TTL compatible digital I/O, and two 24 bit counter/timers for timing I/O and up to 200kS/s sampling. The configuration and calibration of this PCI board is done via a National Instrument MITE bus interface chip that connects the board to the PCI I/O bus and implements the PCI local Bus specification.

Configuration and control of serial, GPIB, and also VXI instruments is achieved through an interface called VISA, the Virtual Instrument Software Architecture application programming interface(API). In our experiment, the PCI 6023 E board uses a device with a high resolution (12 bits ±0.5LSB) and the PCI-GPIB (Transfer Rate ~1 – 8 MB/s).

2.3 Structure of the Virtual Instrument

LabVIEW (Laboratory Virtual Instrument Engineering Workbench) is a commonly used software program developed by National Instruments [13]. LabVIEW uses a language based on “data driven dataflow” language plus additional “graphical control flow” such as loops.

2.3.1 Control Interface : LabVIEW

With LabVIEW, the main change is the appearance of virtual instrumentation which replaces part of the signal acquisition, processing, and display in traditional instruments, by computers. The front panel of your traditional instrument is replaced by a computer monitor. In addition, Virtual Instrumentation supports a variety of control systems: Plug-in Data Acquisition Board (DAQ), General Purpose Instrument Bus (GPIB), and VXI frames.

LabVIEW is a graphical programming language that allows building:

- block diagrams representing the code itself;
- a front panel for monitoring and controlling the system.

It enables the user to make modifications at any time to accommodate every changing application and unforeseen problem.

A virtual instrument (Appendix D) allowed control of the stepper motor. After that, a mechanical cross calibration provided a determination of the actual distance the stepper moved (Figure 2.13). Error bars represent the average percent difference between the actual distance the stepper moved and the theoretical distance requested by the VI. For the distance measured with dial indicator, the percentage difference is 0.66% whereas for the distance measured with the vernier caliper the percentage difference is 0.35%.

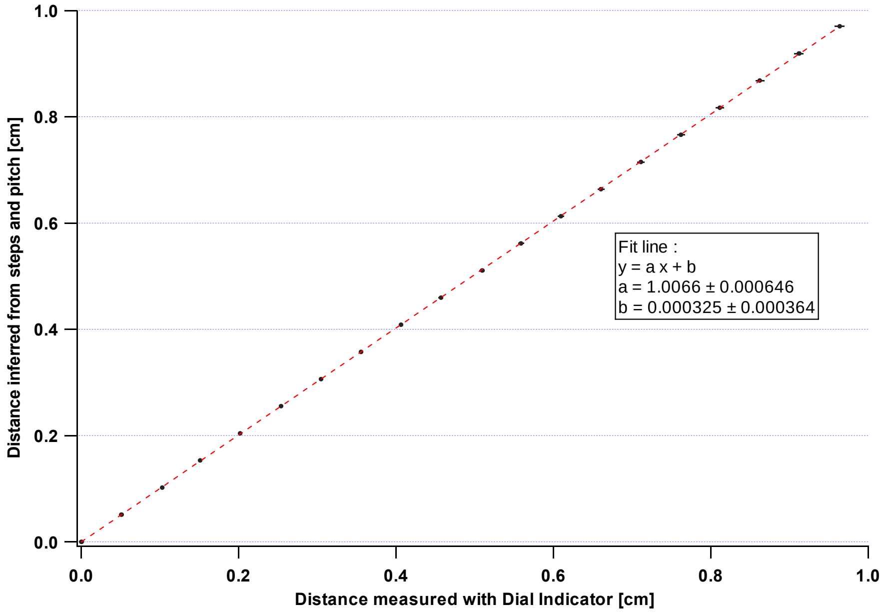

Figure 2.13 Cross Calibration of the linear mover

Knowing the correlation, 200 steps corresponding to one revolution, the Virtual Instrument was modified so that the motor is controlled by the distance and not by the number of pulses.

The acquisition of the signal of the various sensors is controlled by the HP34970A. The challenge with this system was to combine the motion control and the data acquisition. The Real-Time System Integration bus synchronizes them. RTSI, Real-Time System Integration bus, is a high-speed digital bus designed to facilitate system integration by high-speed real-time communication between National Instruments devices with no external cabling [14].

The VI works as follows:

- The program generates a “pulse train” of 100 Hz at the output of the SCB – 68 connector block, connected to the input of the stepper motor driver;
- The DAQ unit reads out the sensor response and the reference voltage through the analog board;
- The VI records these values with the distance moved in a text file;
- A main loop controlled by the start/stop button commands the number of readings or scans.

The sequence structure inside the main loop has two frames. The first frame (Appendix F), used for the control of the stepper motor, is described in the next sections. The second frame acquires the sensor response and the reference voltage by twice calling the same sub-VI, “HP34970A single pt.vi”. These sub-VIs are configured to read out simultaneously the Sensor Output (V) and the Reference Voltage (V) from the Agilent - HP 34970A (device 1). The diagram panel for this frame is shown in Figure 2.14.

The “HP34970A switch”.vi controls the HP3409A Matrix Switch and allows specifying which channel you wish to close or to open. This sub-vi also initialize the DAQ unit (HP 34970A).

Two modes of scanning are supported: continuous or step mode, selectable by indicating the total range and the scan interval. If the total range and the scan interval are the same, the motor will run continuously. Otherwise for every “x” inches, the stepper motor will stop and acquire data.

On the front panel (Appendix D), the type of sensor and the channel number can be selected by a Boolean control. An indicator called "Motor Scan" under the status section (Appendix E) shows the number of steps as the scan progresses to cover the desired limit. The VI stops when the scans are finished, then returns to its starting location by switching the direction of the stepper motor. Finally, the position and the data are appended to a data file in text format for later analysis.

The "While" loop repeats the sub diagram inside it until the conditional terminal receives a particular Boolean value. The Boolean value is set to "stop if TRUE". The While Loop executes only once. The iteration (**i**) terminal provides the current loop iteration count, which is zero for the first iteration. A section is used to check if the calibration scan has been performed entirely. In the "Status" sections on the front panel (Appendix E), the expected number of scans is calculated in the "total number of scans" terminal. On its left, a display of the scan's iteration allows to check if the calibrated distance has been fully completed.

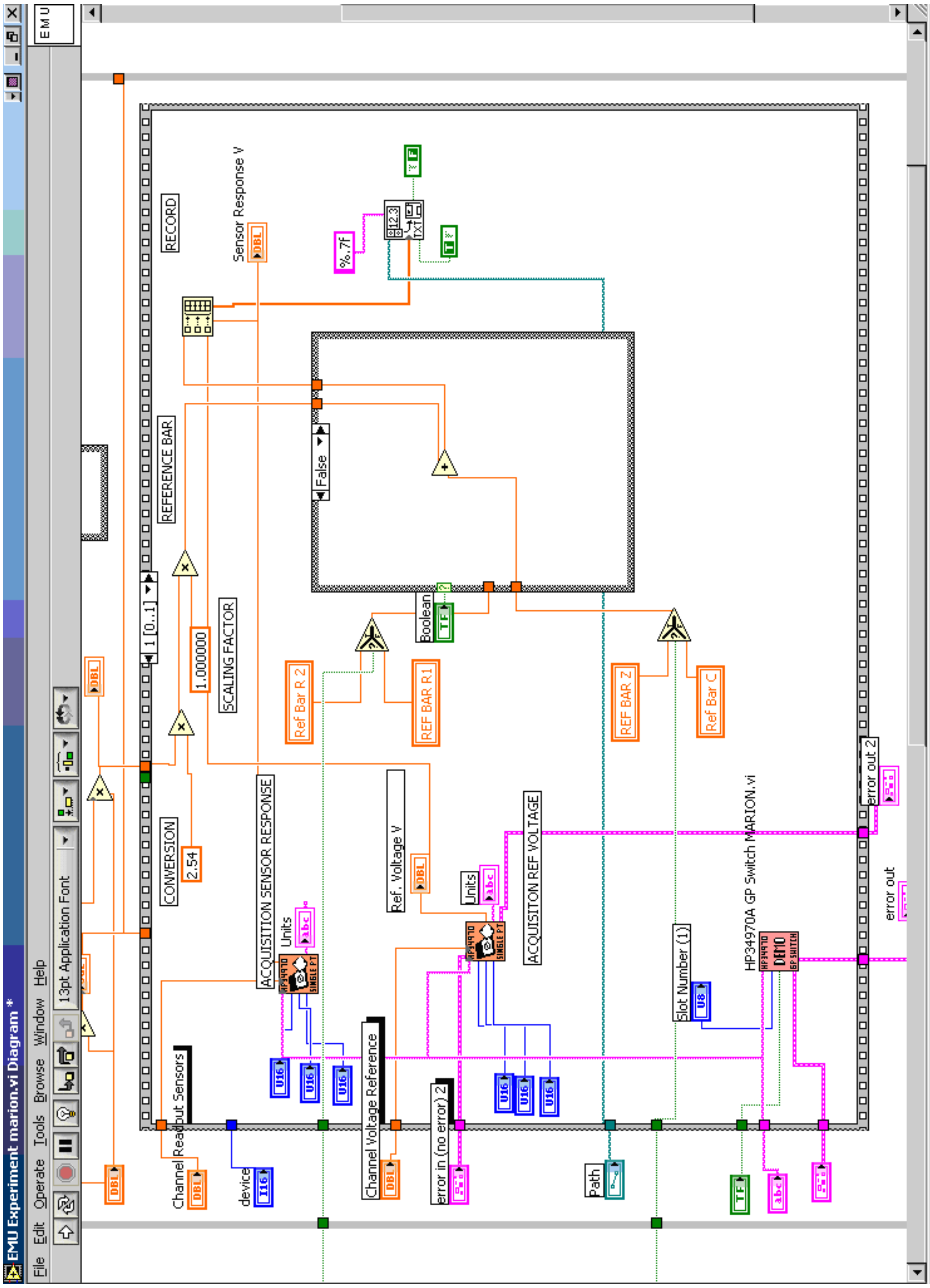

Figure 2.14 Diagram of the second frame

2.3.2 Motor Control with LabVIEW

A LabVIEW Virtual Instrument for generating digital TTL signals is used to provide the stepping sequence (f=100Hz) for a two-phase stepper motor.

The advantage of LabVIEW is that no hardware (except a computer and data acquisition card) is required to generate a signal. A stepper motor control system is developed using LabVIEW through a block connector SCB68 using Pulse Delay technique.

2.3.2.1 Characteristics of the CSK243 ATA stepper motor

The CSK 2 phase stepping motor series [15] includes high resolution types for which the full step mode is 1.8 º/step. The angular distance moved corresponds to the number of pulse input with a stopping accuracy of ±0.05º (with no load).

The driver requires a DC Supply Voltage of 24V and a current of 1.4A maximum with the motor rated current set to 0.95 A/phase. The standstill current reduction (current down) ratio is set to approximately 50 %. In order to prevent the motor and driver from becoming too hot and also to increase the motor's standstill holding torque, the motor's running current and standstill current have been lowered. However, reducing too much the current flow to the motor will smooth the rotation whereas increasing it will increase the stiffness and will also provide more torque (since the torque is almost proportional to current). The current down ratio percent, defined as the ratio of standstill current setting to running current setting, has been lowered to 44%.

The motor has a step angle of 1.8°, Resistance per phase of 4.2 Ω/phase, and maximum holding torque of 0.16 N.m. The direction signal is changed using the “pulse input mode switch”. Set to “1 pulse input mode”, the motor rotates clockwise; set to “2 pulse input mode”, counterclockwise.

2.3.2.2 Stepper Motor Configuration

The stepper motor configuration consists of three basic elements:

- The controller (PCI-6023-E via I/O connector SCB 68) capable of generating step pulses for the driver.
- The Driver converts the controller signals into the power necessary to energize the motor windings.

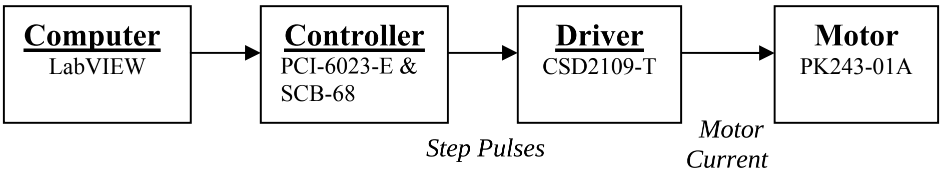

Figure 2.15 Stepper Motor Configuration System [15]

The stepper motor is a device for converting digital pulses into mechanical shaft rotation. The CSK-243ATA is a two-phase hybrid motor, combining a permanent magnet motor and the multi-toothed stator poles from a variable reluctance motor.

The principle of the permanent magnet motor consists in using the principle of a magnetic field on a weak magnet placed on the rotor (low number of steps/revolution). Applying a current to each phase will cause the rotor to rotate by adjusting the changing magnetic fields.

The variable reluctance motor does not use a permanent magnet, so that the rotor can move without constraint. However, a current applied to stator pole A through the motor windings will cause the rotor to align with the pole A (Figure 2.16). This process continues with the other poles.

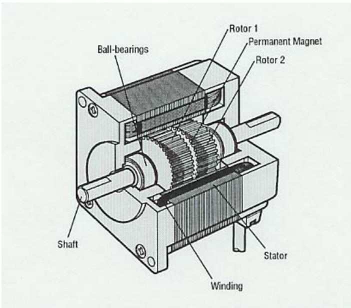

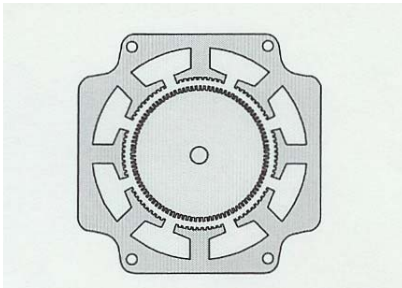

Figure 2.16 Structure of the 2-phaseStepping Motor (1.8 deg/step) and Cross section perpendicular to shaft [15]

In order to reach a sufficient resolution (number of steps per revolution), the magnet of the rotor is split into two rotors mechanically shifted. Between these two discs, a permanent magnet is inserted. The number of teeth on the rotor (50) is different from that of the stator. When the coil is excited, rotors place the North and South tooth in such a way that the flux crossing the rotor is maximal. It's possible to make each step-angle smaller by the driver (0.9 deg/step), but the step angle discrepancies increases.

In our project, the motor is coupled to a 20 cm threaded rod by a brass joint. The axis of the motor must be aligned with the threaded rod (Figure 2.17) to reduce the vibrations which would cause a reduction of the life of the ball bearing of the motor. The resolution of the entire driving system "stepper motor + threaded rod + movable table "is quantified by a cross calibration using a vernier caliper (resolution 0.001 ") and a dial indicator (resolution 0.001 ").

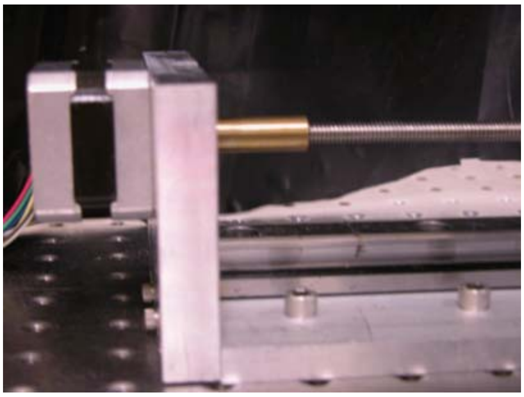

Figure 2.17 The driving system “stepper motor + threaded rod”

2.3.2.3 Stepper motor connections

Two counters (Figure 2.18) of the block connector SCB-68 are used to produce a finite pulse train of the input of the motor’s driver. All counters have a source input, a gate, and an output. Each pulse generated by a counter consists of a delay phase (phase 1) followed by a pulse phase (phase 2) of the desired polarity. Counter [0] is used to generate a continuous pulse train while counter [1] generates a minimum pulse delayed in order to control the stepper motor by our Virtual Instrument.

This “pulsewait”.vi shown in Figure 2.19 uses the “Generator Pulse Train.vi”, “Counter Stop.vi” and “Wait ms.vi” to produce a finite pulse train on the OUT pin#2 of the counter[0]].

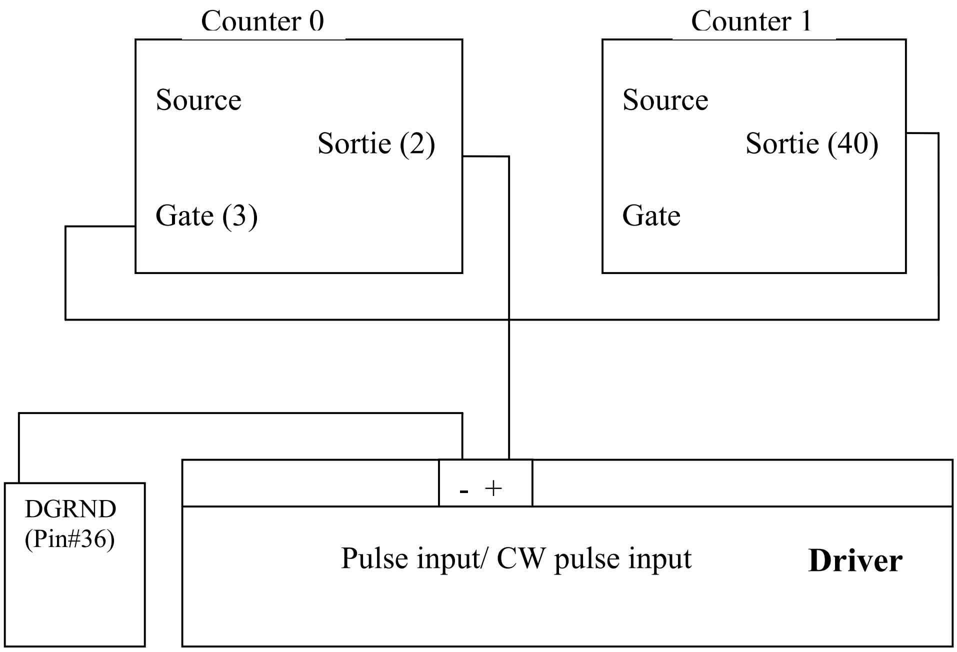

Figure 2.18 Connection between the counter 0 and 1 to generate a finite pulse train on the pulse/cw pulse input.

This VI uses the Generate Pulse Train.vi to produce a finite pulse train on the counter [0]. Counter [0] is set up to generate pulses while its gate input is high. This finite pulse train is created by gating a continuous counter (counter [0]) with a single minimum delayed pulse from counter [1]. The Wait (ms).vi is used as a delay before the counters are reset. The speed of the motor can be adjusted by this function. Finally, the "Counter Stop.vi" stops and resets the counters.

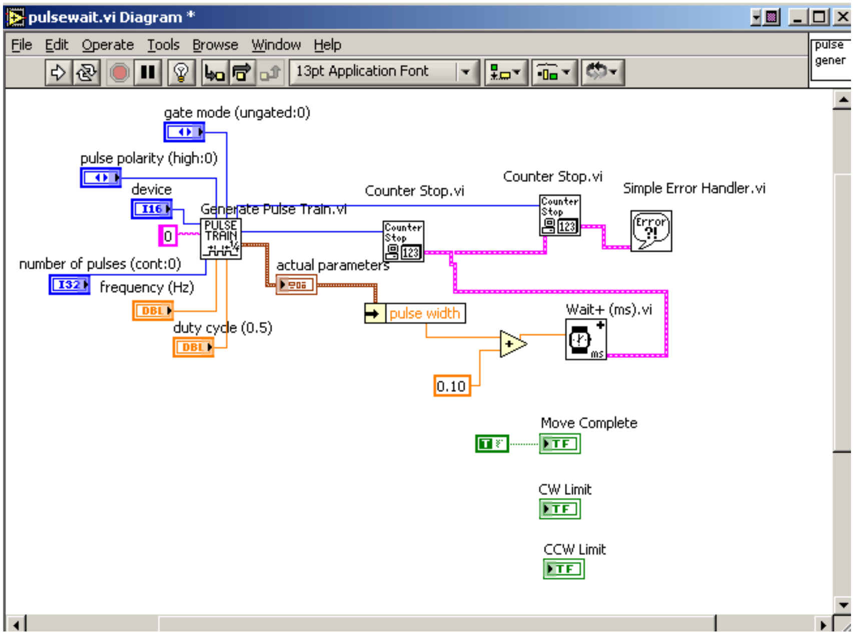

Figure 2.19 Diagram of the Pulse wait subvi

Parameters:

Gate mode: the ungated/software start ignores the gate source and starts when the VI is called.

Pulse polarity: high pulse means that phase1 of the pulse is a low TTL level and phase 2 is a high level.

Duty cycle: $\frac{phase\ 2}{period}$ where $period = phase1 + phase2$

A signal with a duty cycle of 0.5 is chosen since a high duty cycle will lead to a long pulse phase relative to the delay phase.

The width of the gating pulse is set to equal the actual period of the continuous pulse (T=1/100Hz) times the number of pulses (N). When using the calibration mode (step by step acquisition mode), each pulse is triggered at a fix delay of 1ms for any defined number of pulse as shown in Figure 2.19.

Number of Pulses: If number of pulses=0, the output is continuous.
If N>0, the output is N pulses.
If N=-1, a continuous pulse train is stopped.

As shown in the figure 2.18, the pulse signal is generated on the output pin#2 of counter [0] controlled by the "continuous pulse generator" Virtual Instrument. The OUT pin#2 is connected to the driver of the stepper motor.

The gate input (pin3) is used to activate counter [0] and to control a continuous pulse train. The OUT pin#40 of counter1 is connected to the GATE pin#3 of counter [0].

2.4 Cross Calibrations

A cross calibration of the calibration setup has been performed for each type of sensor. It is performed to verify the calibration consistency of the stepper motor to ensure that accurate steady distance measurement are provided by the control system managed by LabVIEW.

2.4.1 R and Z sensor

The curve (Figure 2.20) shows a systematic comparison of distance readings using a Mechanical Dial Indicator (Figure 2.21) to identify the deviation of the distance inferred from the VI from the mechanical measurement. Measured offsets from the Cross Calibrations have been inserted into the LabVIEW program for each type of sensors, summarized in the table 2.1 below.

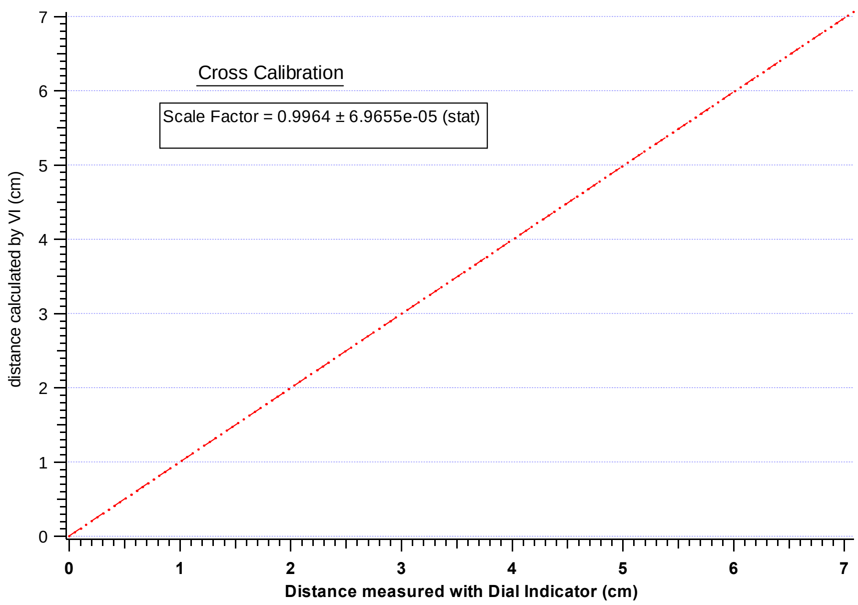

Figure 2.20 Cross Calibration for R1 sensor (ME+3/1-1TP4sens+31_04>OUT). Error bars cannot been seen due to small errors in the distance measured with dial indicator ±0.00025 cm

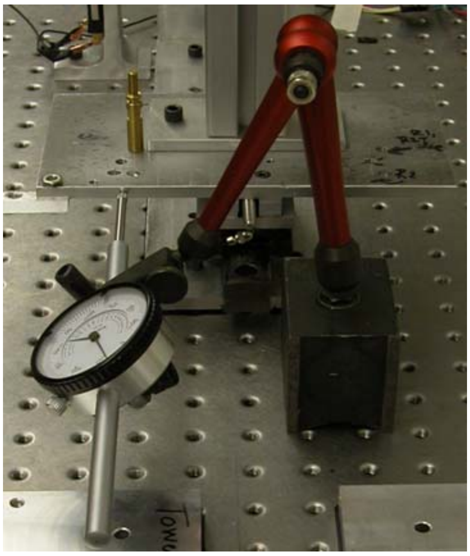

Figure 2.21 Mechanical Dial Indicator

A cross calibration was performed each time our mechanical bench was modified. Our last results are summarized in the table 2.1. The method of the cross calibration (Range, Channel readout) is the same as the procedure for the mass calibration of linear and angular sensors for which you can find technical details in Appendix G.

	R1	R2	R2-Tower	Z1 and Z2	INC + direction	INC - direction
Scale Factor	0.9964	1.0036	0.9986	0.99728	1.003121	1.0081362

Table 2.1 Offset or Scale Factor for different type of Analog Sensors

2.4.2 Clinometers

For the clinometers, the cross calibration method consists of a test to verify that accurate angles are measured using two different ways:

1. The distance moved by the stepper motor lead to an angle that can be calculated using this formula:

$$\theta_{geometry} = \arctan\left(\frac{\Delta x + x_0}{y}\right)$$

2. A rotary laser level reflects through a mirror attached to the clinometers adaptor (Figure 2.22). For each type of clinometers, a different adaptor has been built. The Inclinometer is screwed onto the adaptor. As the stepper motor turns, the table in contact with the clinometers by a blade is tilted. As in the cross calibration for R and Z sensor, the table is equipped with a high precision dial indicator (accuracy 0.0001").

The rotary laser level unit is located at 30 cm from the mirror. The reflection on the wall of the original beam allows us to calculate the angle moved using this equation:

$$\theta_{reflection} = \frac{1}{2}\arctan\left(\frac{h}{L}\right)$$

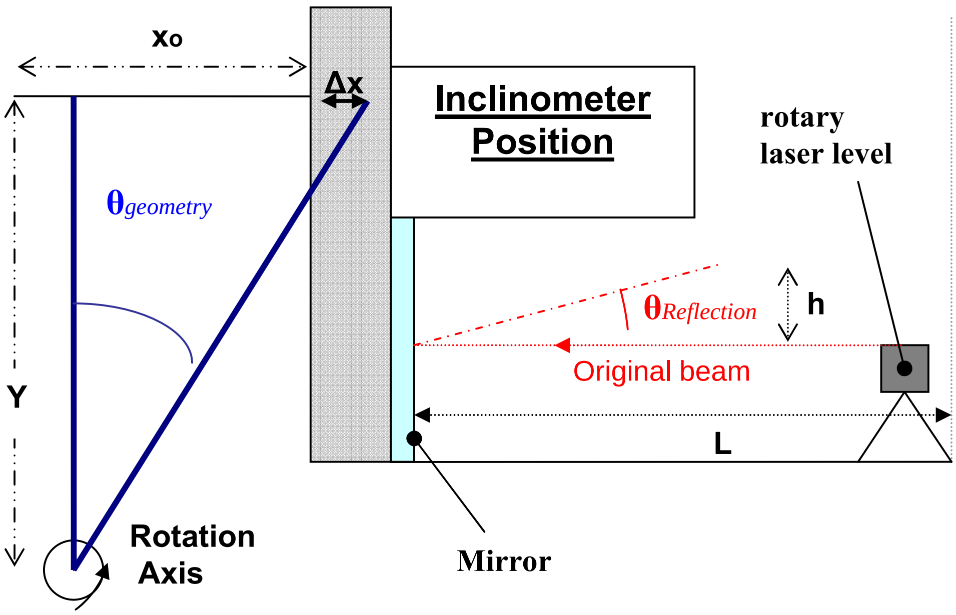

Figure 2.22 Sketch of the lateral view of the experimental set-up for clinometers

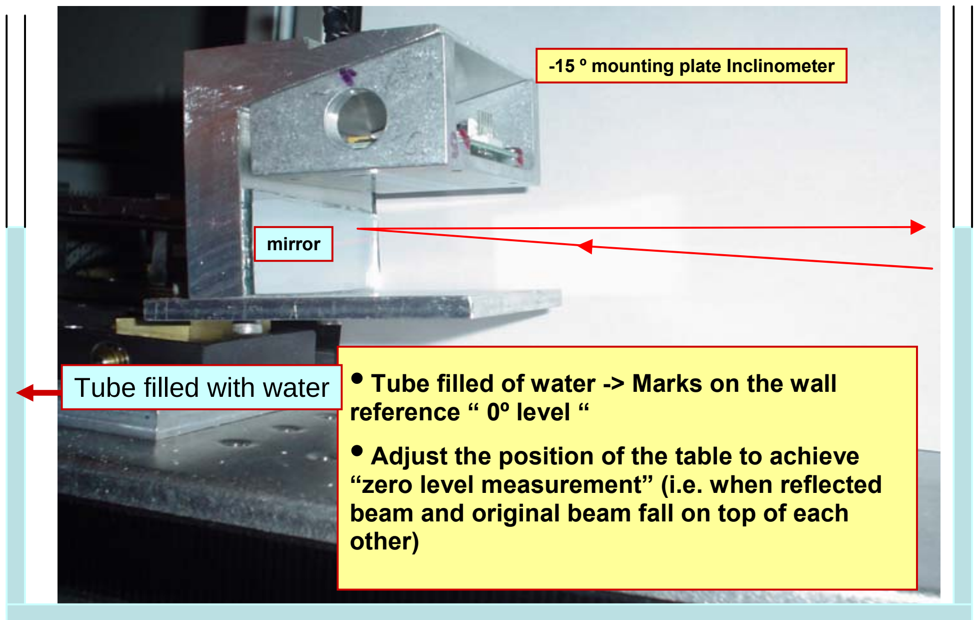

Figure 2.23 Photograph of the lateral view of the experimental set-up for clinometers

We find the zero level by using a 6 meter tube filled with water hanging along the lab (Figure 2.23). Two marks drawn on the walls with a pencil will be our level reference. We then fix the rotary laser level on these marks and take data. We moved the table in steps of "Δx" and take values of the tiltmeter voltage, of the "Δx" using the dial indicator and of the height of the reflected beam on the wall. This operation allows measuring simultaneously, with respect to the zero level reference, the voltage increment, and the value of the moved angle by two different ways. Figures 2.24 and 2.25 show the Cross Calibration curve in X and Y direction for -15 º Inclinometers.

2.5 Calibration Procedure

The calibration of R and Z sensors entails calibrating the absolute distance between a dowel pin or hole on the sensor mount to a post (R sensor) or surface (Z sensor).

2.5.1 R and Z sensors

The main sensor mount (Figure 2.26) with one sensor and two dowel pins, is positioned by means of the dowel pins on a stand, built and designed at Florida Institute of Technology. Our calibration bench was modified several times in order to satisfy the accuracy of the sensor output to be less than 150 micrometers.

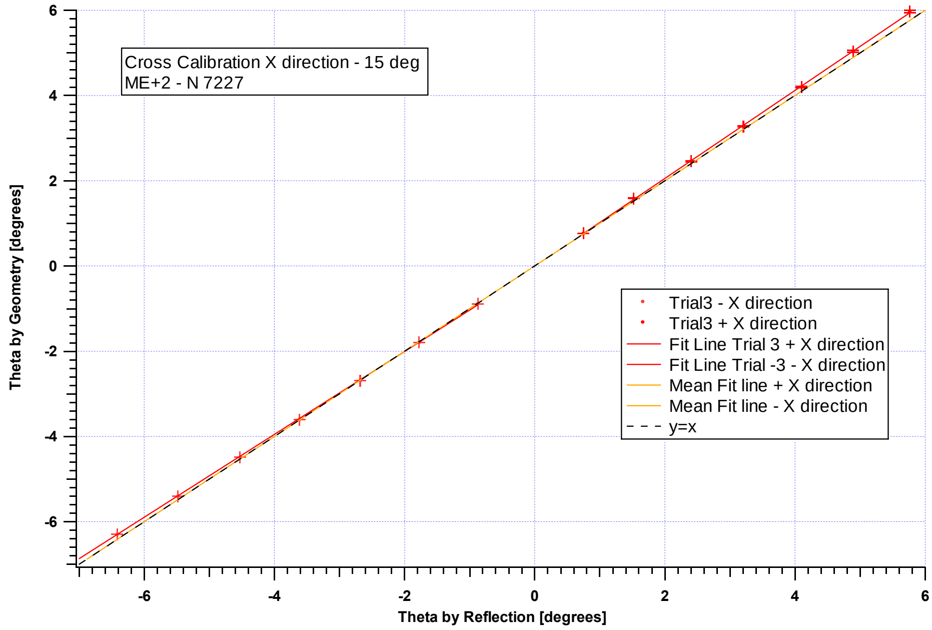

Figure 2.24 Cross Calibration X direction -15 deg

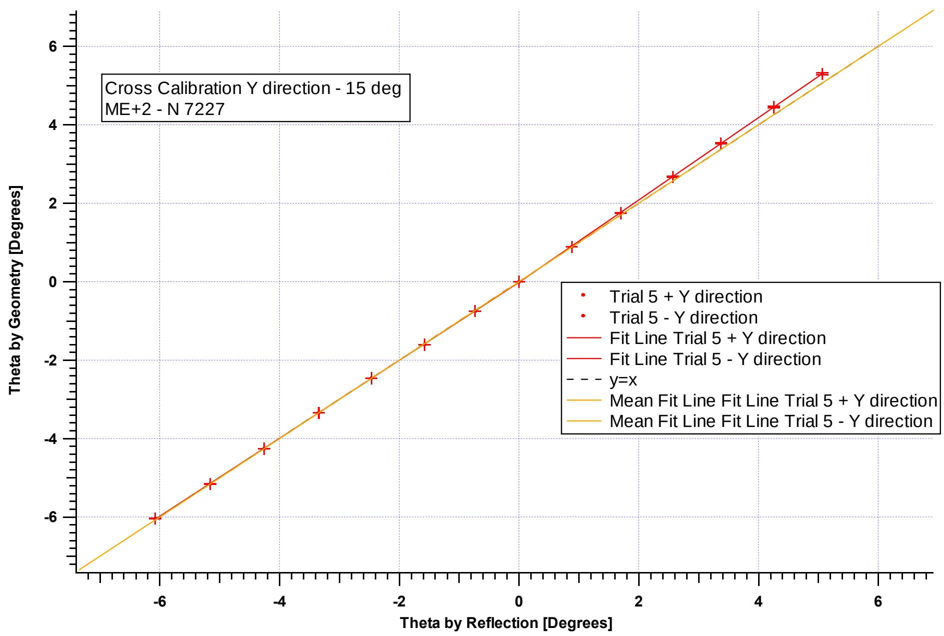

Figure 2.25 Cross Calibration Y direction -15 deg

The configuration of the calibration bench and the calibration procedure are such that:

1. The movable table and the mounts with sensors are parallel to each other with a precision of $\pm$ 0.001inch.

2. The line connecting the fixed “R –Post” to one of the dowel pins is orthogonal to the displacement. This absolute distance is measured each time a calibration for the R sensor output is done (Figure 2.28).

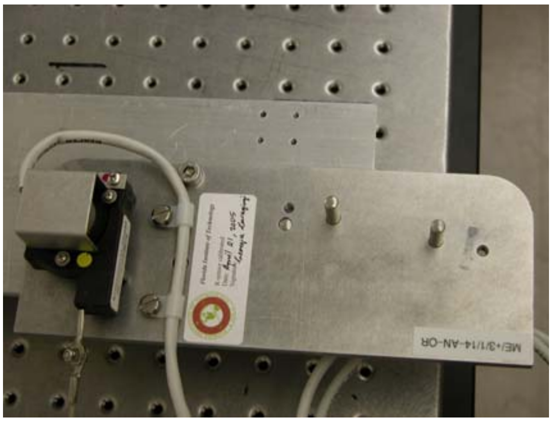

Figure 2.26 The main sensor mount with one R1 sensor on plate ME+3/1/14-AN-OR is positioned by means of two dowel pins and a spacer on a stand.

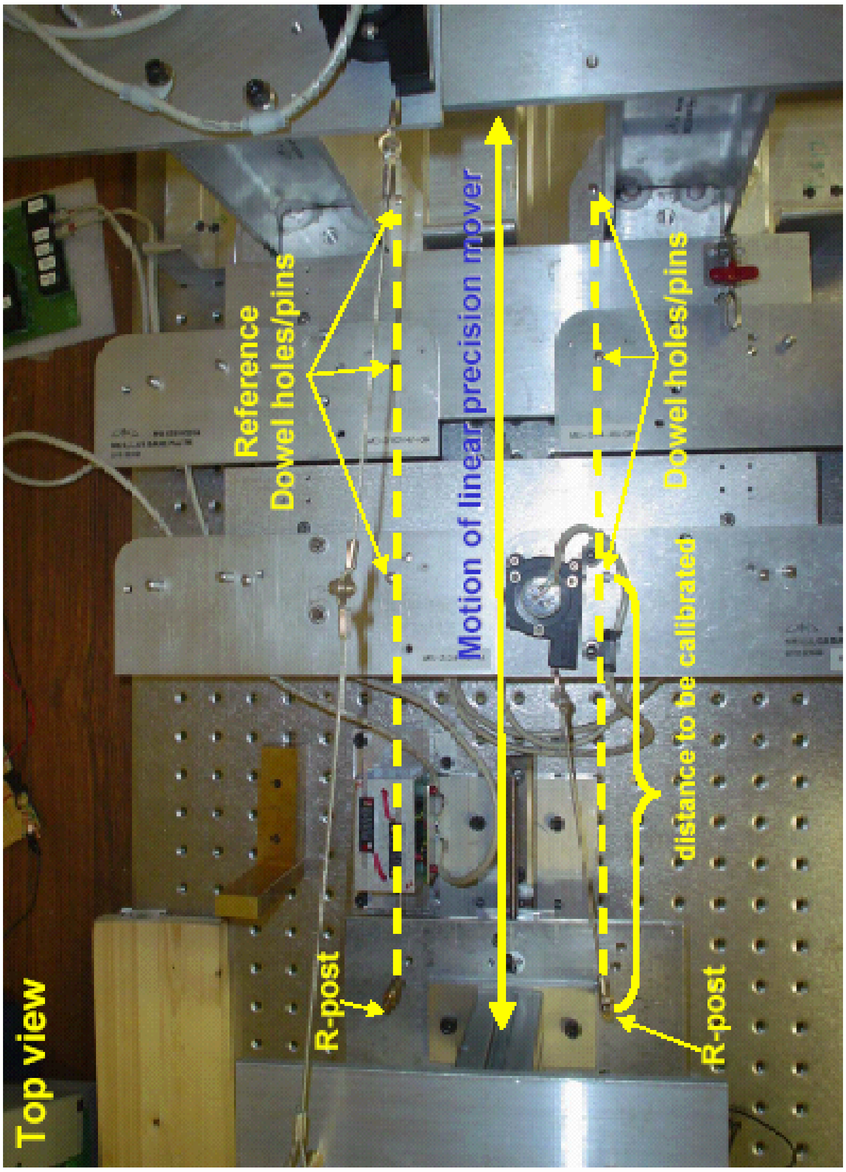

Figure 2.27 Calibration procedure for R sensors Line up reference points

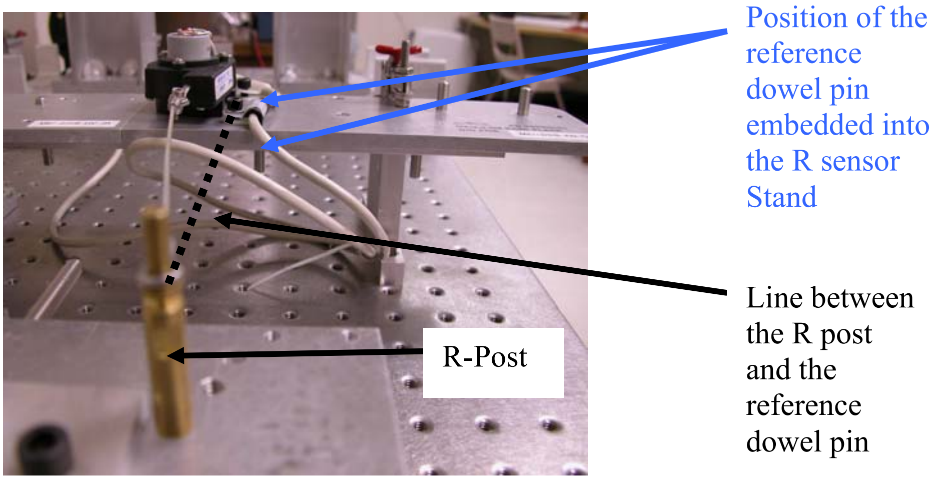

Figure 2.28 Calibration Alignment

3. A reference bar represents and quantifies with an uncertainty of ±1/1000 inches the absolute distance to calibrate. The reference bar is manually positioned between R post and R stand until 0% of the reference bar dowel pin stick out from the dowel hole (Figure 2.29).

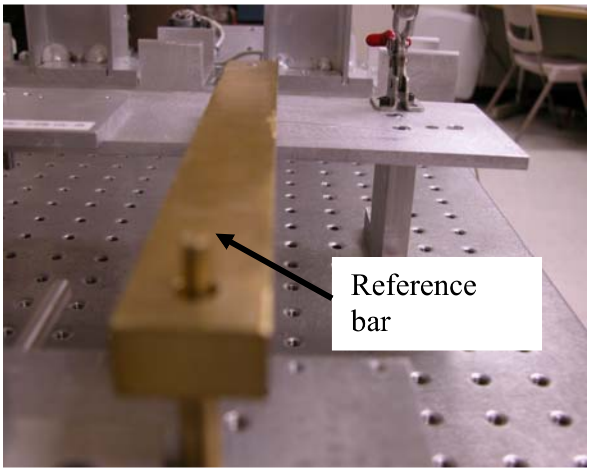

Figure 2.29 Reference bar representing an absolute initial distance

The following pictures (Figure 2.30-2.32) show the different reference bars used for the three types of R sensor: R1, R2 and R2 Tower.

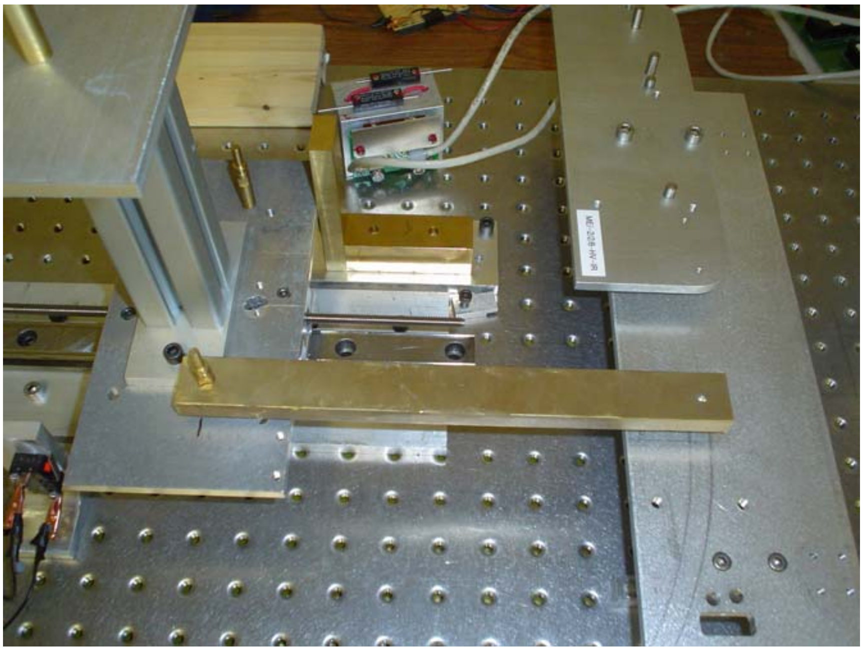

Figure 2.30 Position of R2 Reference Bar between R post and R2 stand

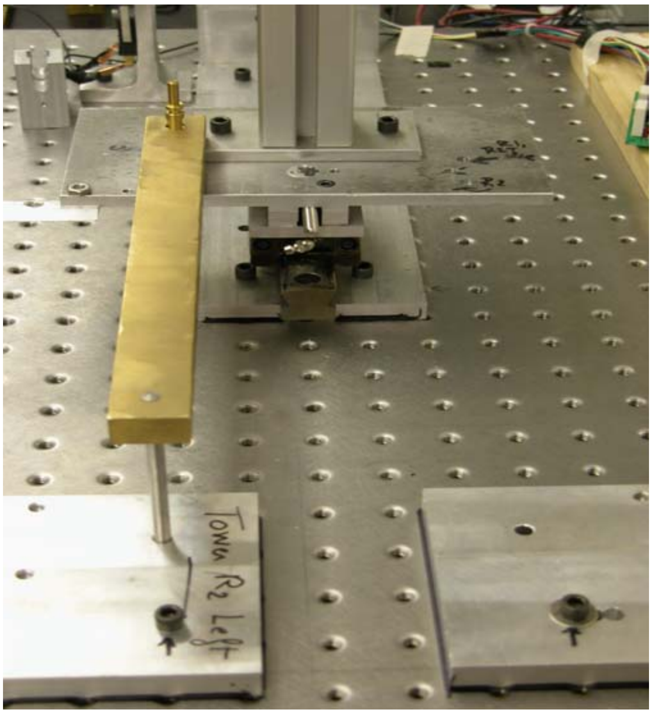

Figure 2.31 Position of R2 Tower Reference Bar

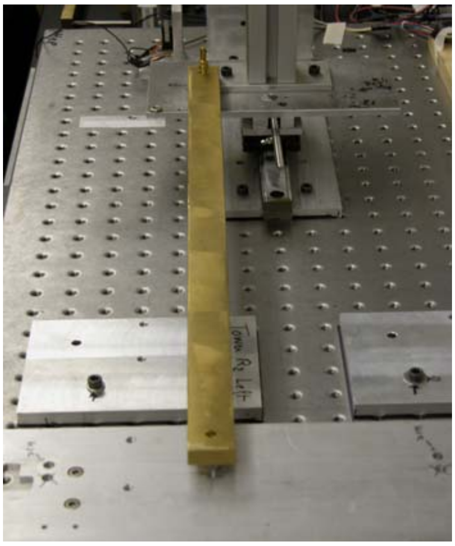

Figure 2.32 Position of R1 Reference Bar

4. The calibration procedure. The mount with the R sensor (Figure 2.33) is removed from the R–stand initial distance re-established with the reference bar, the mount remounted and a calibration performed. Five trials of the same sensors are taken in order to reduce the measurement uncertainties; this increases the precision of the calibration. Each time the absolute distance is checked using the reference bar (accuracy ~1/1000 inches). The average of the five trials will produce the calibration values for the sensor to be calibrated.

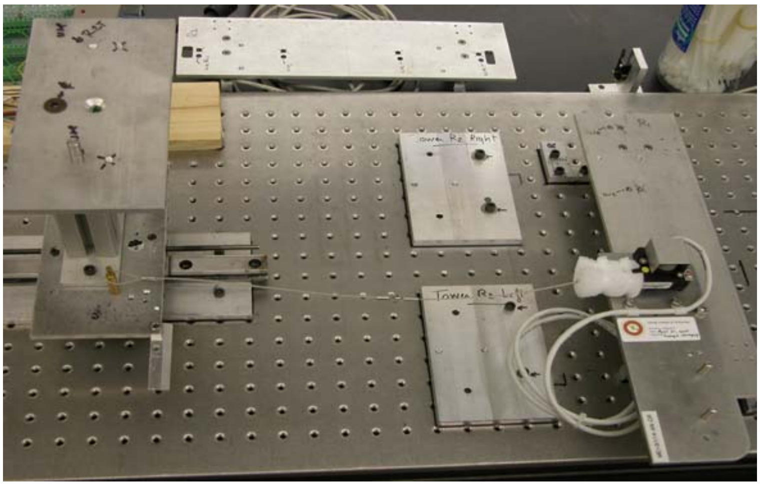

Figure 2.33 Position of R1 sensor on R1 stand after establishing initial absolute distance with reference bar

2.5.2 Z sensor

For the Z sensor, a reference bar (accuracy ~1/9000 inches) is also used to check the absolute distance before each calibration. Calibration procedure and detailed picture show the exact position of the reference bar (Figure 2.34).

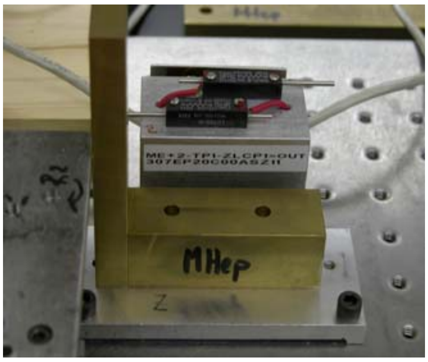

Figure 2.34 Position of Z reference bar

The analog interface board has a voltage regulator which is applied across the fixed terminals of the potentiometer. The voltage of the regulator can vary; in consequence for each calibration, the sensor output voltage and the reference voltage are recorded simultaneously.

2.5.3 Sensor Angles

When plotting the sensor output versus the total extension of the cable, three linear curves appear since the cable moves around the internal capstan of the sensor three times (Figure 2.35).

In comparison with simulations, the length of displacement of the Cathode Strip Chambers will be much smaller than the length of the cable. Taking this into account, the calibration of the response of the R sensors is carried out only about 5 cm on its first range whereas the Z sensors are calibrated over their full length (Appendix G).

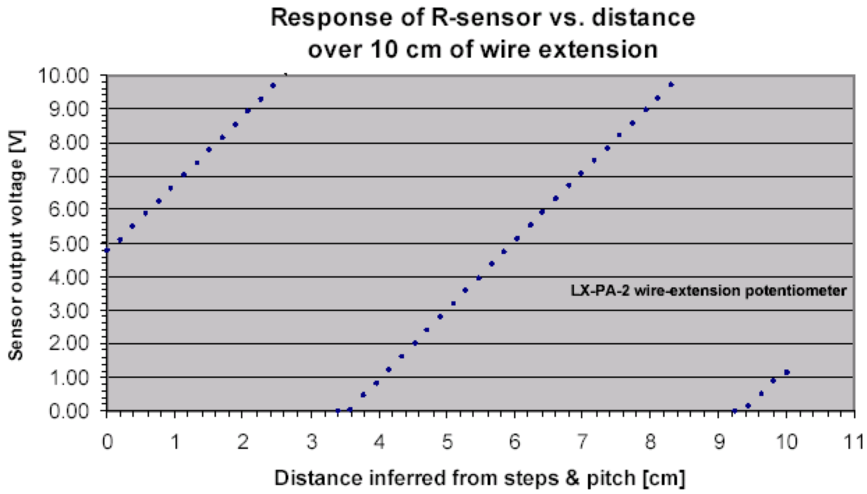

Figure 2.35 Typical R Sensor Response over its full range.

2.5.3 Inclinometers

The inclinometers are screwed on the inclinometers stand via adaptors. After adjusting the “zero level” with the rotary laser level and by matching on the wall the reflected beam with the original beam, the inclinometers are calibrated from -12º to 12º. As for previous sensors, for each trial (five in all), the “zero degree level” is rechecked between all measurements.

Chapter 3 Analysis and Results

In order to calibrate the analog sensors we checked the expected linear response of each sensor by taking five trials and calculated their average slope, y-intercept, and respective standard deviations and relative percent errors.

We are required to calibrate the different types of linear and angular sensors with a precision of 150 μm for R sensors, 1000 μm for Z sensors or better. The calibration accuracy of these sensors is determined by estimating the uncertainty in their absolute distance.

3.1 Sources of Error

Systematic errors [16] may results from:

- Unavoidable influences of the surroundings on the measurement (e.g. the temperature dependence of measuring instruments). During each calibration, the temperature is recorded.
- An unsuitable measurement method (e.g. calibration method). The initial calibration method turned out to be unsuitable; the next section will discuss it more in details and how we took care of it.
- Any operator mistakes during the performance of the measurement. An extensive list of possible errors such as the distance to be calibrated, the absolute position, or the channel configuration. This list has been regularly updated and as a consequence, a procedure manual was developed (Appendix G).

These systematic errors cannot be excluded entirely but we can keep this error as small as possible by carefully following the procedure measurement.

Random errors [16] also affect our results. Their causes can be:

- Due to vibration, the stepper motor coupling device might have some small random slippage,
- The value of the laser level on the wall is read too low or too high according to the position of the reader's head….

These random errors always deviate our measured results from the "true" value in one direction or the other. If the measurement is frequently repeated, deviations balance each other.

From these principles [16, 17], we conclude that for any measuring method, the result of a single measurement is not reliable since it can deviate more or less from the true value. Repetition of the measurement with the same measuring method we will give us a better estimate of the true value.

3.2 R sensors

R sensors are characterized by three types: R1 sensors, R2 sensors and R2 tower sensors. We are required to calibrate the three types of R sensors with a precision of 150 µm.

3.2.1 Uncertainty in the absolute R calibration

Many different checks were performed to ensure proper calibration of the R sensors. The tests consisted of quantifying uncertainties in the R sensors absolute calibration. Five different tests were conducted:

Tolerance in the dowel hole/pin for R1 and R2 sensors. To quantify this error, 30 trials of the reproducibility of the sensor response against distance were performed. The method reestablishes the initial absolute distance between each measurement. The detailed results of this test are described in section 3.2.3. Another test to estimate the tolerance in the dowel hole is to "wiggle" the plate in its stand to obtain the maximum deviation in the dowel hole. Our final precision in the dowel hole tolerance is $\delta x_{[TDOWEL]} = \pm 75$ µm. This uncertainty has been measured by plotting the Histogram of the Y-intercept for 30 measurements as shown in Figure 3.5.

Tolerance in the dowel hole/pin for R2 Tower sensors. The method is the same and all the statistical analysis is shown in Appendix H. Our precision in the dowel hole tolerance is $\delta x_{[TDOWEL]} = \pm 180$ µm.

<u>Initial absolute distance with reference bar</u> (Figure 3.1). The reference bar is manually positioned between R post and stand by slightly shifting the movable table until 0% of the reference bar dowel pin sticks out from the dowel hole. However, due to the intrinsic dowel hole tolerance, the deviation when 0% of the reference bar protrude is estimated to be $\delta x_{[REFBZERO]} = \pm 50$ µm. To measure this quantity, the stepper motor rotates (with the smallest step size of 0.00025'') until the percent of the reference bar protruded was around 90%. Thus, driving step by step the movable table until 0% of the reference bar protrude establishes the deviation of the dowel hole tolerance. Consequently, when establishing initial distance the operator has to be carefully support the reference bar until it reaches this position.

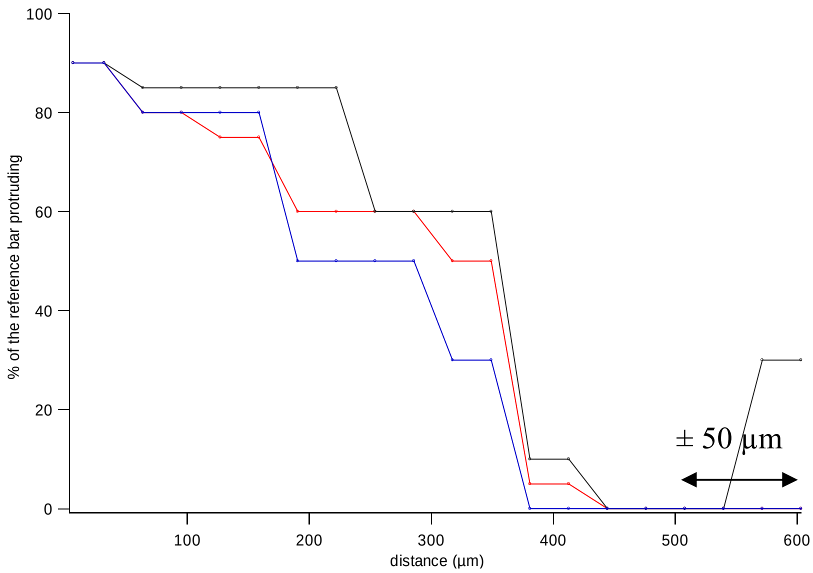

Figure 3.1 Uncertainty in initial absolute distance with R reference bar.

This quantity ($\delta x_{[REFBZERO]}$) is a measure of how well the dowel pin fits into the dowel hole. The uncertainty ($\delta x_{[REFBZERO]}$) in the absolute distance in the reference bar confirms our measurements of the uncertainty ($\delta x_{[TDOWEL]}$) of the tolerance in the dowel hole since $\delta x_{[REFBZERO]} < \delta x_{[TDOWEL]}$.

Calibration of stepper motor was already discussed in section 2.4. The stepper motor accuracy is estimated to be $\delta x_{[STEPMOTOR]} = \pm 5\ \mu m$.

Non-parallel mover axis and line connecting R post and dowel hole. By using a vernier caliper with resolution of 0.001' and a laser level, the small deviation was established by measuring the deviation shown by the laser level:

$\delta x_{[LPARALLEL]}$: ±2 μm.

3.2.2 Mechanical workpiece uncertainties

Dimensional accuracy. The workpiece (R stand, Z stand, clinometers adaptor) were designed to be square with a precision of ±0.001''. The accuracy of the two R reference bars were measured using a CNC precision tool by taking 15 measurements:

R2 reference bar: 8.99322 ±0.00012in = 228.427 ±0.003 mm (at 24ºC)

R1 reference bar: 18.00535 ±0.00017in = 457.336 ±0.004 mm (at 24ºC)

The uncertainty in the reference bars is estimated to be: δx = ± 4μm

The dynamic movement uncertainty. A PVC element initially coupled the threaded rod and the table. This piece contributed to vibration error and as a consequence to a large guidance uncertainty estimated to be around 120 μm over a 5 cm range. Delrin Acetal Polyoxymethylene (POM) resin was used to rebuild this element in order to prevent disturbance in the uncertainty in the guiding of the stepper motor. This material includes a high rigidity over temperature, resistance to repeated impact, mold low and screw deposit. The stepper motor accuracy with the Acetal element is now estimated to be ± 5µm.

Thermal deformation. Changes in temperature cause thermal effects on brass including thermal expansion. For the longest rod the main thermal deformation occurs along the length of the rod, and is given by:

$\delta_{brass} = \alpha_{brass}\left(\Delta T\right) L$ where

α_{brass} linear coefficient of expansion of brass $= 20 \times 10^{-6}\, l / °C$

ΔT temperature change the material experiences

L initial length of the rod

For a temperature increase of 3 ºC, the resulting change in length of the reference bar is about $\delta x_{[ThExp]} = 25$ µm.

The total uncertainty in R sensors was obtained from the four sensor tests and from the machining error. As the errors are independent [16], the total uncertainty in absolute R1 calibration for our system can be calculated using the equation:

$$\delta x_{total} = \sqrt{\delta x^2_{\text{REFBZERO}} + \delta x^2_{\text{TDOWEL}} + \delta x^2_{\text{STEPMOTOR}} + \delta x^2_{\text{LPARALLEL}} + \delta x^2_{\text{ThExp}} + \delta x^2_{\text{RefB}}}$$

$$\delta x_{total} = 100 \mu m$$

The uncertainty in the absolute distance at CMS is calculated using the same formula $\delta x_{total}^{CMS} = \sqrt{\left(\delta x_{total}^{calib}\right)^2 + \left(\delta x_{\mathrm{TDOWEL}}\right)^2} = 120\mu m$ with taking into consideration:

the total uncertainty in absolute R1 calibration for our system δx_{total} and,

the uncertainty in the dowel hole since the sensors will be mounted on the chambers and the uncertainty in the CMS dowel pin has to be added.

In order to ensure an equal treatment of all sensors, the calibrating method remained the same for all R sensors. A summary of the uncertainty in the absolute distance for all R sensors and a summary of the uncertainty in the absolute R distance at CMS are shown in Table 3.1, Table 3.2 and Table 3.3 respectively.

Random uncertainties:		
- Dowel hole/pin tolerances	**± 75**	**µm**
- Initial absolute distance with reference bars	**± 50**	**µm**
Systematic uncertainties:		
- Calibration of stepper motor (over 5 cm range)	**± 5**	**µm**
- Mechanical accuracy of reference bars	**± 4**	**µm**
- Thermal expansion of longest ref. bars (± 3ºC)	**± 25**	**µm**
- Non-parallel mover axis and line connecting R-post and dowel hole	**± 2**	**µm**
Total calibration Uncertainty	**± 100**	**µm**

Table 3.1 A summary of the uncertainty in the absolute R1 sensors calibration

<u>Random uncertainties:</u>	
- Dowel hole/pin tolerances	**± 75 µm**
<u>Systematic uncertainties:</u>	
- Total Calibration Uncertainty	**±100 µm**
Total:	**± 125 µm**
Required : ≤ ± 430 µm (from simulation)	

Table 3.2 A summary of the uncertainty in the absolute R1 distance at CMS

	R1 sensors	R2 sensor	R2 Tower sensor
Total Calibration Uncertainty	100 µm	189 µm	92 µm
Total Uncertainty at CMS	125 µm	200 µm	120 µm

Table 3.3 A summary of the Total calibration uncertainty δx_{total} and the total uncertainty at CMS δx_{total}^{CMS} for R1, R2 and R2 tower sensors.

3.2.3 Initial Results for R sensor:

Using the initial calibration stand, thirty measurements of the sensor response were taken and three out of thirty are plotted in the Figure 3.2. Between two measurements, the calibration procedure includes removing the plate from the stand, then reestablishing the initial absolute distance with the reference bar, remounting the plate and remeasuring. The average characteristic equation and the linear fit completed the final calibration for each sensor and and for each trial respectively.

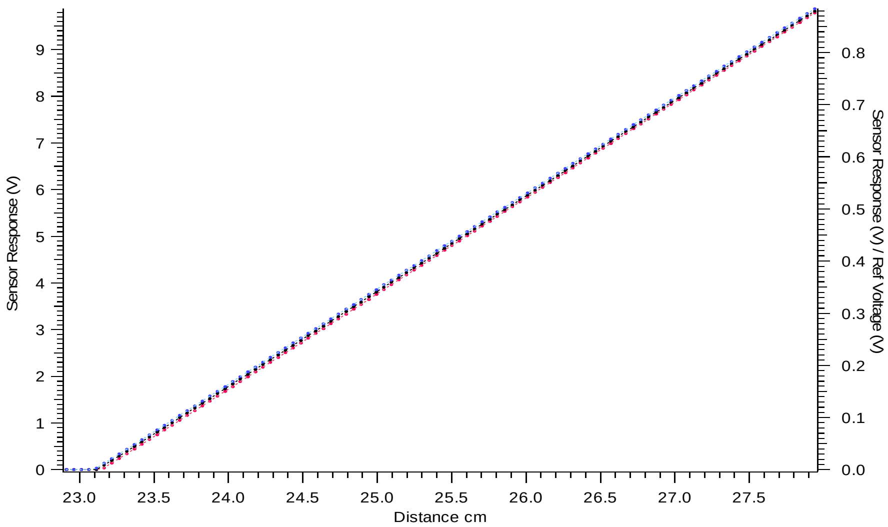

Figure 3.2 Sensor Response (V) vs. Distance (cm) from R post center to dowel hole center over a total length of 5 cm. 30 measurements of the extension of the R sensors LX-PA-2 S/N 3310410 on plate ME+2/2/8-AN-OR were taken. 3 measurements are shown.

The frequency distribution of the slope and of the y-intercept of each linear fit required at least 30 values to tell us about the variation of the values in the vicinity of the mean value. The mathematical measure of the variation is the root of the sum of the squares of the deviation of x from their average value, or the root mean square (rms) value.

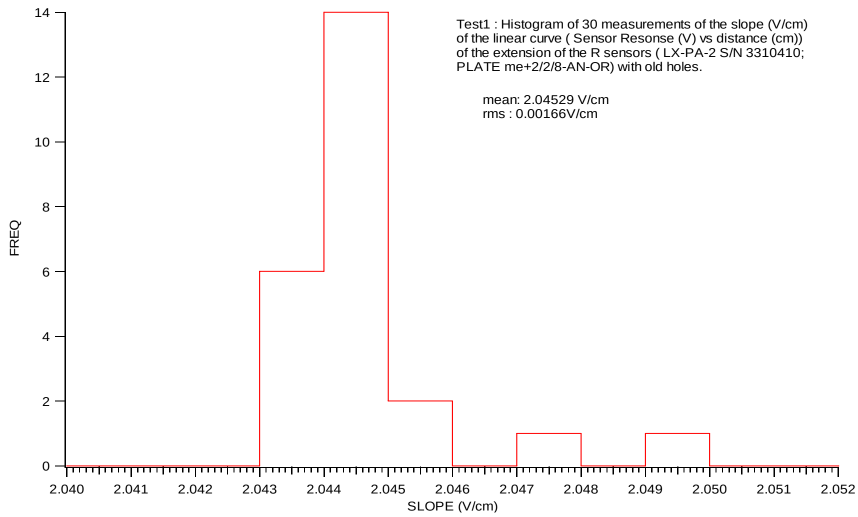

Figure 3.3 Histogram of 30 measurements of the slope (V/cm) of the linear curve (Sensor Response (V) vs. Distance (cm)) of the extension of the R sensors (LX-PA-2-S/N 3310+10 Plate ME+2/2/8 –A-N-OR) with original dowel holes.

3.2.4 R sensor before Mass Calibration.

The Histogram of the y-intercept (Figure 3.4) reveals a voltage rms of 0.609V. Knowing the mean of the histogram of the slope, the variation can be deducted:

$$\sigma(x) = \frac{0.0609V}{2.04529V/cm} 10^4 = 298\mu m$$

This large variation in the calibrated line quantifies a systematic error in measuring the absolute distance. A major part of my job was to understand and reduce sources of systematic errors.

In this experiment, the source of deviation was that the dowel holes had unacceptably large tolerances. We drilled some new tighter dowel holes; the correction did significantly improve the precision. Another set of data were taken with new holes giving us a ±75 μm variation in the y-intercept as shown on figure 3.5.

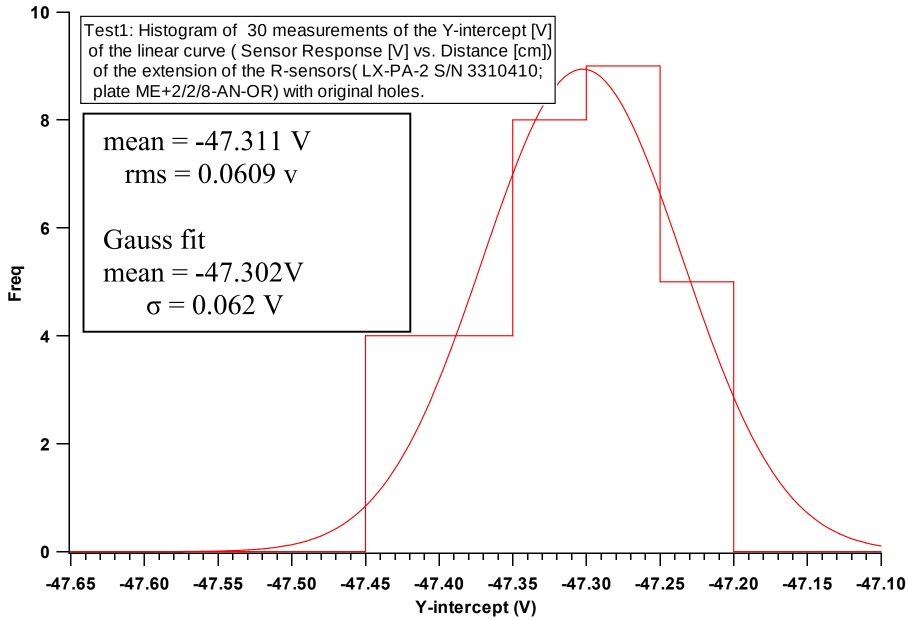

Figure 3.4 Histogram of 30 measurements of the Y-intercept (V) of the linear curve (Sensor Response (V) vs. Distance (cm)) of the extension of the R sensors (LX-PA-2-S/N 3310+10 Plate ME+2/2/8 –A-N-OR) with original dowel holes.

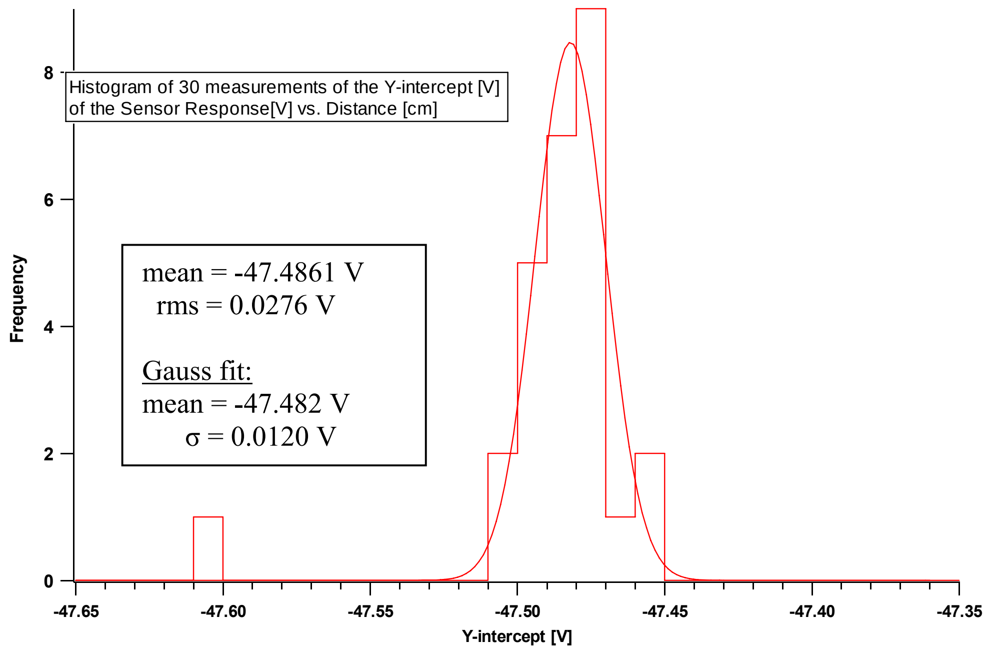

Figure 3.5 Histogram of 30 measurements of the Y-intercept (V) of the linear curve (Sensor Response (V) vs. Distance (cm)) of the extension of the R sensors (LX-PA-2-S/N 3310+10 Plate ME+2/2/8 –A-N-OR) with new dowel holes.

A sanity check taking 5 trials of the sensor response without dismounting and remounting the plate between measurements gives us an rms of 16 μm for the y-intercept, allowing us to conclude that the larger discrepancy is indeed due to the dismounting and remounting procedure and not an intrinsic problems of the linear mover. Knowing the mean of the histogram of the slope equal to 2.04709 V/cm and the voltage rms of the histogram of the Y-intercept (Figure 3.6), the variation in the calibration method is calculated using this equation:

$$\sigma(x) = \frac{0.0032V}{2.04709V/cm} 10^4 = 16\mu m$$

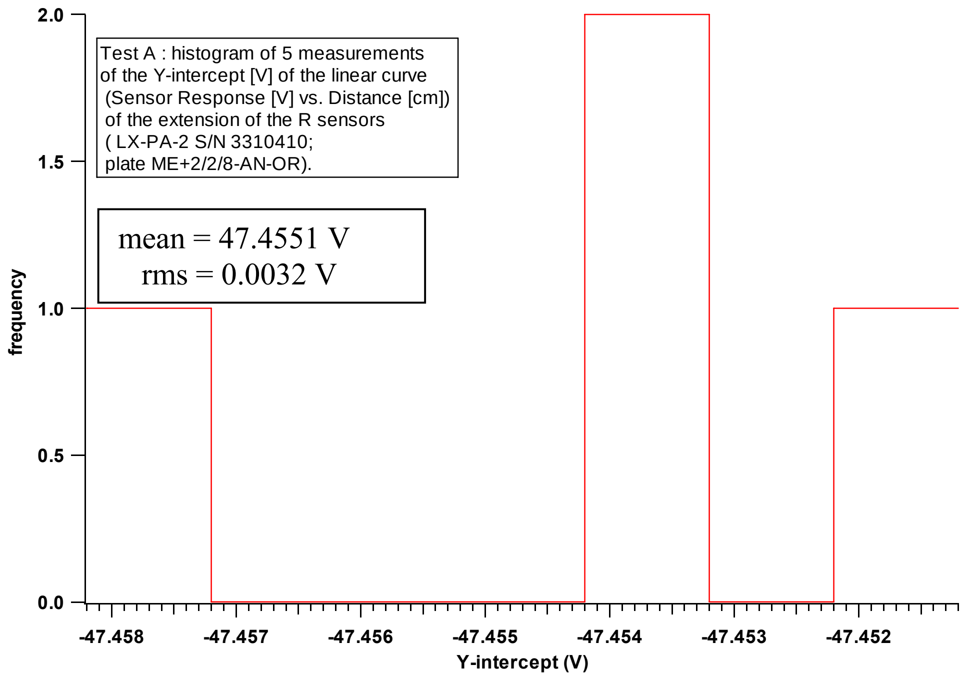

Figure 3.6 Sanity check: Histogram of 5 measurements of the Y-intercept (V) of the linear curve (Sensor Response (V) vs. Distance (cm)) of the extension of the R sensors (LX-PA-2-S/N 3310+10 Plate ME+2/2/8 –A-N-OR) with new dowel holes.

The tolerance of the dowel hole is double checked by a wiggling test: the plate is placed on the R sensor stand with dowel pin in dowel holes and is wiggled while we simultaneously record the sensor response (Figure 3.7).

The figure 3.8 shows two peaks representing the edge of the holes. The error in the dowel hole (100 µm) is consistent with the results from the histogram with the new dowel holes.

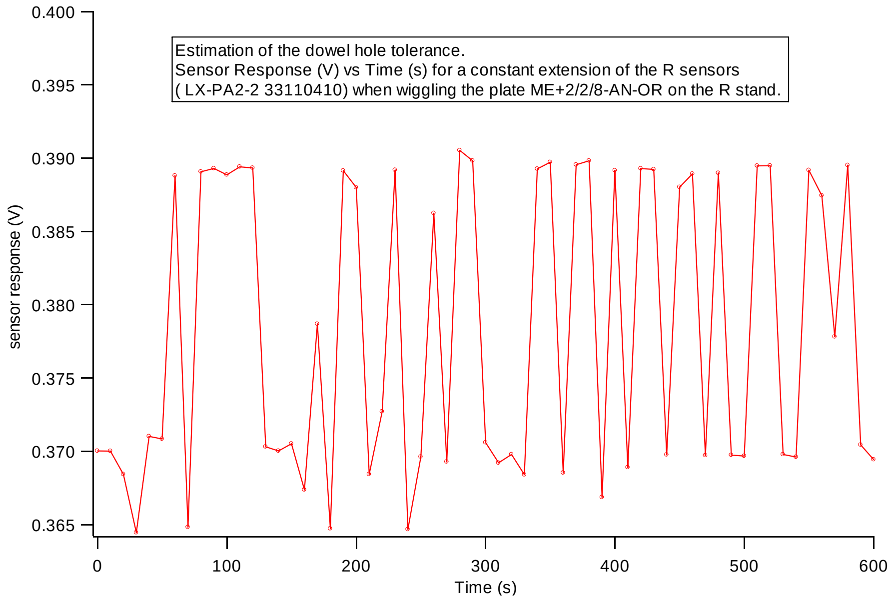

Figure 3.7 Sensor Response (V) vs. Time (s) for a constant extension of the R sensors (LX-PA-2-2-33110410) when wiggling the plate ME+2/2/8-AN-OR on the R stand.

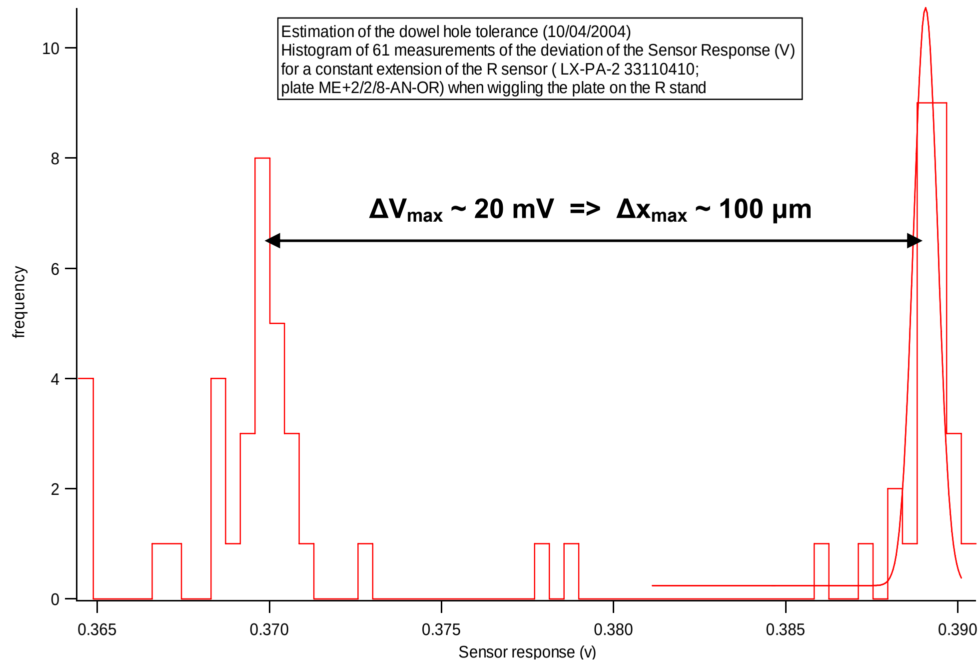

Figure 3.8 Histogram of 61 measurements of the Sensor Response (V) of the R sensors (LX-PA-2-S/N 3310+10 Plate ME+2/2/8 –A-N-OR) at rest when wiggling the plate on the R stand with new dowel holes without removing the plate between measurements.

3.2.6 Statistical analysis and results for the 12 R sensors of the ME+2 disk

The characteristic response curve is the measure of the output voltage against the distance moved. The result of the fit (continuous line) is shown on the same graph (Figure 3.9).

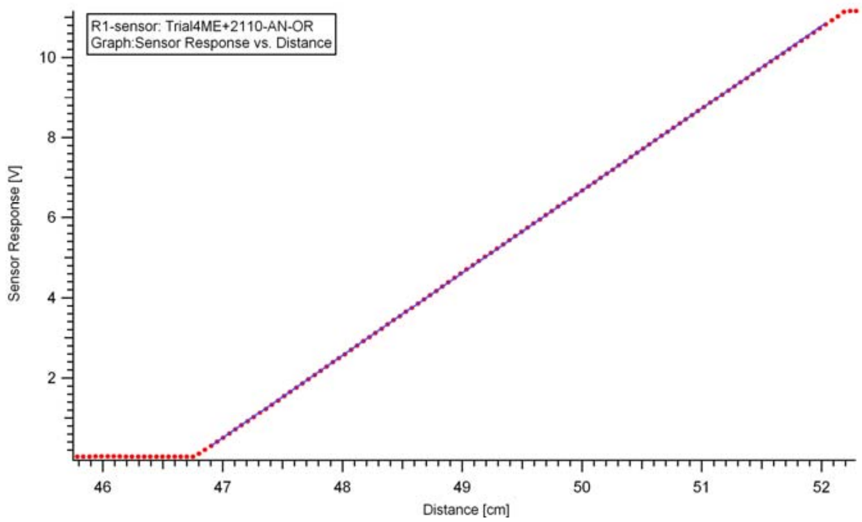

Figure 3.9 Calibration result: output response of one of the sensors as a function of distance. The average percent difference in the scale factor is used but error bars are too small to be distinguished.

The results of the Gaussian fit shown on the graph (Figure 3.10) lead to an overall sensor-to-sensor variation in the slope of 0.68 % for all R sensors.

A closer look, as shown in figure 3.11 and 3.12, reveals that each type of R sensors has different response values due to different angles formed by the cable and the virtual line joining the reference dowel pin and the R post for the three types of R sensors. In the side legend of figure 3.12, sensor response with different ranges for the R2 sensor (R2TP4 sens+22-20>OUT) was calibrated over two ranges due to a kink in the extension wire.

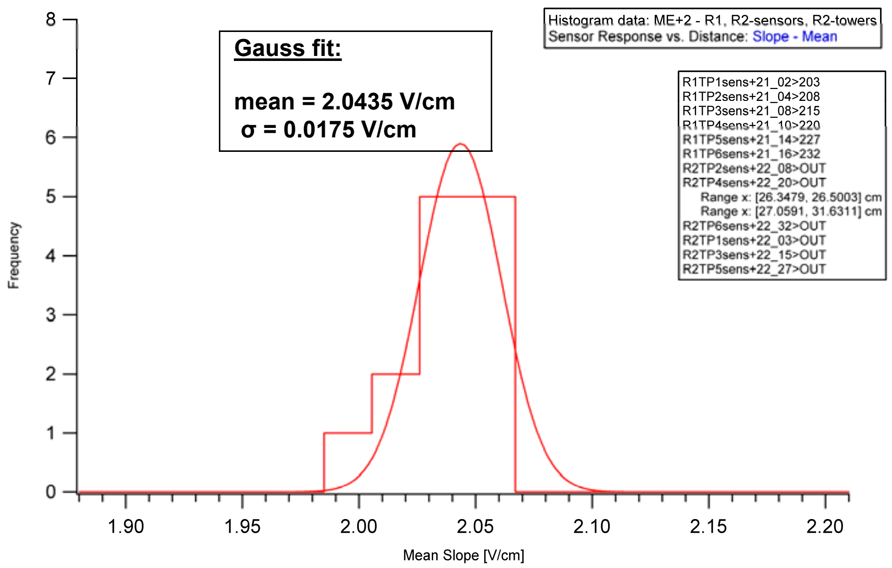

Figure 3.10 Histogram of the slope (V/cm) for all R sensors on ME+2 disk

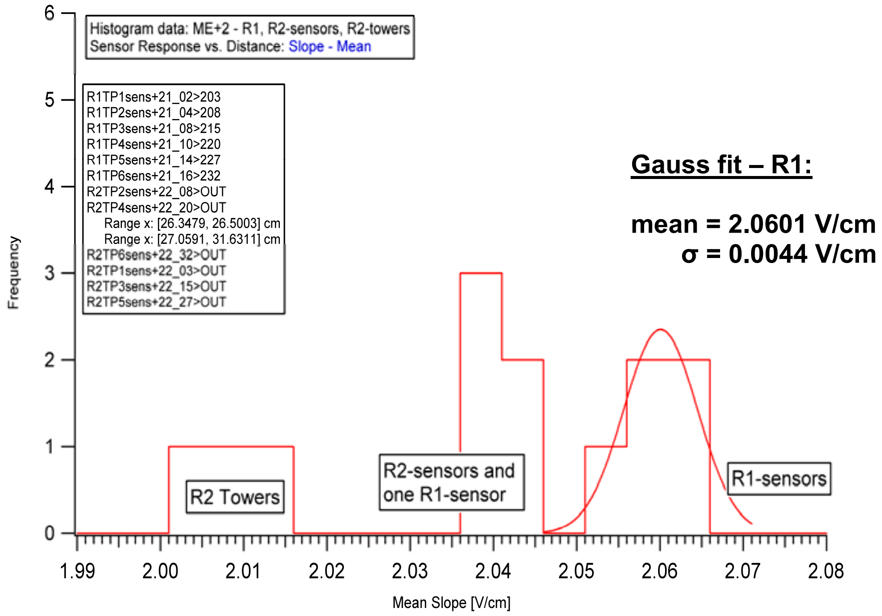

Figure 3.11 Zooms-in of the histogram of the slope (V/cm) for all R sensors on ME+2 disk reveal systematic differences between the three sensor types.

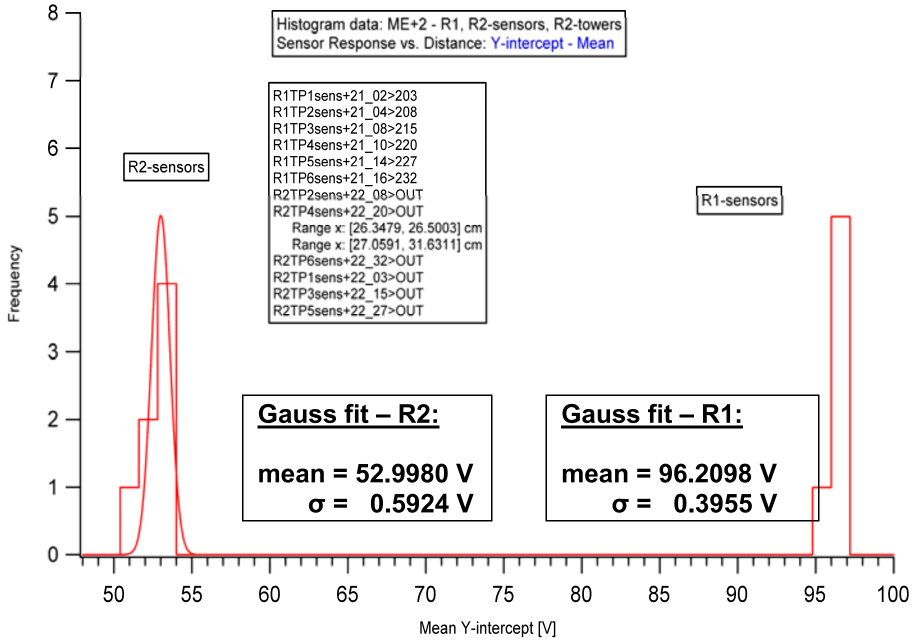

Figure 3.12 Histogram of the Y-intercept (V) for the 12 R sensors of the ME+2 disk

The approach to measure the deviation in the absolute distance is to make a histogram the frequency distribution of the Y-intercepts for the 12 R sensors. The sensor to sensor variation on the relative statistical error on the slope as derived from the linear fits (Figure 3.13) has a Gaussian profile at a relative percent error of 0.021% with a standard deviation equal to 0.015%. It proves that the deviation in the relative changes for the 12 R sensors is reasonably small (0.015%). For the sensor-to-sensor variation on the y-intercept (Figure 3.14), the typical Gaussian profile reveals a deviation in the relative statistical error in the absolute distance equal to 0.017%. Plotting the histogram of the mean reference voltage (Figure 3.15) for the 12 R sensors on ME+2 disk reveals a variation in the voltage regulator of .01%. An analysis of the ratio of the sensor response by the reference voltage consists of taking into consideration the variation in the reference voltage. The sensor-to-sensor variation in the slope (Figure 3.16) for R1 sensor for the Ratio (0.16%) is consistent with the results from the Histogram of the slope (Figure 3.10) of the Sensor Response versus Distance (0.22%).

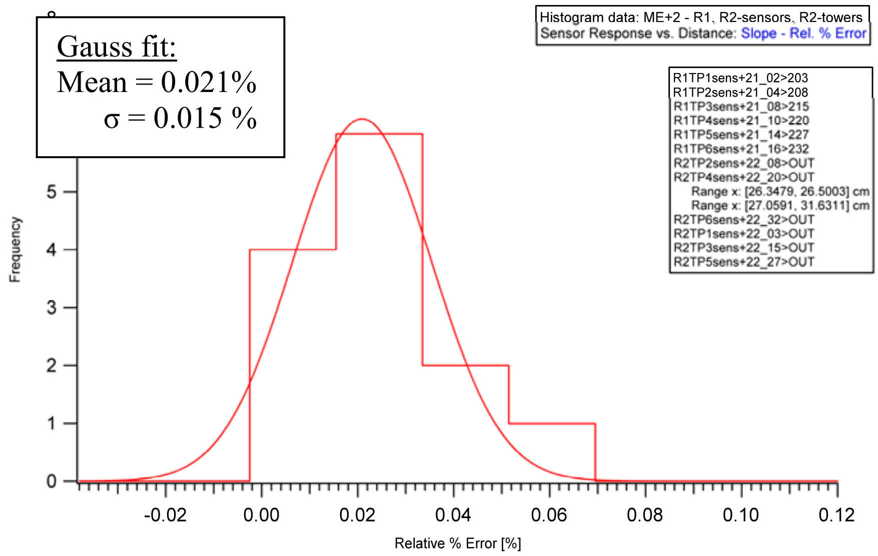

Figure 3.13 Histogram of relative statistical errors on the slope of ME+2 R sensors

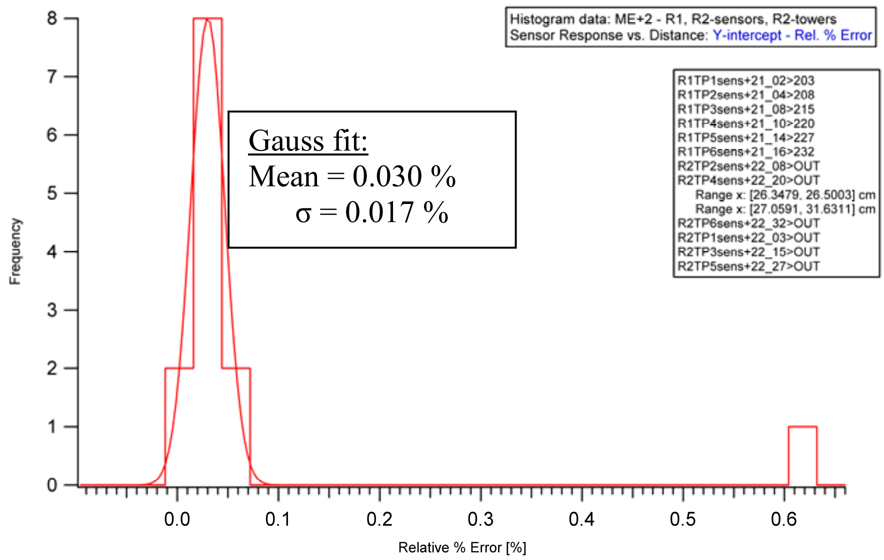

Figure 3.14 Histogram of relative statistical errors on the Y –intercept of ME+2 R sensors

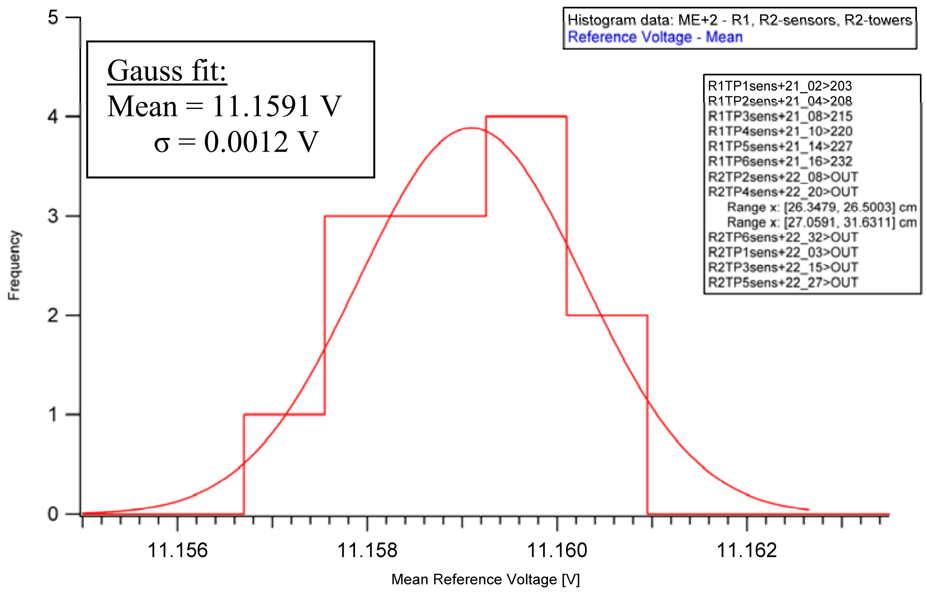

Figure 3.15 Histogram of the mean reference voltage of ME+2 R sensors

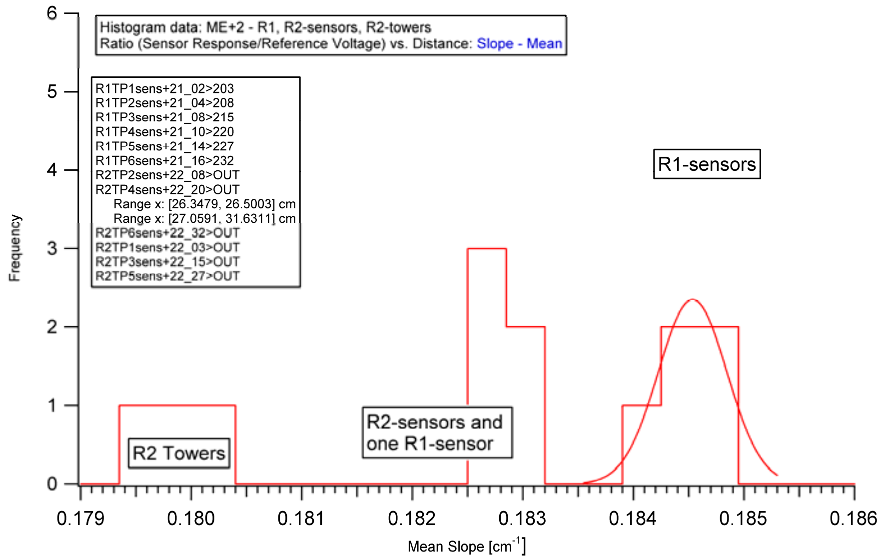

Figure 3.16 Histogram of the mean slope of the Ratio (Response Sensor / Reference Voltage) vs. Distance

3.3 Z sensors

We are required to calibrate the Z sensors with a precision to within 1000 µm. As for the R sensor, we checked the calibration accuracy by determining the possible systematic and random uncertainty in the absolute distance.

3.3.1 Uncertainty in the absolute Z calibration

The same assortment tests quantifying the absolute R calibration are performed for the absolute Z sensor calibration:

Tolerance in the dowel hole/pin. Our final precision in the dowel hole tolerance is $\delta x_{[TDOWEL]} = \pm 15$ µm. This uncertainty has been measured by plotting the Histogram of the Y-intercept for 5 measurements as shown in section 3.3.2 Figure 3.20).

Initial absolute distance with reference bar. (Figure 3.17) The reference bar is smoothly positioned by pushing it until full contact between linear mover and the reference bar is established. However, due to the ± 50 µm dowel hole tolerance, the deviation when no gap exists between the linear mover and the reference bar is estimated to be $\delta x_{[REFBZERO]} = \pm 50$ µm.

Calibration of stepper motor is the same for R and Z sensor. The stepper motor accuracy is estimated to be $\delta x_{[STEPMOTOR]} \pm 5$µm.

The dimensional accuracy. The accuracy of the Z reference bar was measured using a CNC precision tool by taking 15 measurements:

Z reference bar: 1.15325 ± 0.0009 in = 29.293 ±0.002mm (at 24ºC), so the uncertainty in the reference bars is estimated to be δx= ± 2μm.

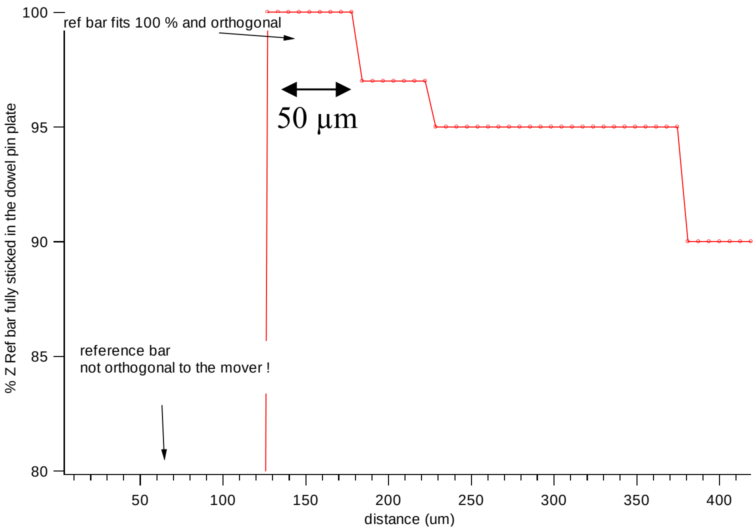

Figure 3.17 Uncertainty in initial absolute distance with Z reference bar

The thermal deformation. Changes in temperature cause thermal effects on brass including thermal deformation. For a temperature increase of 3 ºC, the change in length of the reference bar is about $\delta x_{\text{ThExp}} = 2$ μm.

The total uncertainty for our system in absolute Z calibration can be calculated using the equation [16]:

$$\delta x_{total}^{calib} = \sqrt{\delta x^2_{\text{REFBZERO}} + \delta x^2_{\text{TDOWEL}} + \delta x^2_{\text{STEPMOTOR}} + \delta x^2_{\text{ThExp}} + \delta x^2_{\text{RefB}}} \sim 53 \text{ μm}.$$

The uncertainty in the absolute distance at CMS will be equal to $\delta x_{CMS}^{total} = \sqrt{\left(\delta x_{total}^{calib}\right)^2 + \delta x^2{}_{\mathrm{TDOWEL}}} = 55\mu m$.

A summary of the uncertainty in absolute Z sensors calibration is shown in Table 3.4 and 3.5

Random uncertainties:	
- Dowel hole/pin tolerances	**± 15 µm**
- Initial absolute distance with reference bars	**± 50 µm**
Systematic uncertainties:	
- Calibration of stepper motor (over 1 cm range)	**± 5 µm**
- Mechanical accuracy of reference bar	**± 2 µm**
- Thermal expansion of ref. bar (± 3ºC)	**± 2 µm**
Total Calibration Uncertainty	**± 53 µm**

Table 3.4 A summary of the uncertainty in the absolute Z sensors calibration

Random uncertainties:	
- Dowel hole/pin tolerances	**± 15 µm**
Systematic uncertainties:	
- Total Calibration Uncertainty	**± 53 µm**
Total:	**≤ ± 55 µm**
Required : ≤ ± 1000 µm (from simulation)	

Table 3.5 A summary of the uncertainty in absolute Z distance at CMS

3.3.2 Initial Results for Z sensor:

5 measurements of the sensor response were taken and are plotted on figure 3.18. Between two measurements, the calibration method is always to remove the plate from the stand, then reestablish the initial absolute distance with the reference bar, remount the plate, and remeasure.

A Z sensor non-linearity is observed in figure 3.18. This maximum non-linearity corresponds to Δx =125μm. The maximum non-linearity The Histogram of the slopes (Figure 3.19) reveals a variation of 4.7 μm over a full range of 10 mm, this dispersion in our calibrated line quantify a systematic small error in the measuring relative changes in distances. The variation in the relative changes in distances is calculated using this formula:

$$\sigma_{\Delta x} = \left(\frac{\sigma(<slope>)}{<slope>} \right) (Range)$$

$$\sigma_{\Delta x} = \left(\frac{0.047}{100} \right) * 1.05 * 10^4 = 4.7 \mu m$$

$$5 \text{ calibrations measurements per sensor},$$

$$\sigma_{\Delta x} = \left(\frac{0.047}{100} \right) * 1.05 * 10^4 = 4.7 \mu m$$

The systematic uncertainty due to dowel hole tolerance is determined by plotting the frequency distribution of the y-intercept (V) revealing a systematic uncertainty of 15 μm (Figure 3.20):

$$\sigma_x = \frac{0.0158\,V}{10.3798\,V/cm} 10^4 = 15 \mu m$$

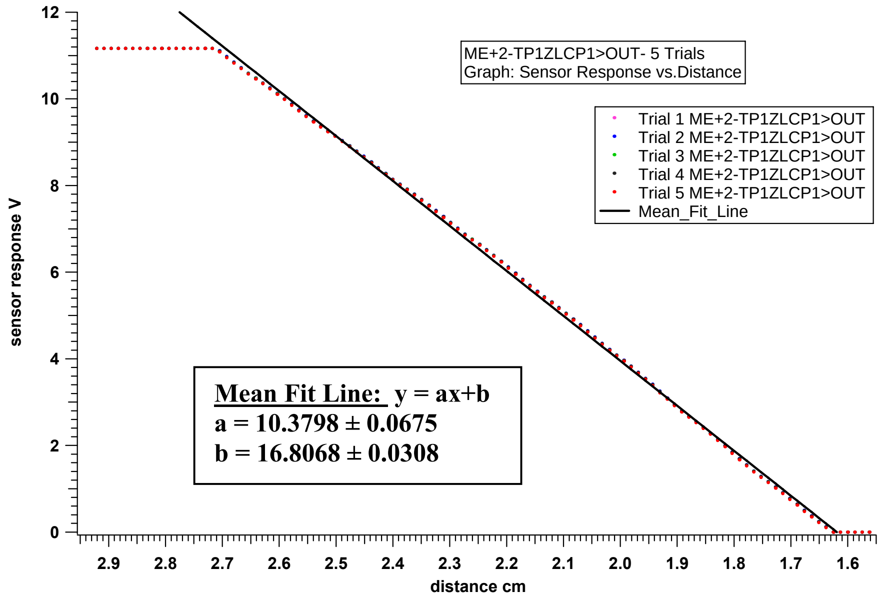

Figure 3.18 ZLCP1 Sensor Response (V) vs Distance (cm) - 5 measurements of Z-LCP1 were taken. Each measurement contains 108 points.

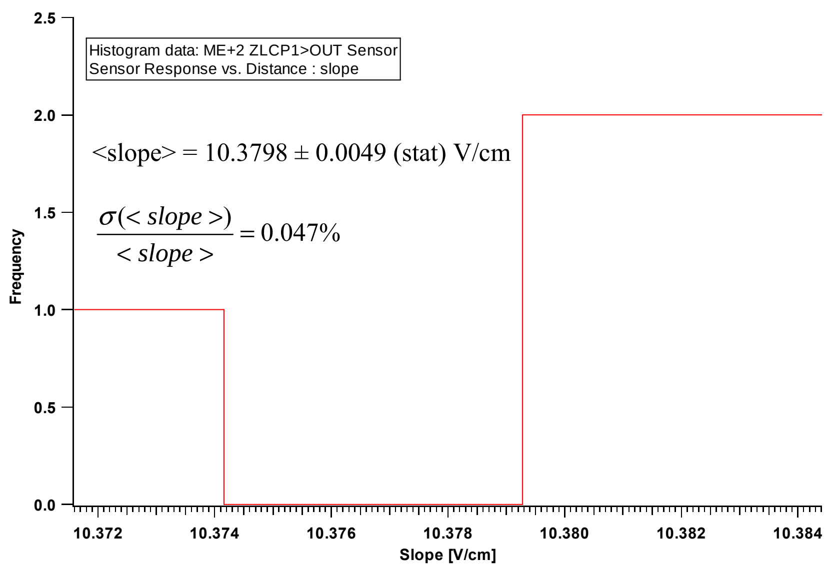

Figure 3.19 Histogram of 5 measurements of the slope [V/cm] of the Sensor (ME+2 TP1-ZLCP1) Response vs. Distance.

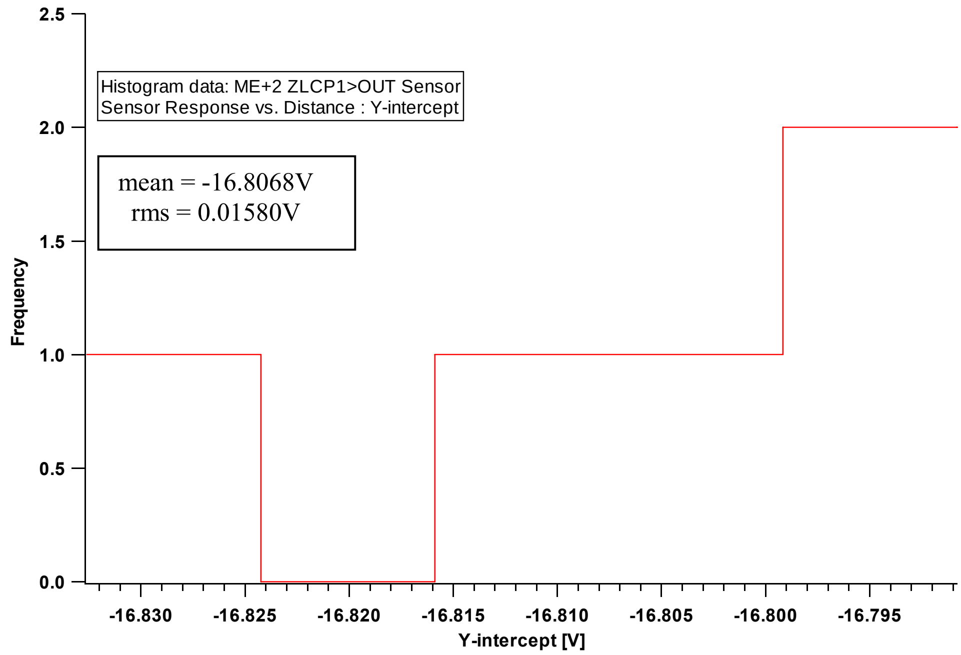

Figure 3.20 Histogram of 5 measurements of the Y-intercept [V] of the sensor (ME+2 TP1-ZLCP1) Response vs. Distance.

This tolerance of the dowel hole is double checked. The method is to wiggle the plate placed on the Z stand and simultaneously to record the sensor response (Figure 3.21). The frequency distribution of the Sensor Response (Figure 3.22) shows only one peak perhaps due to the fact that one of the dowel holes is a slot. With an rms of the histogram of 0.003V, the uncertainty in the dowel hole is estimated to be within 2.89 µm using the following formula:

$$\sigma_x = \frac{0.003V}{10.3798V/cm} 10^4 = 2.89 \mu m$$

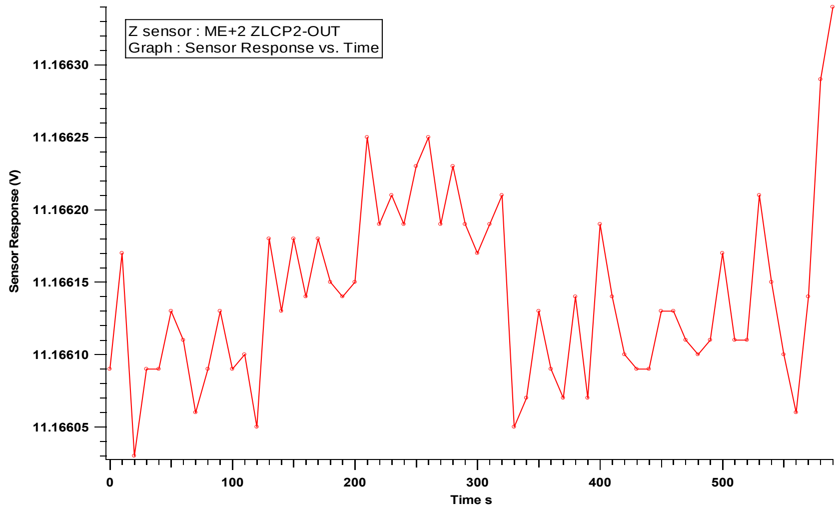

Figure 3.21 Sensor Response (V) vs. Time (s) for a constant extension of the Z sensor (ME+2-ZLCP2-OUT) when wiggling the plate on the Z stand.

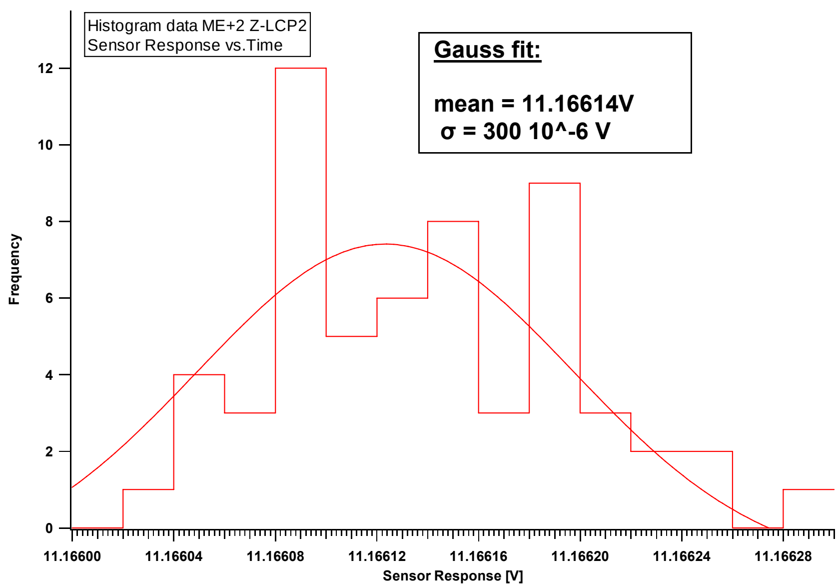

Figure 3.22 Histogram of 60 measurements of the Sensor Response (V) of the Z sensors (ME+2 ZLCP2 -OUT) at rest when wiggling the plate on the Z stand

3.3.3 Statistical Analysis and Results for the twelve Z-sensors of the ME+2 disk

The characteristic response curve is the measure of the output voltage against the distance moved. The results of the fit (continuous line) are shown in Figure 3.23.

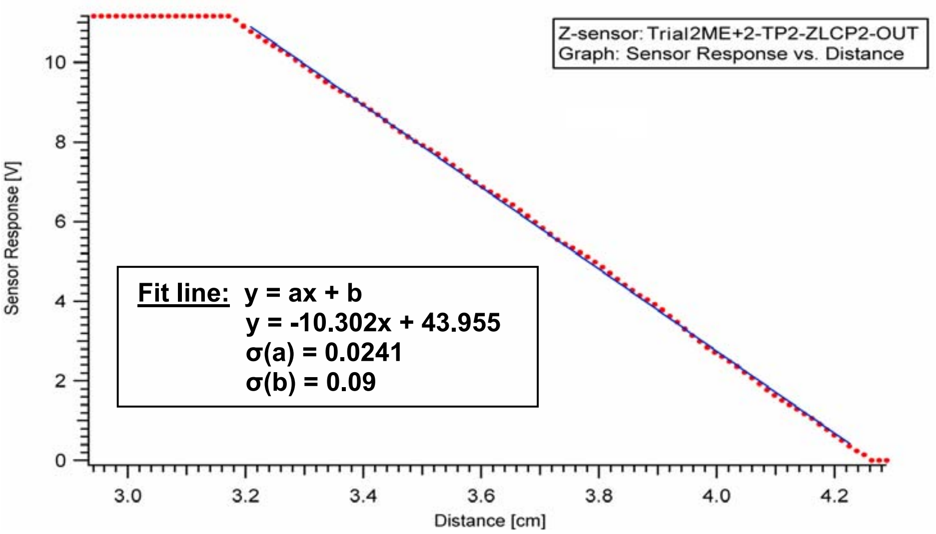

Figure 3.23 Output response of one of the sensors as a function of the distance.

The results of the uncertainty in the relative changes in distance, based on the Histogram of the slope (Figure 3.24), lead to a sensor-to-sensor variation on slopes of 0.63 %. The sensor-to-sensor variation on the relative statistical error on the Y-intercept as derived from the linear fits has a typical Gaussian profile at a relative percent error of 0.019% with a standard deviation equal to 0.007% (Figure 3.25).

A second analysis takes into consideration the variation in the reference voltage for each measurement by defining a Ratio, equal to the sensor response divided by the reference voltage. The sensor-to-sensor variation in the slope for Z sensors for the Ratio is 0.62% (Figure 3.26).

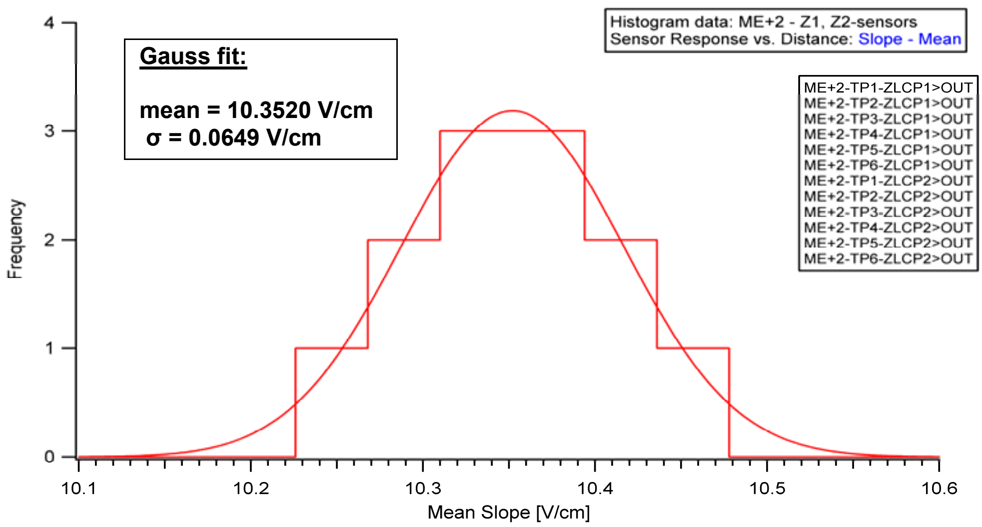

Figure 3.24 Histogram of the slopes (V/cm) for all Z sensors of the ME+2 disk

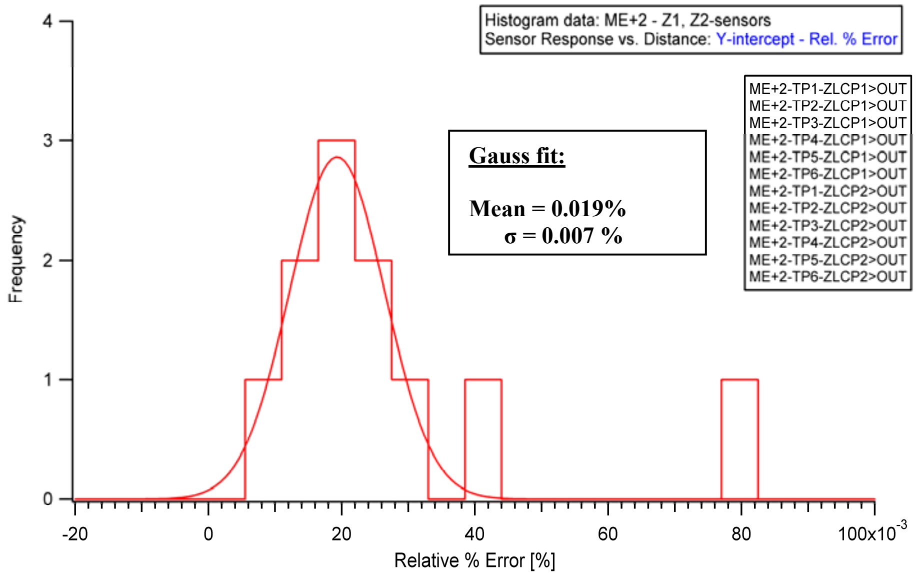

Figure 3.25 Histogram of relative statistical errors on the Y-intercept of ME+2 R sensors

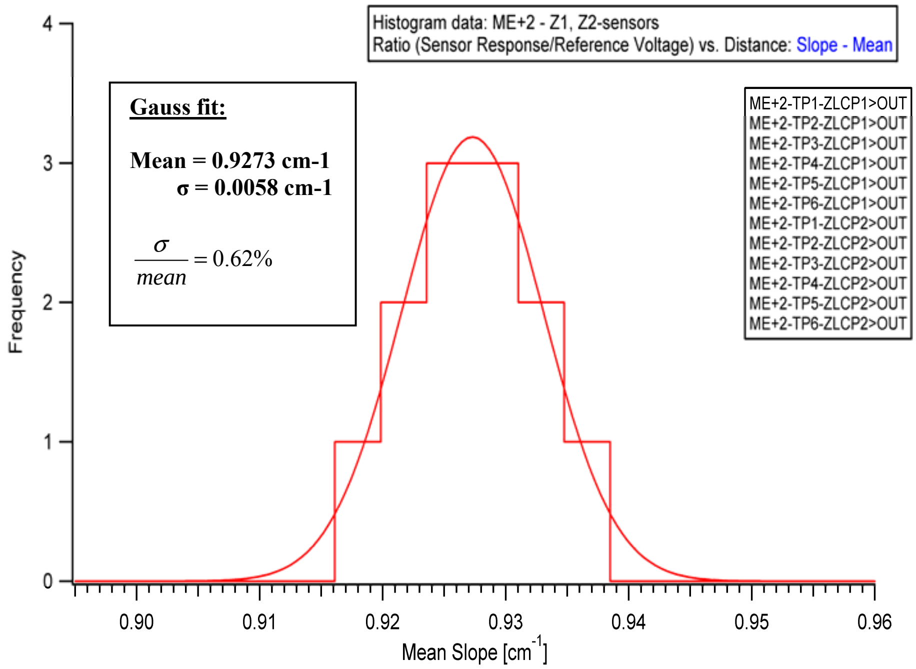

Figure 3.26 Histogram of the slopes for V/Vref of ME+2 R sensors

3.4 Inclinometers

As mentioned before, six types of Inclinometers monitor each disk. Every sensor has to be calibrated. A study of the uncertainty in the absolute zero degree calibration will be followed by a comparison of our calibration results with the manufacturer's specifications.

3.4.1 Uncertainty in the zero degree Inclinometer calibration

Initial zero degree level. The rotary laser level is adjusted to fit the line marked on the wall. The width of the laser level on the wall leads to an uncertainty in our zero degree level. The Inclinometer is moved until the reflected laser beam fits the upper and the lower part of our reference zero degree level and simultaneously the sensor response is recorded. Plotting the frequency distribution of the Sensor Response (Figure 3.27) allows us to determine the uncertainty in our zero level to be $\delta_\theta = \pm 0.020^\circ$.

$$\delta_\theta = \frac{0.0051V}{0.246V/^\circ} = 0.020^\circ, \text{ where}$$

average scale factor for -15° = $0.246V/^\circ$

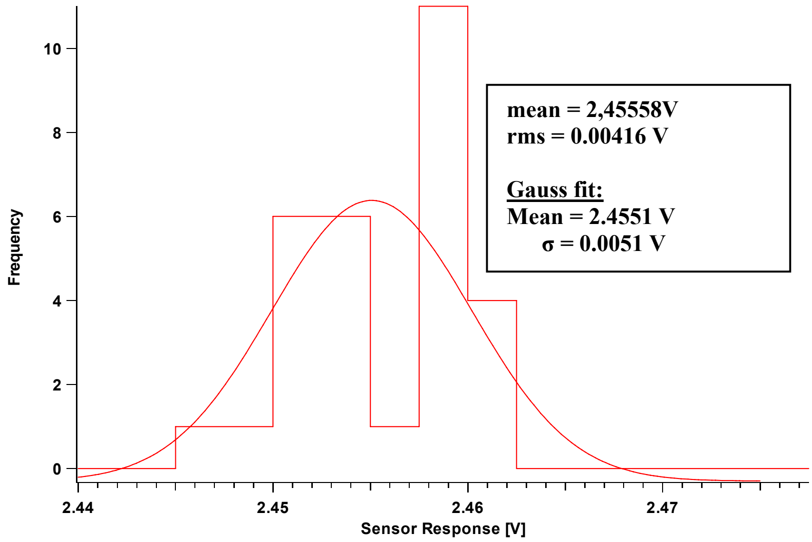

Figure 3.27 Histogram of 30 measurements of the Sensor Response for the zero degree measurement

Calibration of stepper motor. The stepper motor accuracy is estimated to be:

$\delta\theta_{[STEPMOTOR]} = \pm 0.0027°$ in the positive direction and

$\delta\theta_{[STEPMOTOR]} = \pm 0.0018°$ in the negative direction

$$\delta_\theta = \left(\frac{\sigma_{<slope>}}{<slope>}\right) * (range), where$$
$$<slope> = 13.526° / cm \quad + direction, x\, axis$$
$$\sigma_{<slope>} = 0.040° / cm, \text{ and}$$
$$<slope> = 14.522° / cm \quad - direction, x\, axis$$
$$\sigma_{<slope>} = 0.029° / cm$$
$$range = 0.93 cm$$

In table 3.6, the stepper motor accuracy is estimated for the X and Y axis and for each direction.

	X axis		Y axis	
	+	-	+	-
δθ [STEPMO	0.0027	0.0018	0.0022	0.0047

Table 3.6 Stepper motor accuracy in the X and Y axis and for each direction

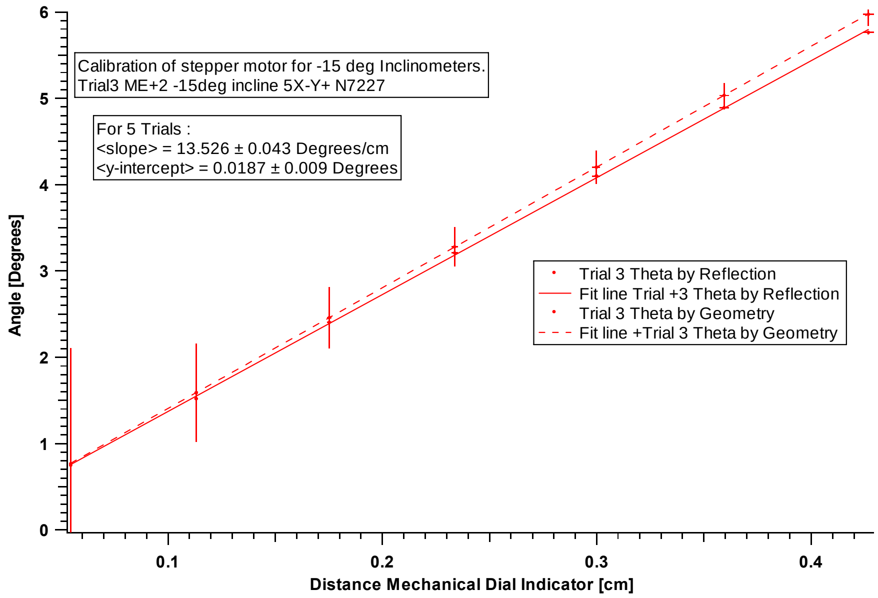

Figure 3.28 Correlation between the distances moved and measured by the mechanical dial indicator and the tilt. Error bars represent the propagated error in the angle calculated by geometry and in the angle calculated by reflection for each data point.

The errors for each measured angle are calculated by the method of propagation of error. The propagated error for the angle calculated by reflection was calculated using this formula:

$$\sigma_{\theta_R} = \left(\frac{-1}{1+\left(\frac{h}{L}\right)^2} \right) \left(\sqrt{\left(\frac{\sigma_h}{h}\right)^2 + \left(\frac{\sigma_L}{L}\right)^2} \right) \left(\frac{h}{L}\right)$$

For the angle calculated by geometry, the propagated error formula is:

$$\sigma_{\theta_G} = \left(\frac{-1}{1+\left(\frac{\Delta x + x_0}{y}\right)^2} \right) \left(\sqrt{\left(\frac{\sigma_{\Delta x + x_0}}{\Delta x + x_0}\right)^2 + \left(\frac{\sigma_y}{y}\right)^2} \right) \left(\frac{\Delta x + x_0}{y} \right)$$

As shown in figure 3.28, the propagated error in the angle measured by geometry is larger by a factor of 10. The correlation between the angle measured by reflection and the distance measured by the mechanical dial indicator is equal to 13.526 ± 0.0187 °/cm for the positive x direction.

In table 3.7, the correlation between Δx and Δθ for each axis and direction is presented.

	X axis		Y axis	
	+	-	+	-
Δθ/ Δx	13.526	14.522	13.371	14.13
$\Delta\theta_0$	0.0187	0.009	0.0174	0.017

Table 3.7 The correlation between Δθ and Δx and the value of $\Delta\theta_0$

The estimated uncertainty in the inclinometers sensors was obtained from these tests. The total uncertainty for our system in absolute zero degree level calibration can be calculated using the equation:

$\sqrt{\delta^2_{\theta\,\mathrm{ZEROLINE}} + \delta^2_{\theta\,\mathrm{STEPMOTOR}}}$ = 0.020º for positive and negative direction for X and Y axis. A summary of the uncertainty in the Inclinometers Calibration is shown in Table 3.8.

Random uncertainties:

- Initial 0º level with rotary laser level (for all Inclinometer)
± 0.020º

Systematic uncertainties:

- **Calibration of stepper motor for X axis**
  in the + direction ± 0.0027º

	X axis		Y axis	
	+	-	+	-
$\delta\theta$ [STEPMOTOR]	0.0027	0.0018	0.0022	0.0047

Table 3.8 A summary of the uncertainty in the absolute angle for Inclinometers

3.4.2 Calibration precision for -15º Inclinometers for ME+2 disk

We calibrated the output response (V) of each sensor and quantify the statistical error in the relative changes in angle and the statistical error in the laser level.

3.4.2.1 -15º Inclinometers in the positive X direction

5 trials were taken for calibrating -15º inclinometers in the positive X direction for ME+2 disk. A 0.19relative error in the slopes [Volt/º] (Figure 3.29) quantifies a statistical error in measuring relative changes in angle equal to ±0.023º. This variation is calculated using this formula:

$$\sigma_{\Delta\theta} = \left(\frac{\sigma < slope >}{< slope >} \right) (Range)$$

$$\sigma_{\Delta\theta} = \left(\frac{0.19}{100} \right) * 12 = 0.023^{\circ}$$

The systematic uncertainty due to the precision of the rotary laser level is determined by plotting the frequency distribution of the y-intercept (V) revealing a systematic uncertainty of 0.13º (Figure 3.30):

$$\sigma_{\theta} = \frac{0.0290\text{V}}{0.2293V/^{\circ}} = 0.13^{\circ}$$

3.4.2.2 -15º Inclinometers in the negative X direction

The histogram of the slope (Figure 3.31) reveals a relative error of 0.46% determining a variation on the relative changes in angle equal to $\sigma_{\Delta\theta} = 0.055°$. A systematic uncertainty in the laser level is determined by plotting the frequency distribution of the y-intercept (V/º) (Figure 3.32) and is calculated using the following formula

$$\sigma_{\theta} = \frac{0.0279\text{V}}{0.2501V/°} = 0.11°.$$

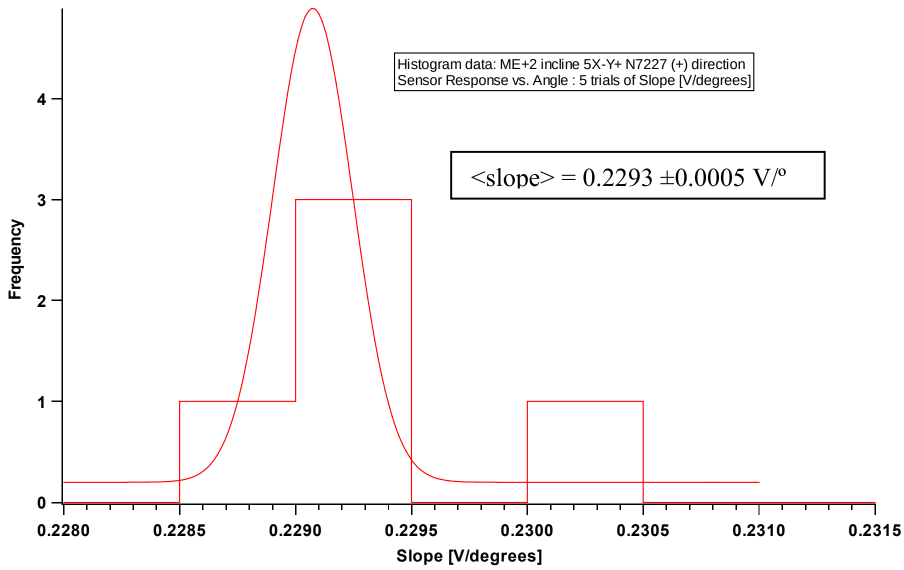

Figure 3.29 Histogram of 5 measurements of the slope [V/º] for ME+2 inclinometers 5X-Y N7227 in the positive X direction.

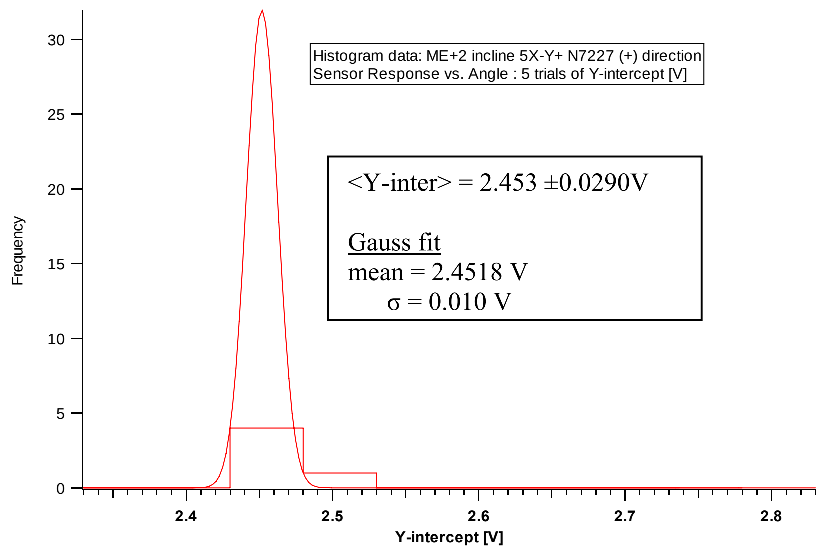

Figure 3.30 Histogram of 5 measurements of the Y-intercept [V] for ME+2 inclinometers 5X-Y N7227 in the positive X direction.

.

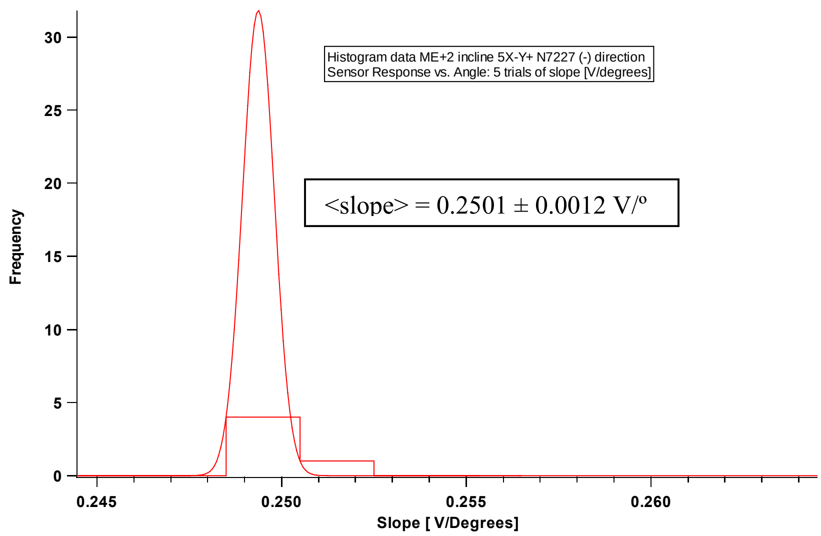

Figure 3.31 Histogram of 5 measurements of the slope [V/º] for ME+2 incline 5X-Y N7227 in the negative X direction.

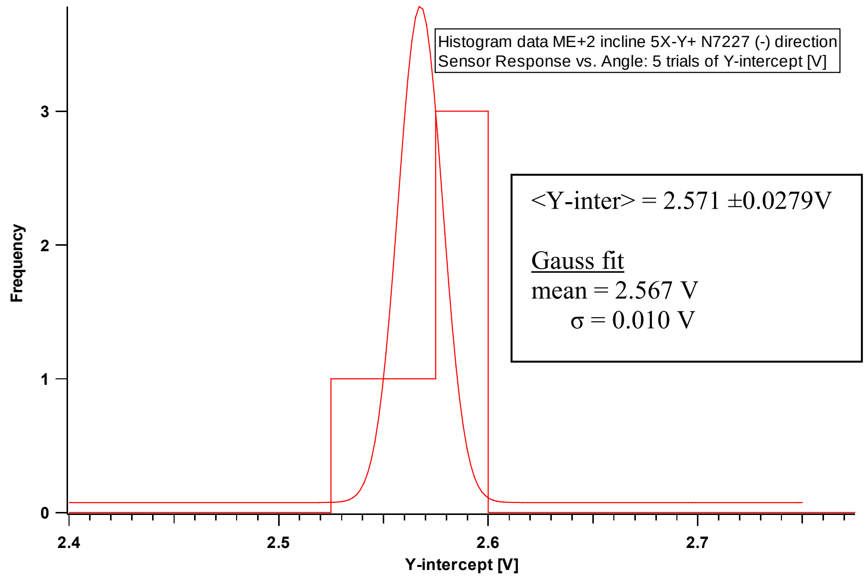

Figure 3.32 Histogram of 5 measurements of the Y-intercept [V] for ME+2 incline 5X-Y N7227 in the negative X direction.

Using the same method, the uncertainty in σ_θ *and* $\sigma_{\Delta\theta}$ for -15 degrees inclinometers is estimated in the X and Y direction and for each direction. The table 3.9 summarizes the uncertainties in the relative change in the angle and the uncertainties in absolute zero level.

	X axis		Y axis	
Direction	+	-	+	-
$\sigma_{\Delta\theta}$ [º]	0.024	0.055	0.015	0.06
σ_θ [º]	0.13	0.11	0.12	0.097

Table 3.9 Uncertainties in angle $\sigma_{\Delta\theta}$ from slopes and in absolute zero level σ_θ.

3.4.3 Calibration Results for ME+2 -15 º Inclinometers

Figures 3.33-3.36 show the Scale Factor calibration results for one inclinometer: ME+2 -15º inclinometer. This inclinometer was calibrated by plotting its sensor response against the tilt in the positive and negative X and Y directions. Then, we compared the Scale Factor [º/Volt] with those quoted in the manufacturer's technical (Table 3.10) report.

X direction

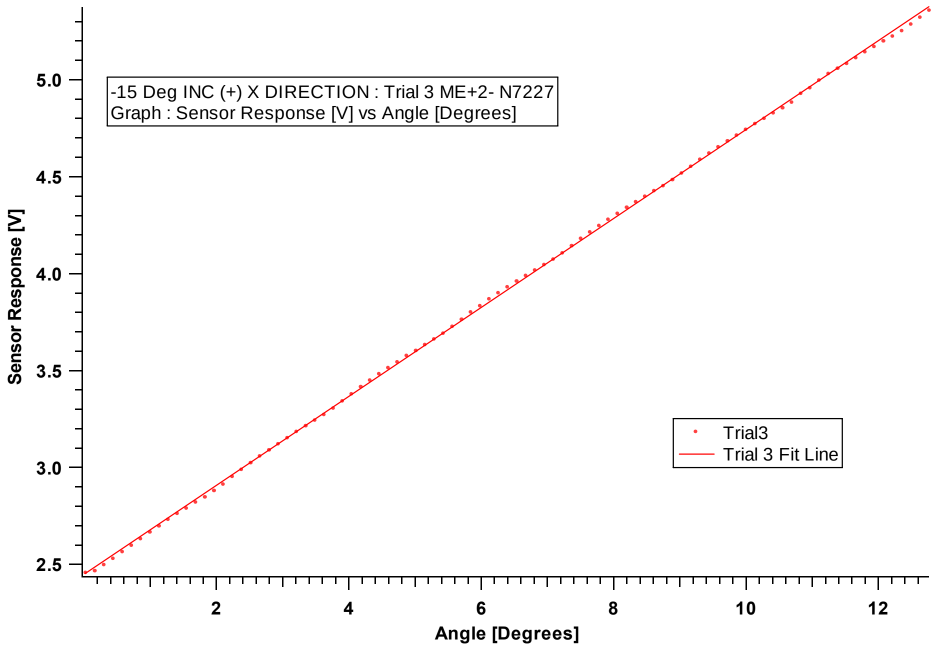

Figure 3.33 Sensor Response [V] vs Angle [Degrees] calculated from linear displacement in the + X direction

	Scale Factor [Degrees/Volt]
	(+) X direction
Geomechanics Technical Note	4.236
FIT Calibration with Temperature Factor coefficient	4.0314 ± 0.0003 (stat)
	(-) X direction
Geomechanics Technical Note	4.243
FIT Calibration with Temperature Factor coefficient	4.394 ± 0.0007 (stat)

Table 3.10 Results for Scale Factor [Degrees/Volt] for ME+2 -15 º inclinometer in the positive and negative X direction.

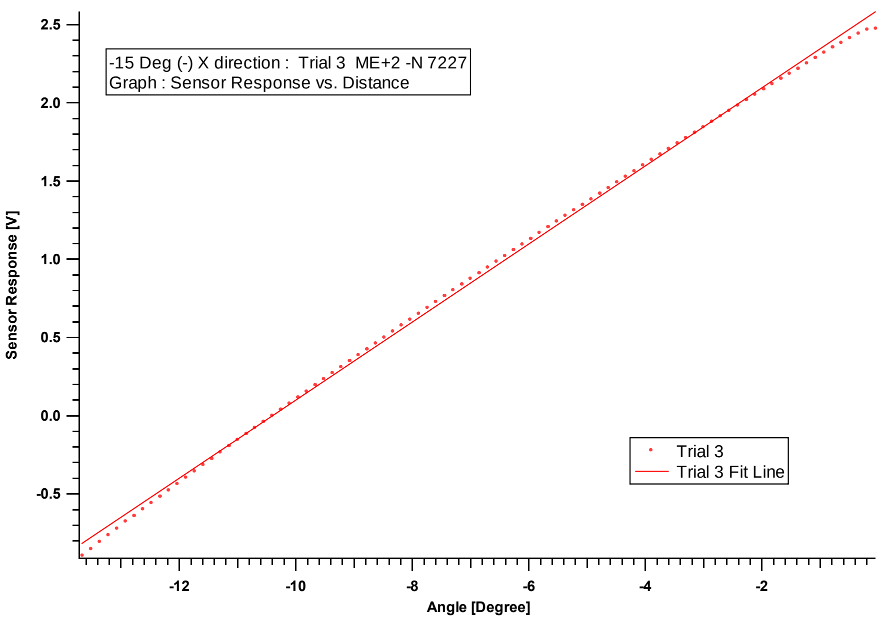

Figure 3.34 Sensor Response [V] vs Angle [Degrees] calculated from linear displacement in the - X direction

Y direction

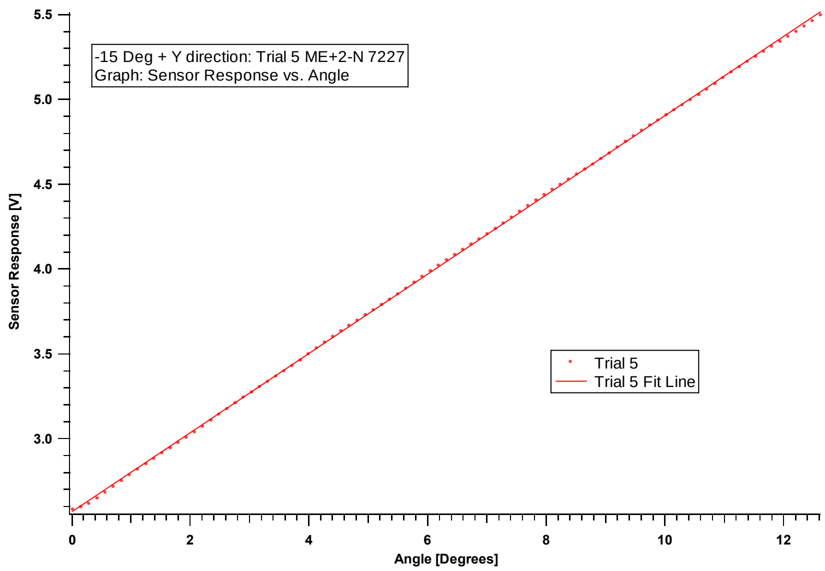

Figure 3.35 Sensor Response [V] vs Angle [Degrees] calculated from linear displacement in the + Y direction

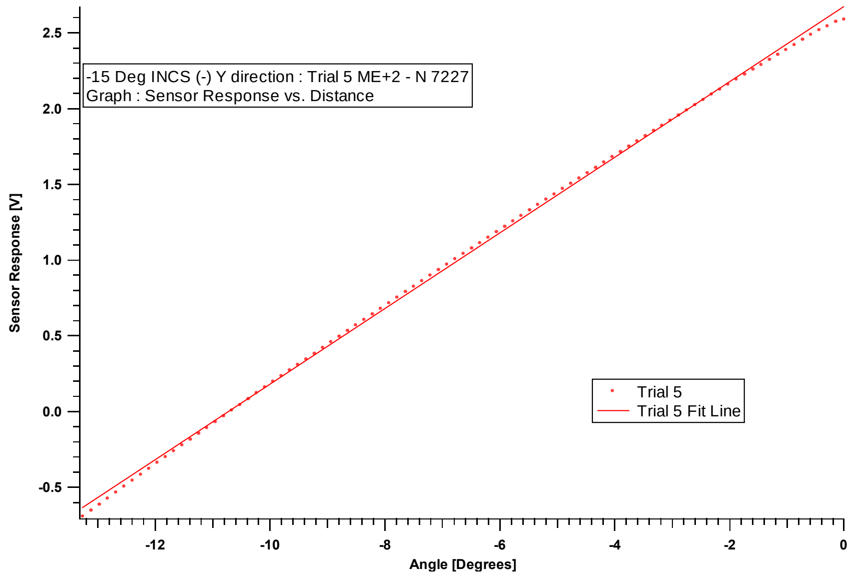

Figure 3.36 Sensor Response [V] vs Angle [Degrees] calculated from linear displacement in the - Y direction

	Scale Factor [Degrees/Volt]
	(+) Y dire ction
Geomechanics Technical Note	4.243
FIT Calibration with Temperature Factor Correction	4.021 ± 0.0006 (stat)
Geomechanics Technical Note	(-) Y direction
FIT Calibration with Temperature Factor Correction	4.243 4.3098 ± 0.0109 (stat)

Table 3.11 Results for Scale Factor [Degrees/Volt] for ME+2 -15º inclinometer in the positive and negative Y direction

3.4.3 Statistical Analysis for eight (-15º) inclinometers in positive and negative X direction.

The sensor-to-sensor variation on the slope for positive and negative directions (Figure 3.37) has Gaussian profiles one representing most of the inclinometers calibrated in the positive direction with a relative percent error of

3.3% with a standard deviation equal to 0.0079 V/degree. As shown in Figure 3.37, the left Gaussian fit represents the slope of all -15 º inclinometers for the positive direction plus two -15 º inclinometers for the negative direction. The right histogram represents six -15 º inclinometers for the negative direction. The histogram of the relative % errors for the eight clinometers (Figure 3.38) at the positive and negative angle reveals a 0.55 % relative error in the slope.

Measuring the variation in the absolute angle by plotting the frequency distribution of the Y-intercept (Figure 3.39) for the eight -15 º Inclinometers give us a relative error of 7.7% with a standard deviation equal to 0.201 [V]. The Histogram of the relative % error (Figure 3.40) for the eight clinometers in the positive and negative direction reveals a small relative error of 0.13% in the Y - intercept. Plotting the histogram of the mean reference voltage (Figure 3.41) for the eight Inclinometers disk shows a variation in the voltage regulator of .016%.

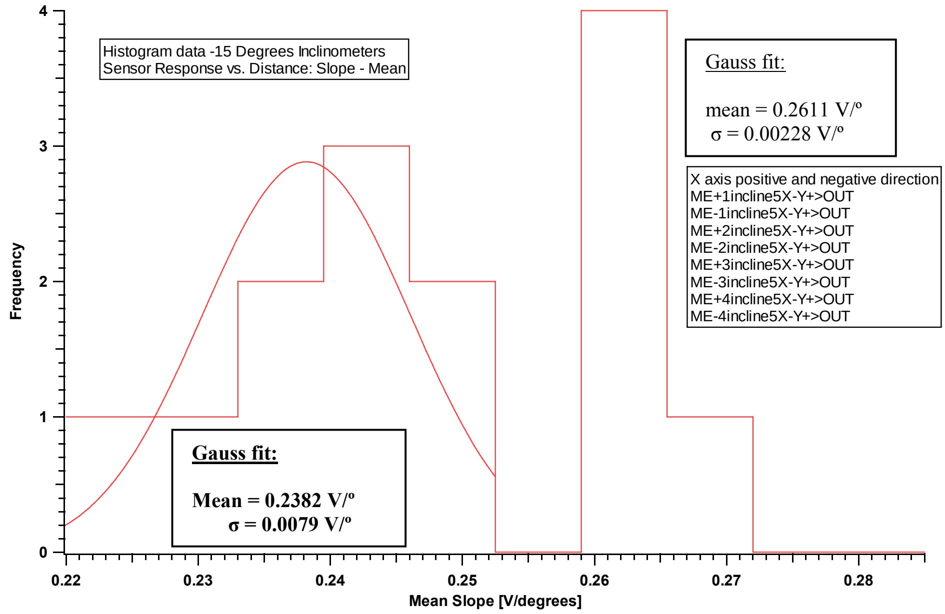

Figure 3.37 Histogram of the slope (V/º) for all -15º inclinometers in ±x direction.

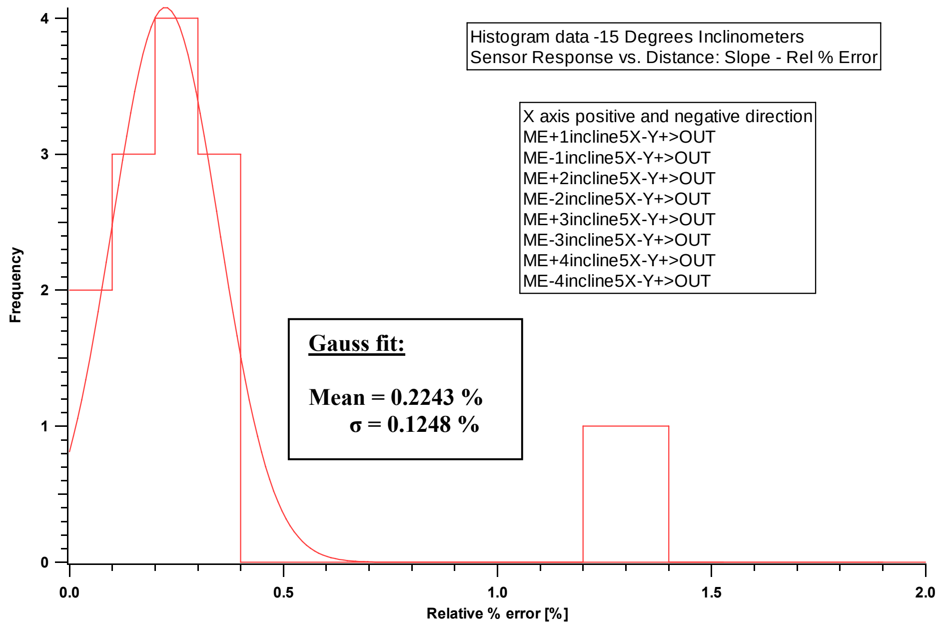

Figure 3.38 Histogram of the relative statistical errors on the Y-intercept (V/º) for all -15º inclinometers in the ±x directions

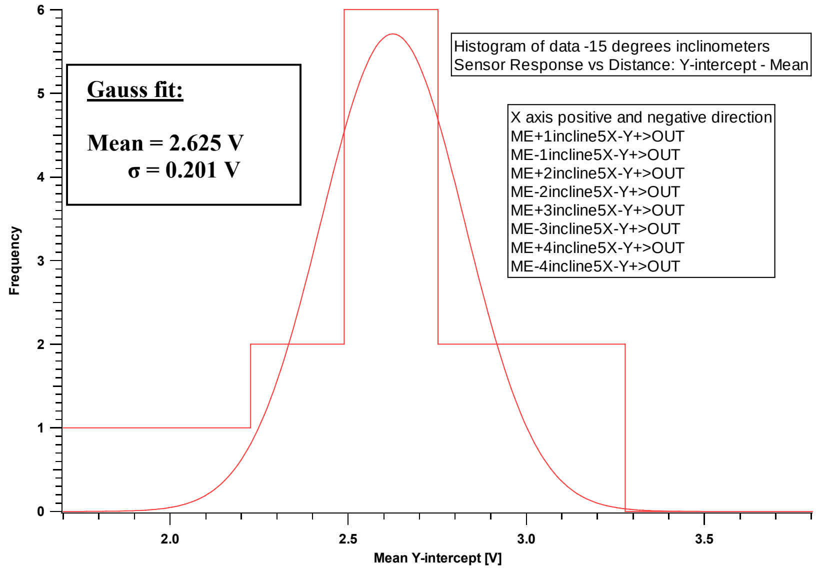

Figure 3.39 Histogram of the Y-intercept (V) for all -15° inclinometers in the ± x directions

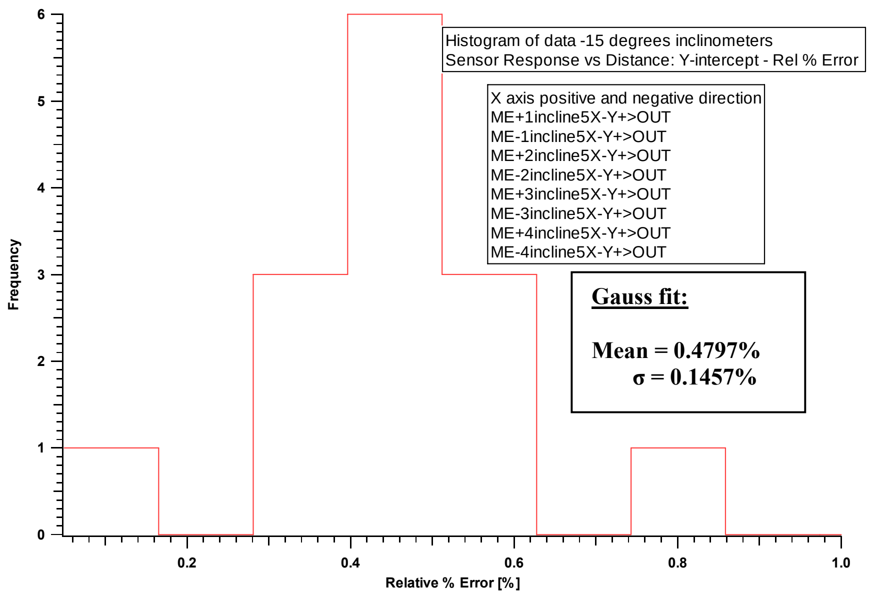

Figure 3.40 Histogram of the relative statistical error on the Y-intercept (V) for all -15° inclinometers in the ± x directions

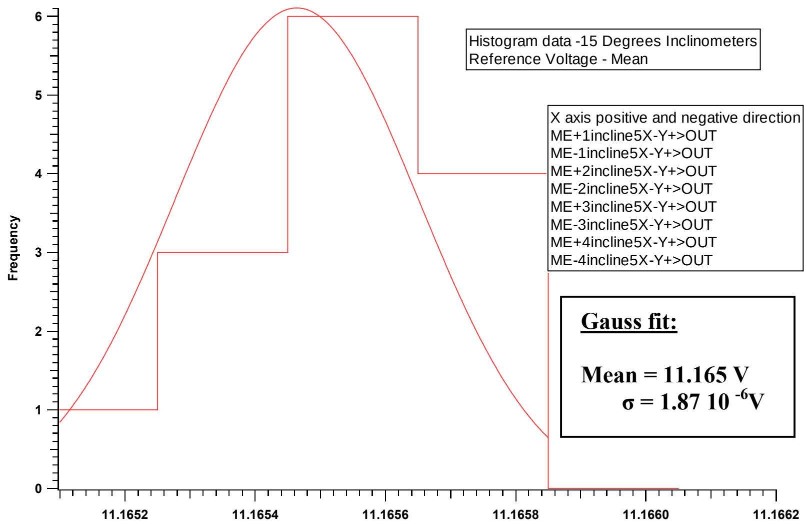

Figure 3.41 Histogram of the Mean Reference Voltage (V) for all -15º inclinometers in the ± x directions

3.4.4 Statistical Analysis for eight (-15º) inclinometers in the Y axis

The variation of the slope for the eight inclinometers of -15º angle type represented by the histogram of the mean of the slopes for the eight inclinometers has a relative error of 4.5 % with a standard deviation equal to 0.011V/º. This larger deviation can be explained by the fact that each inclinometer doesn't have the same value (Figure 3.42) but their mean slope in the positive and negative direction are close. That's why we observed a large relative statistical error for the frequency distribution of the relative error in the slope (Figure 3.43).

As shown in Figure 3.44, the deviation in the absolute angle for -15 º inclinometers in the Y directions gives us a sensor-to-sensor variation of 10%. As previously mentioned, since each (ME) inclinometer has its intrinsic Scale Factor

[V/º], the distribution of all (ME) -15º inclinometers has a large variation in the Y-intercept. Figure 3.45 demonstrates that each inclinometer has their Y-intercept mean in the negative and positive direction relatively close but spread from 2.0V to 2.93 V. The variation of the mean reference voltage shown in Figure 3.46 reveals a small deviation less than 0.0025%.

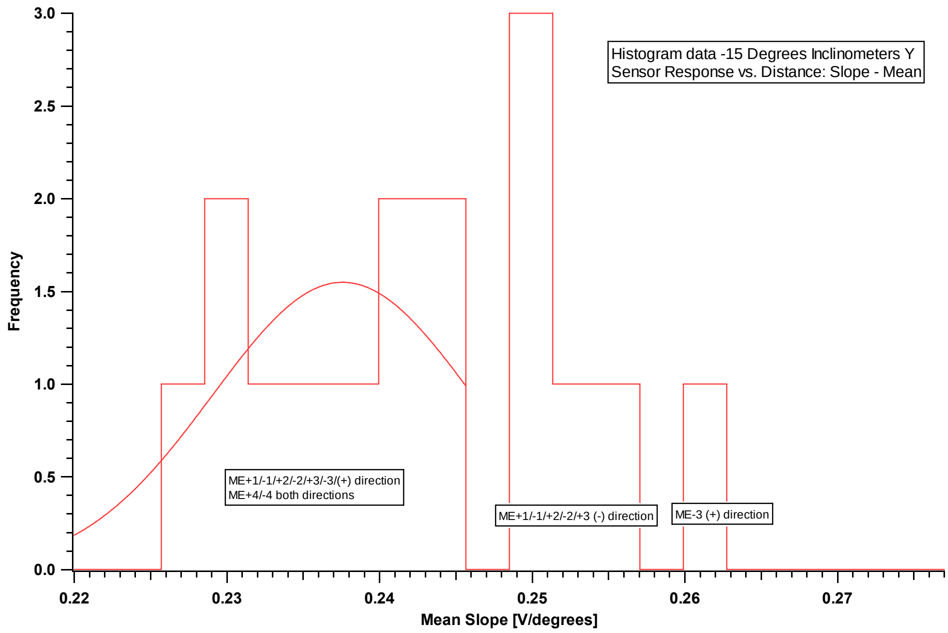

Figure 3.42 Histogram of the slope (V/º) for all -15º inclinometers

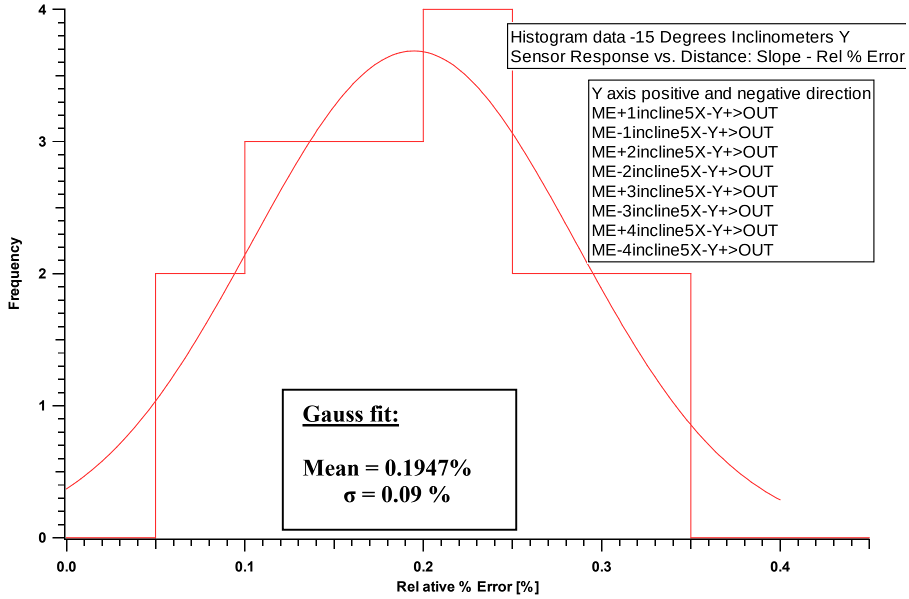

Figure 3.43 Histogram of the relative statistical error on the Y-intercept (V/º) for all -15º inclinometers

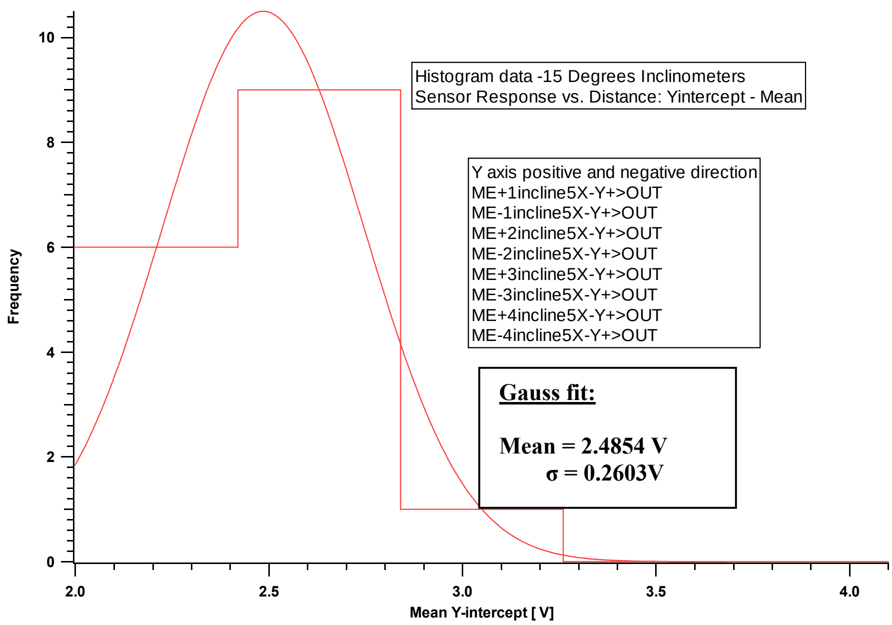

Figure 3.44 Histogram of the Y-intercept (V) for all -15º inclinometers

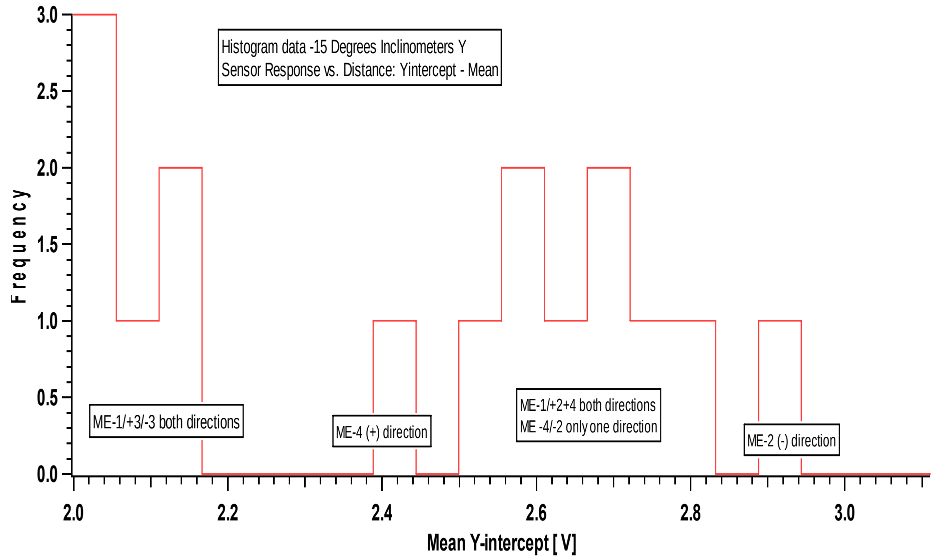

Figure 3.45 Histogram of the mean Y-intercept (V) for all -15º inclinometers

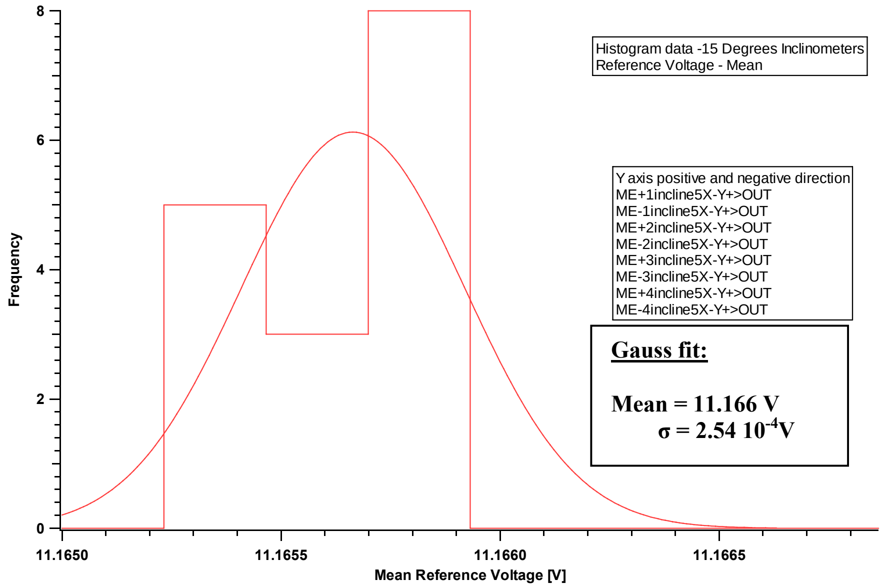

Figure 3.46 Histogram of the Mean Reference Voltage (V) for all -15º inclinometers

Chapter 4 Summary and Future directions

The thesis presents a flexible and easy way to calibrate linear and angular sensors. The aim of the author was to find the most efficient way to build a multi-task test bench allowing us to calibrate these different types of sensors. A control interface using LabVIEW was constructed in order to control the test bench and to acquire any sensor output data. This method of calibration provides a direct measurement of the sensor response. All calibrations are well within the calibration precisions required by CMS.

The work involved an understanding of the overall precision of each sensor calibration. Five trials will be sufficient to achieve a reasonably small uncertainty over the fully calibrated distance. The sensor response and the related Reference Voltage for each trial were measured and analyzed. For each trial a fit line, characterized by its slope and its y-intercept, is recorded and the average of the 5 trials gives us our average linear fit describing the linear output of each sensor. These measurements will be used as input for reconstruction and monitoring of the CSC chambers. A statistical analysis of the sensor-to-sensor variation is done for all R sensors and Z sensors for the ME+2 disk. For inclinometers, it has been shown that the determination of the zero degree level is very sensitive to variations in the X and Y direction.

The future work will be to finish calibrating all sensors and making the calibration data available to the reconstruction and monitoring software.

References

[1] R.Zitoun, “Introduction a la physique des particules”, édition Dunod (2001).

[2] CERN web site http://www.bulletin.cern.ch/.

[3] F.Gianotti, “Physics at Large Hadron Collider”, CERN, 73-75.

[4] The CMS collaboration, “The Muon Project Technical Design Report”, CERN/LHCC 97-32.

[5] R.Lee, “Simulation and study of the CMS endcap muon alignment scheme” (2002).

[6] C.Grupen, “ Particle Detectors”, Cambridge University Press (1996).

[7] F.Sauli, “Principle of operation of multi wire proportional and drift chambers” (CERN 77-09, may 1977).

[8] The GlobalSpec Engineering, Inc web site www.globalspec.com/.

[9] Unimeasure, Inc web site http://unimeasure.com/.

[10] David Eartly, private communications.

[11] ETI Systems, Inc http://www.etisystems.com/.

[12] Applied Geomechanics Inc web site http:// www.geomechanics.com/.

[13] National Instrument website http://ni.com/.

[14] LabVIEW, “Data Acquisition Basis Manual, National Instruments”.

[15] Oriental Motor USA corp. web site www.orientalmotor.com/.

[16] John Mandel, “The Statistical Analysis of Experimental Data”, Dover (1984).

[17] P.Bevington, D.Robinson, Data Reduction and Error Analysis for the Phyiscal Sciences, Mc Graw Hill (2003).

Appendix A

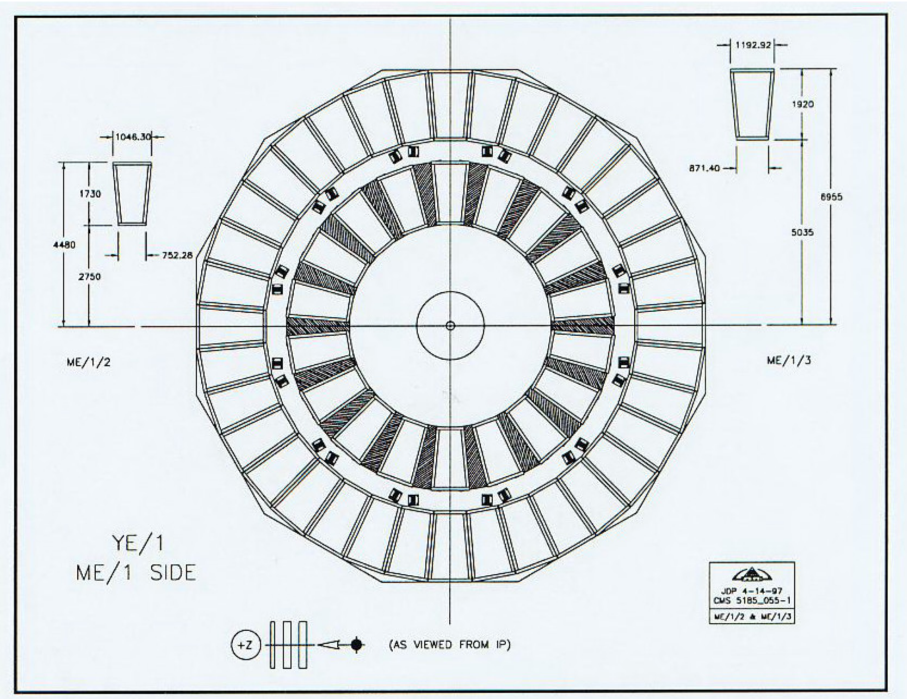

The position of the Cathode Strip Chambers on ME±1 disks [4]

Appendix B

Clinometers Position

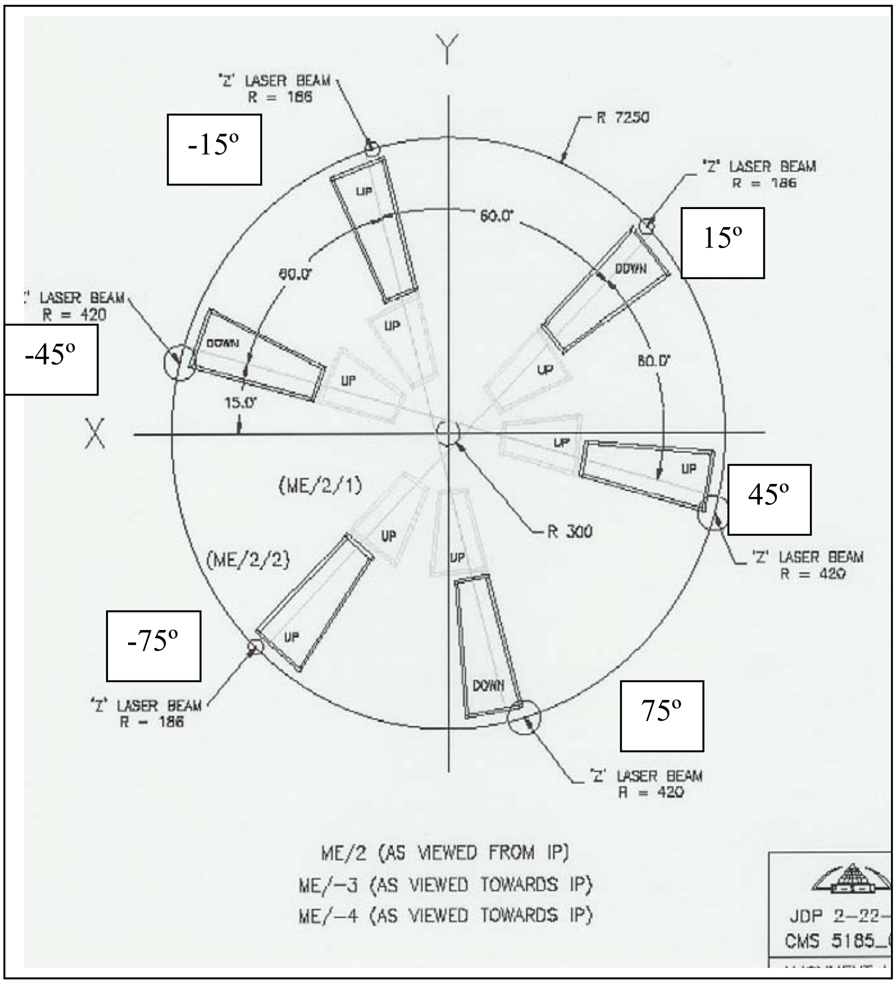

Cathode Strip chambers arrangement and placement on the iron disk.
They are arranged to form four disks called stations ME1/2/3/4 [4]

Appendix C

Data Acquisition Technical Support

Measurement Characteristics[8]

DC Voltage	
Measurement Method	Continuously Integrating Multi-slope III A-D Converter
A-D Linearity	0.0002% of reading + 0.0001 % of range
Input Resistance	
100 mV, 1 V, 10 V ranges	Selectable 10 MΩ or > 10,000 MΩ
100 V, 300 V ranges	10 MΩ ± 1%
Input Bias Current	< 30 pA at 25°C
Input Protection	300 V all ranges
True RMS AC Voltage	
Measurement Method	AC coupled True RMS — measures the AC component of the input with up to 300 Vdc of bias on any range
Crest Factor	Maximum of 5:1 at Full Scale
Additional Crest Factor Errors (non-sinewave)	Crest Factor 1-2 0.05 % of reading Crest Factor 2-3 0.15 % of reading Crest Factor 3-4 0.30 % of reading Crest Factor 4-5 0.40 % of reading
Input Impedance	1 MΩ ± 2% in parallel with 150 pF
Input Protection	300 Vrms all ranges
Resistance	
Measurement Method	Selectable 4-wire or 2-wire Ohms Current source referenced to LO input
Offset Compensation	Selectable on 100Ω, 1kΩ, 10kΩ ranges
Maximum Lead Resistance	10% of range per lead for 100 Ω and 1 kΩ ranges. 1 kΩ on all other ranges
Input Protection	300 V on all ranges
Frequency and Period	
Measurement Method	Reciprocal counting technique
Voltage Ranges	Same as AC Voltage function
Gate Time	1s, 100 ms, or 10 ms
Measurement Timeout	Selectable 3 Hz, 20 Hz, 200 Hz LF limit
DC Current	
Shunt Resistance	5 Ω for 10 mA, 100 mA; 0.1 Ω for 1 A
Input Protection	1A 250 V fuse on 34901A module
True RMS AC Current	
Measurement Method	Direct coupled to the fuse and shunt. AC coupled True RMS measurement (measures the ac component only)
Shunt Resistance	5 Ω for 10 mA; 0.1 Ω for 100 mA, 1 A
Input Protection	1A 250 V fuse on 34901A module
Thermocouple	
Conversion	ITS-90 software compensation
Reference Junction Type	Internal, Fixed, or External
Open thermocouple Check	Selectable per channel. Open >5kΩ
Thermistor	44004, 44007, 44006 series
RTD	α = 0.00385 (DIN) and α = 0.00391

Measurement Noise Rejection 60 (50) Hz[1]

dc CMRR	140 dB
ac CMRR	70 dB
Integration Time	**Normal Mode Rejection[2]**
200 plc/3.33s (4s)	110 dB[3]
100 plc/1.67s (2s)	105 dB[3]
20 plc/333 ms (400 ms)	100 dB[3]
10 plc/167 ms (200 ms)	95 dB[2]
2 plc/33.3 ms (40 ms)	90 dB
1 plc/16.7 ms (20 ms)	60 dB
< 1 plc	0 dB

Operating Characteristics[4]

Single Channel Measurement Rates[5]

Function	Resolution[9]	reading/s
dcV, 2-wire Resistance	6½ digits (10 plc)	6 (5)
	5½ digits (1 plc)	57 (47)
	4½ digits (0.02 plc)	490
Thermocouple	0.1°C (1 plc)	49 (47)
	(0.02 plc)	280
RTD, Thermistor	0.01°C (10 plc)	6 (5)
	0.1°C (1 plc)	47 (47)
	1°C (0.02 plc)	280
acV	6½ Slow (3 Hz)	0.14
	6½ Med (20 Hz)	1
	6½ Fast (200 Hz)	8
	6½[6]	100
Frequency, Period	6½ digits (1s gate)	1
	5½ digits (100 ms)	9
	4½ digits (10 ms)	70

System Speeds[7]

INTO Memory	**ch/s**
single channel dcV	490
34902A scanning dcV	250
34907A scanning digital in	250
34902A scanning dcV with scaling & 1 alarm fail	220
34907A scanning totalize	170
34902A scanning temperature	160
34902A scanning acV[6]	100
34902A scanning dcV/Ohms on alternate channels	90
34901A/34908A scanning dcV	60
INTO and OUT of memory to GPIB or RS-232 (init, fetch)	
34902A scanning dcV	180
34902A scanning dcV with timestamp	150
OUT of memory to GPIB[10]	
Readings	800
Readings with timestamp	450
Readings with all format options ON	310
OUT of memory to RS-232	
Readings	600
Readings with timestamp	320
Readings with all format options ON	230
DIRECT to GPIB or RS-232	
single channel dcV	440
34902A scanning dcV	200
single channel MEAS DCV 10 / MEAS DCV 1	25
single channel MEAS DCV/ MEAS OHMS	12

[1] For 1 KΩ unbalance in LO lead
[2] For power line frequency ±0.1%
[3] For power line frequency ±1% use 80 dB or ±3% use 60 dB
[4] Reading speeds for 60 Hz and (50 Hz) operation
[5] For fixed function and range, readings to memory, scaling and alarms off, AZERO OFF
[6] Maximum limit with default settling delays defeated
[7] Speeds are for 4½ digits, delay Ø, display off, autozero off. Using 115 kbaud RS-232 setting
[8] Isolation voltage (ch - ch, ch - earth) 300 Vdc, ac rms
[9] 6½ digits = 22 bits, 5½ digits = 18 bits, 4½ digits = 15 bits
[10] Assumes relative time format (time since start of scan)

15

Data sheet specifications Agilent 34970 A (1) [13]

Accuracy Specifications ±(% of reading + % of range)[1]

Includes measurement error, switching error, and transducer conversion error

	Range[3]	Frequency, etc.	24 Hour[2] 23°C±1°C	90 Day 23°C±5°C	1 Year 23°C±5°C	Temperature Coefficient 0°C–18°C, 28°C–55°
DC Voltage						
	100.0000 mV		0.0030 + 0.0035	0.0040 + 0.0040	0.0050 + 0.0040	0.0005 + 0.0005
	1.000000 V		0.0020 + 0.0006	0.0030 + 0.0007	0.0040 + 0.0007	0.0005 + 0.0001
	10.00000 V		**0.0015 + 0.0004**	**0.0020 + 0.0005**	**0.0035 + 0.0005**	**0.0005 + 0.0001**
	100.0000 V		0.0020 + 0.0006	0.0035 + 0.0006	0.0045 + 0.0006	0.0005 + 0.0001
	300.000 V		0.0020 + 0.0020	0.0035 + 0.0030	0.0045 + 0.0030	0.0005 + 0.0003
True RMS AC Voltage[4]						
	100.0000 mV	3 Hz–5 Hz	1.00 + 0.03	1.00 + 0.04	1.00 + 0.04	0.100 + 0.004
	to 100.0000V	5 Hz–10 Hz	0.35 + 0.03	0.35 + 0.04	0.35 + 0.04	0.035 + 0.004
		10 Hz–20 kHz	**0.04 + 0.03**	**0.05 + 0.04**	**0.06 + 0.04**	**0.005 + 0.004**
		20 kHz–50 kHz	0.10 + 0.05	0.11 + 0.05	0.12 + 0.05	0.011 + 0.005
		50 kHz–100 kHz	0.55 + 0.08	0.60 + 0.08	0.60 + 0.08	0.060 + 0.008
		100 kHz–300 kHz[5]	4.00 + 0.50	4.00 + 0.50	4.00 + 0.50	0.20 + 0.02
	300.0000V	3 Hz–5 Hz	1.00 + 0.05	1.00 + 0.08	1.00 + 0.08	0.100 + 0.008
		5 Hz–10 Hz	0.35 + 0.05	0.35 + 0.08	0.35 + 0.08	0.035 + 0.008
		10 Hz–20 kHz	0.04 + 0.05	0.05 + 0.08	0.06 + 0.08	0.005 + 0.008
		20 kHz–50 kHz	0.10 + 0.10	0.11 + 0.12	0.12 + 0.12	0.011 + 0.012
		50 kHz–100 kHz	0.55 + 0.20	0.60 + 0.20	0.60 + 0.20	0.060 + 0.020
		100 kHz–300 kHz[5]	4.00 + 1.25	4.00 + 1.25	4.00 + 1.25	0.20 + 0.05
Resistance[6]						
	100.0000Ω	1 mA current source	0.0030 + 0.0035	0.008 + 0.004	0.010 + 0.004	0.0006 + 0.0005
	1.000000 kΩ	1 mA	0.0020 + 0.0006	0.008 + 0.001	0.010 + 0.001	0.0006 + 0.0001
	10.00000 kΩ	**100 µA**	**0.0020 + 0.0005**	**0.008 + 0.001**	**0.010 + 0.001**	**0.0006 + 0.0001**
	100.0000 kΩ	10 µA	0.0020 + 0.0005	0.008 + 0.001	0.010 + 0.001	0.0006 + 0.0001
	1.000000 MΩ	5.0 µA	0.002 + 0.001	0.008 + 0.001	0.010 + 0.001	0.0010 + 0.0002
	10.00000 MΩ	500 nA	0.015 + 0.001	0.020 + 0.001	0.040 + 0.001	0.0030 + 0.0004
	100.0000 MΩ	500 nA/10 MΩ	0.300 + 0.010	0.800 + 0.010	0.800 + 0.010	0.1500 + 0.0002
Frequency and Period[7]						
	100 mV	3 Hz–5 Hz	0.10	0.10	0.10	0.005
	to 300 V	5 Hz–10 Hz	0.05	0.05	0.05	0.005
		10 Hz–40 Hz	0.03	0.03	0.03	0.001
		40 Hz–300 kHz	**0.006**	**0.01**	**0.01**	**0.001**
DC Current (34901A only)						
	10.00000 mA	<0.1 V burden	0.005 + 0.010	0.030 + 0.020	0.050 + 0.020	0.002+ 0.0020
	100.0000 mA	**<0.6 V**	**0.010 + 0.004**	**0.030 + 0.005**	**0.050 + 0.005**	**0.002 + 0.0005**
	1.000000 A	<2 V	0.050 + 0.006	0.080 + 0.010	0.100 + 0.010	0.005 + 0.0010
True RMS AC Current (34901A only)						
	10.00000 mA	3 Hz–5 Hz	1.00 + 0.04	1.00 + 0.04	1.00 + 0.04	0.100 + 0.006
	and[4] 1.000000 A	5 Hz–10 Hz	0.30 + 0.04	0.30 + 0.04	0.30 + 0.04	0.035 + 0.006
		10 Hz–5 kHz	**0.10 + 0.04**	**0.10 + 0.04**	**0.10 + 0.04**	**0.015 + 0.006**
	100.0000 mA[8]	3 Hz–5 Hz	1.00 + 0.5	1.00 + 0.5	1.00 + 0.5	0.100 + 0.06
		5 Hz–10 Hz	0.30 + 0.5	0.30 + 0.5	0.30 + 0.5	0.035 + 0.06
		10 Hz–5 kHz	0.10 + 0.5	0.10 + 0.5	0.10 + 0.5	0.015 + 0.06

Temperature	Type	1-Year Accuracy[9]		Extended Range 1-Year Accuracy[9]		
Thermocouple[10]	B	1100°C to 1820°C	1.2°C	400°C to 1100°C	1.8°C	
	E	-150°C to 1000°C	1.0°C	-200°C to -150°C	1.5°C	
	J	**-150°C to 1200°C**	**1.0°C**	**-210°C to -150°C**	**1.2°C**	
	K	-100°C to 1200°C	1.0°C	-200°C to -100°C	1.5°C	0.03 °C
	N	-100°C to 1300°C	1.0°C	-200°C to -100°C	1.5°C	
	R	300°C to 1760°C	1.2°C	-50°C to 300°C	1.8°C	
	S	400°C to 1760°C	1.2°C	-50°C to 400°C	1.8°C	
	T	-100°C to 400°C	1.0°C	-200°C to -100°C	1.5°C	
RTD	R_0 from 49 Ω to 2.1 kΩ	-200°C to 600°C	0.06°C			0.003 °C
Thermistor	2.2 k, 5k, 10k	-80°C to 150°C	0.08°C			0.002 °C

[1] Specifications are for 1 hr warm-up and 6½ digits, Slow ac filter
[2] Relative to calibration standards
[3] 20% over range on all ranges except 300 Vdc and ac ranges and 1 Adc and ac current ranges
[4] For sinewave input > 5% of range. For inputs from 1% to 5% of range and < 50 kHz, add 0.1% of range additional error
[5] Typically 30% of reading error at 1 MHz, limited to 1 x 10⁸ V Hz
[6] Specifications are for 4- wire ohms function or 2-wire ohms using Scaling to remove the offset. Without scaling, add 4 Ω additional error in 2-wire Ohms function
[7] Input > 100 mV. For 10 mV to 100 mV inputs multiply % of reading error x 10
[8] Specified only for inputs >10 mA
[9] For total measurement accuracy, add temperature probe error
[10] Thermocouple specifications not guaranteed when 34907A module is prese…

Data sheet specifications Agilent 34970 A (2) [13]

Modules Specifications

The Agilent 34970A accuracy specifications already include the switching offset and reference junction errors shown below. These errors are listed separately for determining system error with external measurement devices.

Up to three modules, in any combination, can be inserted into a single mainframe. The 34970A's internal DMM connections are accessible only through the 34901A, 34902A, and 34908A low-frequency multiplexers.

On-module screw terminals accept wire sizes from 16 gage to 22 gage. Twenty-gage wire is recommended for high channel count applications. The 34905A and 34906A RF Multiplexers use SMB connectors. A standard set of (10) BNC-to-SMB adapter cables is provided with each RF module for convenient BNC connections.

		Multiplexer			Actuator	Matrix	RF Multiplexer		Multifunction
		34901A	34902A[1]	34908A	34903A	34904A	34905A	34906A	34907A
General									
Number of Channels		20 + 2 2/4 wire	16 2/4 wire	40 1 wire	20 SPDT	4 x 8 2 wire	Dual 1 x 4 50 Ω	75 Ω	See page 22 for module specifications
Connects to Internal DMM		•	•	•					
Scanning Speed		60 ch/s	250 ch/s	60 ch/s					
Open/Close Speed		120/s	120/s	70/s	120/s	120/s	60/s		
Input									
Voltage (dc , ac rms)[2]		300 V	300 V	300 V	300 V	300 V	42 V		
Current (dc , ac rms)		1A	50mA	1A	1A	1A	0.7A		
Power (W , VA)		50 W	2 W	50 W	50 W	50 W	20 W		
DC Characteristics									
Offset Voltage [3]		< 3uV	< 6uV	< 3uV	< 3uV	< 3uV	< 6uV		
Initial Closed Channel R [3]		< 1 Ω	< 1 Ω	< 1 Ω	< 0.2 Ω	< 1 Ω	< 0.5 Ω		
Isolation ch-ch, ch-earth		> 10 G Ω	> 10 G Ω	> 10 G Ω	> 10 G Ω	> 10 G Ω	> 1 G Ω		
AC Characteristics									
Bandwidth[4]		10 MHz	10 MHz	10 MHz	10 MHz	10 MHz	2 GHz [5]	2 GHz [5]	
Insertion Loss (dB)	10 MHz	—	—	—	—	—	-0.1	-0.1	
	100 MHz	—	—	—	—	—	-0.4	-0.4	
	500 MHz	—	—	—	—	—	-0.6	-0.5	
	1 GHz	—	—	—	—	—	-1	-1	
	1.5 GHz	—	—	—	—	—	-1.2	-1.5	
	2 GHz	—	—	—	—	—	-3	-2	
SWR	10 MHz	—	—	—	—	—	1.02	1.02	
	100 MHz	—	—	—	—	—	1.05	1.05	
	500 MHz	—	—	—	—	—	1.20	1.25	
	1 GHz	—	—	—	—	—	1.20	1.40	
	1.5 GHz	—	—	—	—	—	1.30	1.40	
	2 GHz	—	—	—	—	—	1.40	2.00	
ch-ch Cross Talk (dB)[4]	10 MHz	-45	-45	-18[6]	-45	-33	-100	-85	
	100 MHz	—	—	—	—	—	-85	-75	
	500 MHz	—	—	—	—	—	-65	-65	
	1 GHz	—	—	—	—	—	-55	-50	
	1.5 GHz	—	—	—	—	—	-45	-40	
	2 GHz	—	—	—	—	—	-35	-35	
Risetime							< 300 ps		
Signal Delay							< 3 ns		
Capacitance	HI - LO	< 50 pF	< 50 pF	< 50 pF	< 10 pF	< 50 pF	< 20 pF		
	LO - Earth	< 80 pF	< 80 pF	< 80 pF	< 80 pF	< 80 pF	—		
Volt-Hertz limit		10^8	10^8	10^8	10^8	10^8	10^{10}		
Other									
T/C Cold Junction Accuracy[3]	(typical)	0.8°C	0.8°C	0.8°C[8]					
Switch Life	No Load (typical)	100M	100M	100M	100M	100M	5M	5M	
	Rated Load (typical)[7]	100k	100k	100k	100k	100k	100k	100k	
Temperature	Operating	all cards — 0°C to 55°C							
	Storage	all cards — -20°C to 70°C							
Humidity	(non-condensing)	all cards — 40°C/80% RH							

[1] Not recommended for connection to ac line without external transient suppression
[2] Channel-to-channel or channel-to-earth
[3] Errors included in DMM measurement accuracy specifications
[4] 50Ω source, 50Ω load
[5] [illegible]
[6] Isolation within channel 1 to 20 or 21 to 40 banks is -40 dB
[7] Applies to resistive loads only
[8] Thermocouple measurements not recommended with 34908A module due to common lo configuration

Data sheet specifications Agilent 34970 A (3) [13]

12-Bit E Series Multifunction DAQ Specifications

Specifications – NI 607xE, NI 6062E, NI 6040E, NI 602xE

These specifications are typical for 25 °C unless otherwise noted.

Analog Input

Input Characteristics

Number of Channels

6070E	16 single-ended or 8 differential (software selectable per channel)
6062E	
6040E	
602xE	
6071E	64 single-ended or 32 differential (software selectable per channel)

Resolution .... 12 bits, 1 in 4,096

Maximum Sampling Rate

607xE	1.25 MS/s
6062E	500 kS/s
6040E	500 kS/s single-channel scanning 250 kS/s multichannel scanning
6023E	200 kS/s
6024E	
6025E	
6020E	100 kS/s

Input Signal Ranges

Device	Range (Software Selectable)	Bipolar Input Range	Unipolar Input Range
607xE	20 V	±10 V	–
6062E	10 V	±5 V	0 to 10 V
6040E	5 V	±2.5 V	0 to 5 V
6020E	2 V	±1 V	0 to 2 V
	1 V	±500 mV	0 to 1 V
	500 mV	±250 mV	0 to 500 mV
	200 mV	±100 mV	0 to 200 mV
	100 mV	±50 mV	0 to 100 mV
6023E	20 V	±10 V	–
6024E	10 V	±5 V	–
6025E	1 V	±500 mV	–
	100 mV	±50 mV	–

Input coupling .... DC

Maximum working voltage
(signal + common mode) .... Input should remain within ±11 V of ground

Overvoltage Protection

Device	Powered On	Powered Off
607xE	±25 V	±15 V
6062E		
6040E		
6023E	±40 V	±25 V
6024E		
6025E		
6020E	±35 V	±25 V

Inputs Protected

6070E	AI <0..15>, AI SENSE
6062E, 6040E	
602xE	
6071E	AI <0..63>, AI SENSE, AI SENSE2

FIFO Buffer Size

DAQCard-6062E	8,192 samples
DAQPad-6020E	4,096 samples
DAQPad-6070E	2,048 samples
DAQCard-6024E	
PCI/PXI-6070E	512 samples
6071E, 6040E	
PCI-6023E, NI 6025E, PCI-6024E	

Data transfers
PCI, PXI, DAQPad for FireWire .... DMA, interrupts, pr
DAQCard, DAQPad for USB...................... Interrupts, programi

DMA modes
PCI, PXI, DAQPad for FireWire .... Scatter-gather (sing

Configuration memory size .... 512 words

Transfer Characteristics

Relative Accuracy

Device	Typical Dithered	Maximum Undithered
607xE	±0.5 LSB	±1.5 LSB
6062E		
6040E		
6023E		
6024E		
6025E		
6020E	±0.2 LSB	±1.5 LSB

DNL

Device	Typical	Maximum
607xE	±0.5 LSB	±1.0 LSB
6040E		
6023E		
PCI-6024E		
6025E		
6020E	±0.2 LSB	±1.0 LSB
6062E	±0.75 LSB	-0.9, +1.5 LSB
DAQCard-6024E		

Data sheet specifications NI PCI 6023E (1) [13]

12-Bit E Series Multifunction DAQ Specifications

Specifications – NI 607xE, NI 606xE, NI 6040E, NI 602xE (continued)

Amplifier Characteristics

Input Impedance

Device	Normal Powered On	Powered Off	Overload
6070E 6062E 6040E PCI-6071E PXI-6071E	100 GΩ in parallel with 100 pF	820 Ω	820 Ω
6023E, 6024E, 6025E	100 GΩ in parallel with 100 pF	4.7 kΩ	4.7 kΩ
6020E	100 GΩ in parallel with 50 pF	3 kΩ	3 kΩ

Input bias current .... ±200 pA
Input offset current .... ±100 pA

CMRR, DC to 60 Hz

Device	Range	CMRR (dB)
607xE	20 V	95
	10 V	100
	100 mV to 5 V	106
6040E 6062E	10 to 20 V	85
	5 V	95
	100 mV to 2 V	100
6023E 6024E 6025E	10 to 20 V	85
	100 mV to 1 V	90
6020E	100 mV to 20 V	90

Dynamic Characteristics

Bandwidth

Device	Small Signal (-3 dB)	Large Signal (1% THD)
607xE	1.6 MHz	1 MHz
6062E	1.3 MHz	250 kHz
6040E	600 kHz	350 kHz
6023E PCI-6024E 6025E	500 kHz	225 kHz
DAQCard-6024E	500 kHz	265 kHz
DAQPad-6020E	150 kHz	200 kHz

Settling Time to Full-Scale Step

Device	Range	Accuracy ±0.012% (±0.5 LSB)	Accuracy ±0.024% (±1 LSB)	Accuracy ±0.098% (±4 LSB)
6070E	20 V	2 μs typical 3 μs maximum	1.5 μs typical 2 μs maximum	1.5 μs typical 2 μs maximum
	10 V	2 μs typical 3 μs maximum	1.5 μs typical 2 μs maximum	1.3 μs typical 1.5 μs maximum
	200 mV to 5 V	2 μs typical 3 μs maximum	1.5 μs typical 2 μs maximum	0.9 μs typical 1 μs maximum
	100 mV	2 μs typical 3 μs maximum	1.5 μs typical 2 μs maximum	1 μs typical 1.5 μs maximum
6071E	20 V	3 μs typical 5 μs max	1.9 μs typical 2.5 μs maximum	1.9 μs typical 2 μs maximum
	10 V	3 μs typical 5 μs maximum	1.9 μs typical 2.5 μs maximum	1.2 μs typical 1.5 μs maximum
	200 mV to 5 V	3 μs typical 5 μs maximum	1.9 μs typical 2.5 μs maximum	1.2 μs typical 1.3 μs maximum
	100 mV	3 μs typical 5 μs maximum	1.9 μs typical 2.5 μs maximum	1.2 μs typical 1.5 μs maximum
6062E	All	2.5 μs typical 4 μs maximum	2.5 μs typical 3 μs maximum	2 μs typical 2.5 μs maximum
	All	4 μs typical 8 μs maximum	4 μs maximum	4 μs maximum
	All	5 μs typical	5 μs maximum	5 μs maximum
	All	10 μs maximum	10 μs maximum	10 μs maximum

System Noise (LSB_{rms}, Not Including Quantization)

Device	Range	Dither Off	Dither On
6070E 6071E	1 to 20 V	0.25	0.5
	500 mV	0.4	0.6
	200 mV	0.5	0.7
	100 mV	0.8	0.9
6062E	1 to 20 V	0.25	0.6
	500 mV	0.4	0.75
	200 mV	0.5	0.8
	100 mV	0.8	1.0
6040E	1 to 20 V	0.2	0.5
	500 mV	0.25	0.5
	200 mV	0.5	0.7
	100 mV	0.9	1.0
6023E PCI-6024E, 6025E	1 to 20 V	0.1	0.6
	100 mV	0.7	0.8
DAQCard-6024E	10 to 20 V	0.1	0.65
	1 V	0.45	0.65
	100 mV	0.70	0.90
6020E	1 to 20 V	0.07	0.5
	500 mV	0.12	0.5
	200 mV	0.25	0.6
	100 mV	0.5	0.7

Crosstalk, DC to 100 KHz

Device	Adjacent Channels	All Other Channels
607xE, 6062E, 6040E	-75 dB	-90 dB
602xE	-60 dB	-80 dB

Data sheet specifications NI PCI 6023E (2) [13]

12-Bit E Series Multifunction DAQ Specifications

Specifications – NI 607xE, NI 606xE, NI 6040E, NI 602xE (continued)

Analog Output

Output Characteristics

	Number of Channels
607xE 6062E 6040E 6020E 6024E 6025E	2 voltage outputs
6023E	None

Resolution .... 12 bits, 1 in 4,096

Maximum update rate

	Waveform Generation			
	FIFO Mode		Non-FIFO Mode	
Device	Internally Timed	Externally Timed	1 Channel	2 Channels
607xE 6040E	1 MS/s	950 kS/s	800 kS/s, system dependent	400 kS/s, system dependent
6062E	850 kS/s	850 kS/s	800 kS/s, system dependent	400 kS/s, system dependent
6023E PCI-6024E 6025E	N/A	N/A	10 kS/s with DMA 1 kS/s with interrupts system dependent	10 kS/s with DMA 1 kS/s with interrupts system dependent
DAQCard-6024E	N/A	N/A	1 kS/s with interrupts system dependent	1 kS/s with interrupts system dependent
DAQPad-6020E	N/A	N/A	20 S/s, system dependent	20 S/s, system dependent

	FIFO Buffer Size
607xE, 6062E	2,048 samples
6040E	512 samples
602xE	None

Data transfers
- PCI, PXI, DAQPad for IEEE 1394 .... DMA, interrupts, programmed I/O
- DAQCard, DAQPad for USB .... Interrupts, programmed I/O

DMA modes
- PCI, PXI, DAQPad .... Scatter-gather (single transfer, demand transfer)

Transfer Characteristics

Relative accuracy
- After calibration
  - 6062E, DAQCard-6024E .... ±0.5 LSB typical, ±1.0 LSB maximum
  - All others .... ±0.3 LSB typical, ±0.5 LSB maximum
- Before calibration .... ±4 LSB maximum

DNL
- After calibration
  - 6062E, DAQCard-6024E .... ±0.5 LSB typical, ±1.0 LSB maximum
  - All others .... ±0.3 LSB typical, ±1.0 LSB maximum
- Before calibration .... ±3 LSB maximum

Monotonicity .... 12 bits, guaranteed after calibration

Gain error (relative to external reference)
- 6062E, 6020E .... ±0.5% of output maximum, not adjustable
- 607xE, 6040E .... 0 to 0.67% of output maximum, not adjustable

Voltage Output

Output coupling .... DC

Output impedance .... 0.1 Ω maximum

	Ranges
607xE, 6040E, 6020E	±10 V, 0 to 10 V, ±EXT REF, 0 to EXT REF; software selectable
6062E	±10 V, ±EXT REF, software selectable
6024E, 6025E	±10 V

Current drive .... ±5 mA maximum

Protection .... Short-circuit to ground

Power-on state .... 0 V (±200 mV)

External Reference Input

- Range .... 11 V
- Overvoltage protection
  - 607xE, 6062E, 6040E .... ±25 V powered on, ±15 V powered off
  - 6020E .... ±35 V powered on, ±25 V powered off
- Input impedance .... 10 kΩ
- Bandwidth (-3 dB)
  - 607xE, 6040E .... 1 MHz
  - 6062E .... 50 kHz
  - 6020E .... 300 kHz

Dynamic Characteristics

Device	Settling Time for Full-Scale Step	Slew Rate
607xE 6062E 6040E	3 μs to ±0.5 LSB accuracy	20 V/μs
602xE	10 μs to ±0.5 LSB accuracy	10 V/μs

Device	Reglitching Disabled	Reglitching Enabled
607xE, 604xE	±20 mV	±4 mV
PCI-6024E 6025E	±42 mV	N/A
DAQCard-6024E	±13 mV	N/A
6020E	±100 mV	N/A
6062E	±80 mV	±30 mV

	Glitch Duration (At Mid-Scale Transition)
607xE 6040E	1.5 μs
6024E 6025E	2 μs
6020E 6062E	3 μs

Noise .... 200 μV_{rms}, DC to 1 MHz

Glitch energy magnitude (at mid-scale transition)

Stability

Gain temperature coefficient (except 6024E, 6025E)
- External reference .... ±25 ppm/°C

National Instruments • Tel: (800) 433-3488 • info@ni.com • ni.com 7

Data sheet specifications NI PCI 6023E (3) [13]

High-Performance GPIB Interfaces for PCI and PXI

Specifications

IEEE 488 Compatibility

IEEE 488.1 and IEEE 488.2 compatible

Capability Code	Description
SH1	Source Handshake
AH1	Acceptor Handshake
T5, TE5	Talker, Extender Talker
L3, LE3	Listener, Extender Listener
SR1	Service Request
PP1, PP2	Local/Remote Parallel Poll
RL1	Remote/Local
C1, C2, C3, C4, C5	Controller
E1, E2	Three-state bus drivers with automatic switch to open collector during parallel poll

Maximum IEEE 488 Bus Transfer Rates

IEEE 488 interlocked handshake .... 1.5 MB/s
IEEE 488 noninterlocked
(HS488) handshake .... 7.7 MB/s
(Actual rates depend on system configuration and instrument capabilities.)

GPIB Analyzer Performance

Sampling rate .... 20 MHz
Timestamp resolution .... 50 ns

Ethernet Performance

10BaseT .... 10 Mb/s, full-duplex
100BaseTX .... 100 Mb/s, full-duplex
1000BaseT .... 1000 Mb/s, full-duplex

Power Requirements

PCI-GPIB, PXI-GPIB, PCI-GPIB/LP (183617x-01-based board)
+5 VDC .... 1.5 W typical, 2.25 W maximum
PCI-GPIB, PXI-GPIB (188513x-01-based board)
+3.3 VDC .... 0.4 W typical, 0.6 W maximum
PCI-GPIB+
+5 VDC .... 2.5 W typical, 3.75 W maximum
PCI-8232
+5 VDC .... 4.4 W typical, 5.8 W maximum
PXI-8232
+3.3 VDC .... 3.0 W typical, 4.0 W maximum
PCI signaling level .... Universal

Physical Dimensions

PCI (183617x-01-based board) .... 13.3 by 10.7 cm (5.3 by 4.2 in.)
PCI (188513x-01-based board) .... 12.0 by 6.44 cm (4.72 by 2.54 in.)
PCI (Low Profile) .... 12.0 by 6.44 cm (4.72 by 2.54 in.)
PXI .... 16 by 10 cm (6.3 by 3.9 in.)

I/O Connectors

GPIB .... IEEE 488 standard 24 pin
Ethernet RJ45

Operating Environment

Ambient temperature .... 0 to 55 °C
Relative humidity .... 10 to 90%, noncondensing

Storage Environment

Ambient temperature .... -20 to 70 °C
Relative humidity .... 5 to 95%, noncondensing

Compliance

Online at ni.com/compliance

Data sheet specifications PCI GPIB (1) [13]

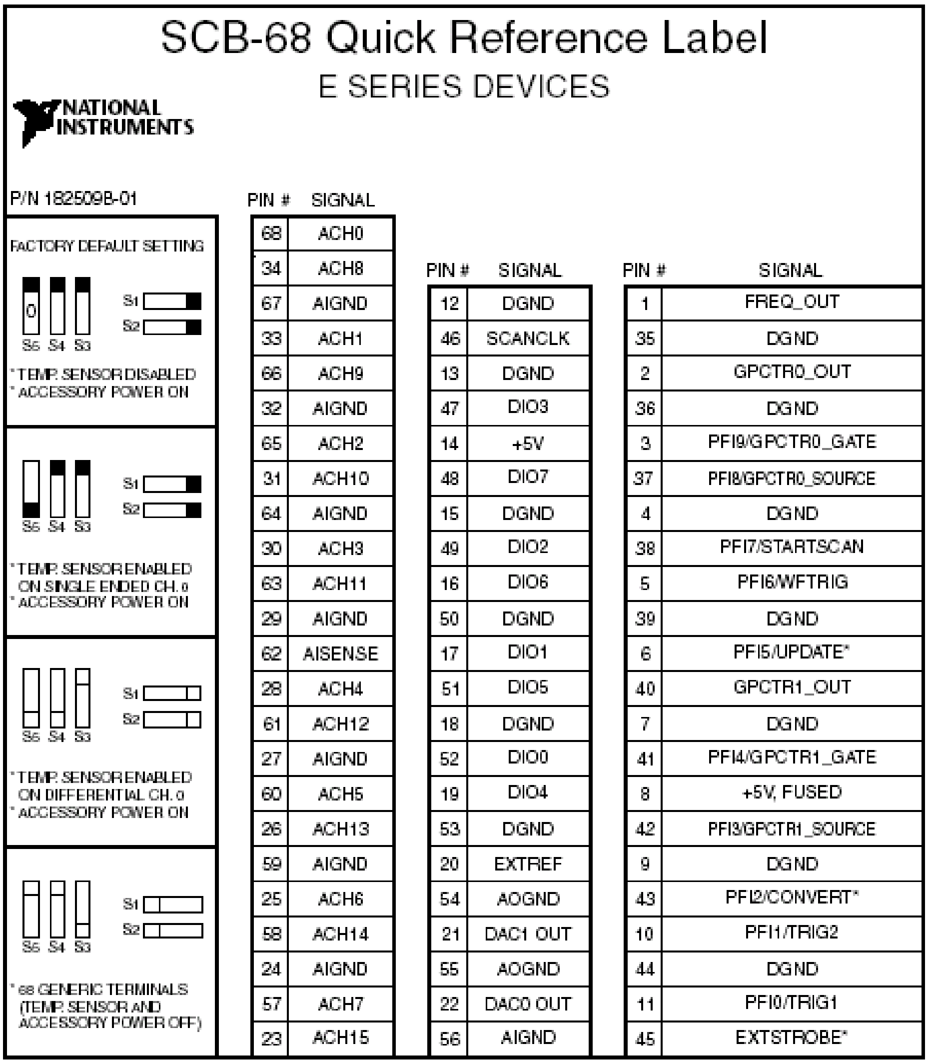

PIN #	SIGNAL
68	ACH0
34	ACH8
67	AIGND
33	ACH1
66	ACH9
32	AIGND
65	ACH2
31	ACH10
64	AIGND
30	ACH3
63	ACH11
29	AIGND
62	AISENSE
28	ACH4
61	ACH12
27	AIGND
60	ACH5
26	ACH13
59	AIGND
25	ACH6
58	ACH14
24	AIGND
57	ACH7
23	ACH15

PIN #	SIGNAL
12	DGND
46	SCANCLK
13	DGND
47	DIO3
14	+5V
48	DIO7
15	DGND
49	DIO2
16	DIO6
50	DGND
17	DIO1
51	DIO5
18	DGND
52	DIO0
19	DIO4
53	DGND
20	EXTREF
54	AOGND
21	DAC1 OUT
55	AOGND
22	DAC0 OUT
56	AIGND

PIN #	SIGNAL
1	FREQ_OUT
35	DGND
2	GPCTR0_OUT
36	DGND
3	PFI9/GPCTR0_GATE
37	PFI8/GPCTR0_SOURCE
4	DGND
38	PFI7/STARTSCAN
5	PFI6/WFTRIG
39	DGND
6	PFI5/UPDATE*
40	GPCTR1_OUT
7	DGND
41	PFI4/GPCTR1_GATE
8	+5V, FUSED
42	PFI3/GPCTR1_SOURCE
9	DGND
43	PFI2/CONVERT*
10	PFI1/TRIG2
44	DGND
11	PFI0/TRIG1
45	EXTSTROBE*

SCB 68 E series I/O connector Pinout [13]

Appendix D

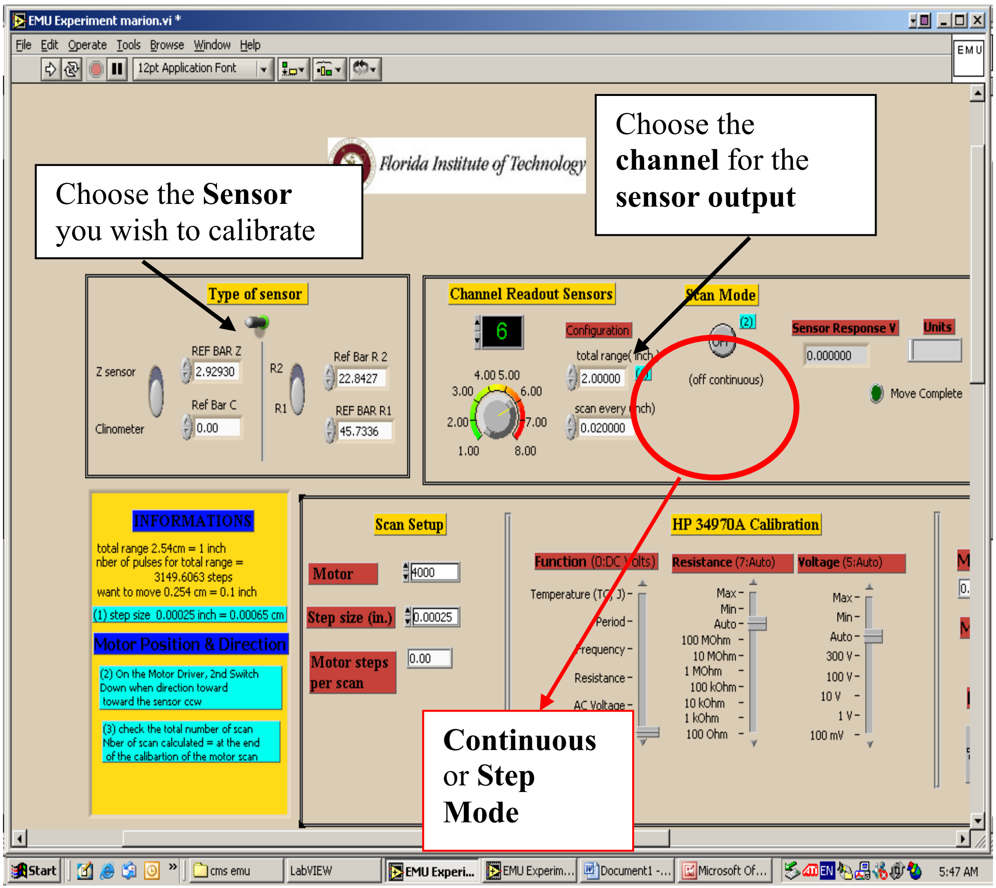

Front Panel of CMS EMU.VI (1)

Appendix E

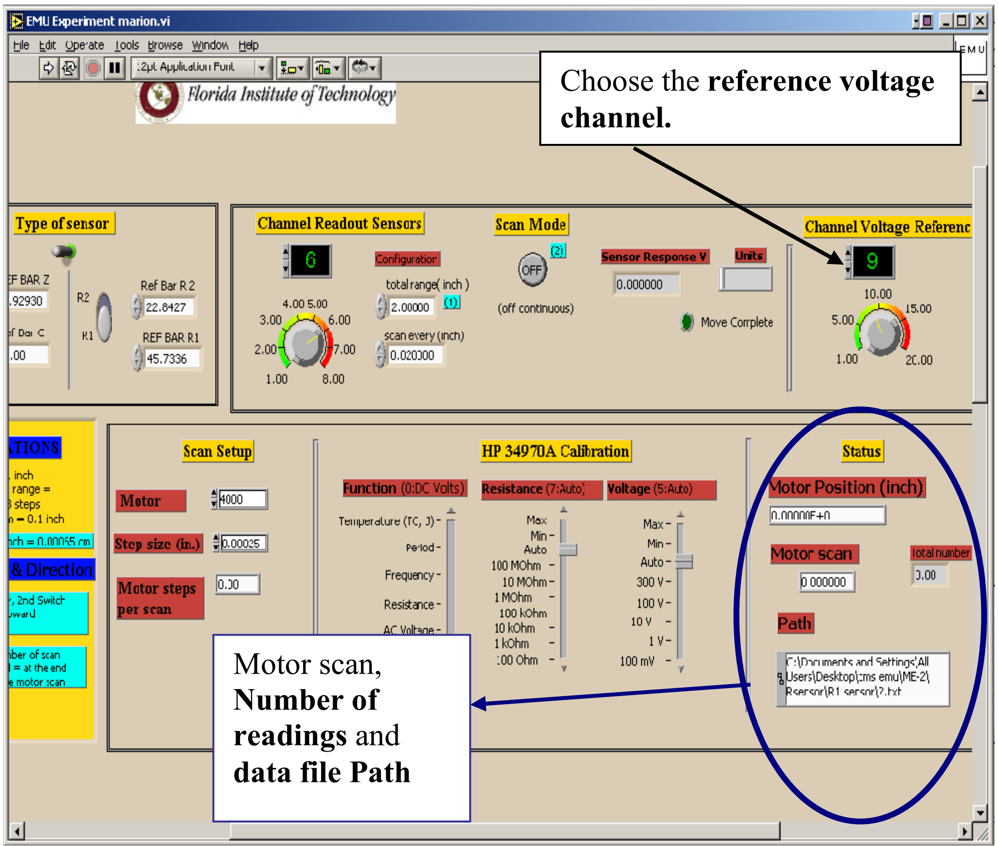

Front Panel of CMS EMU.VI (2)

Appendix F

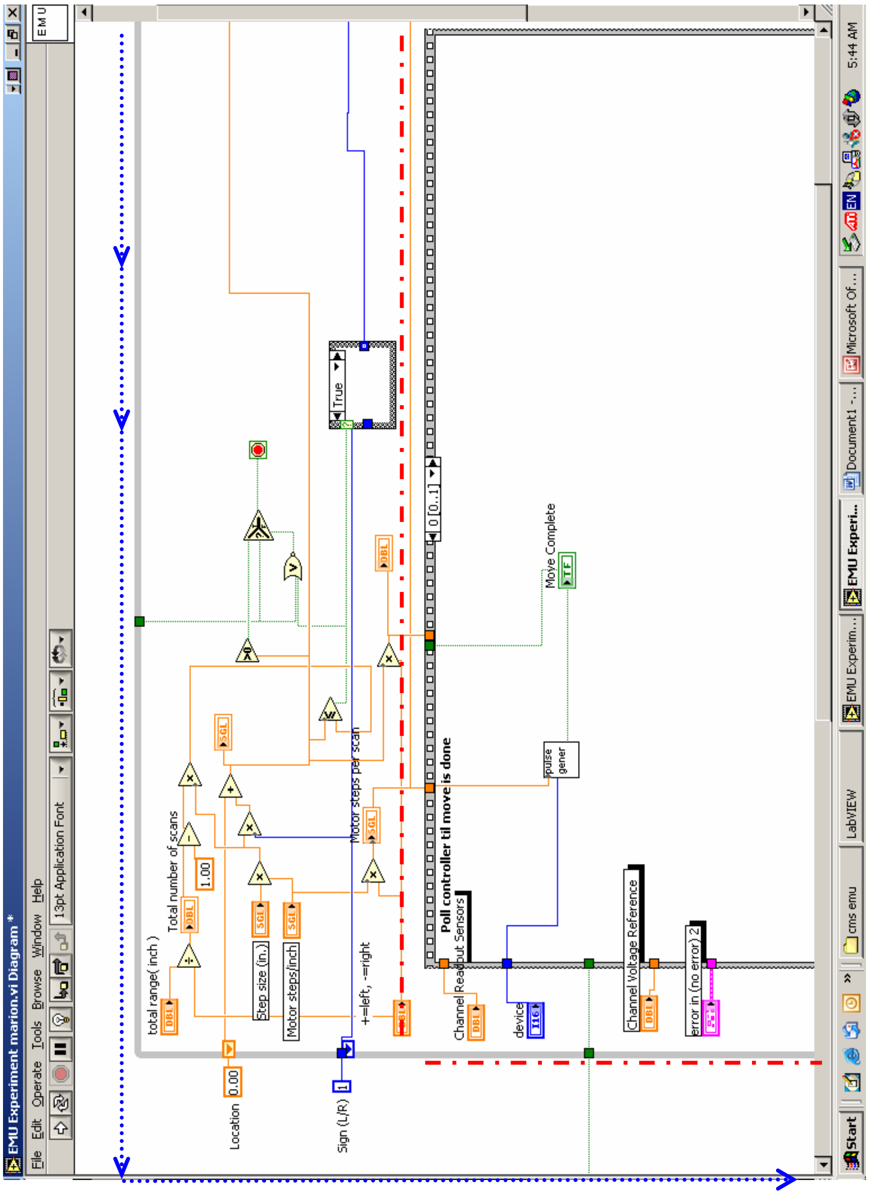

Diagram Panel for CMS EMU.VI

First sequence – Control of Stepper Motor

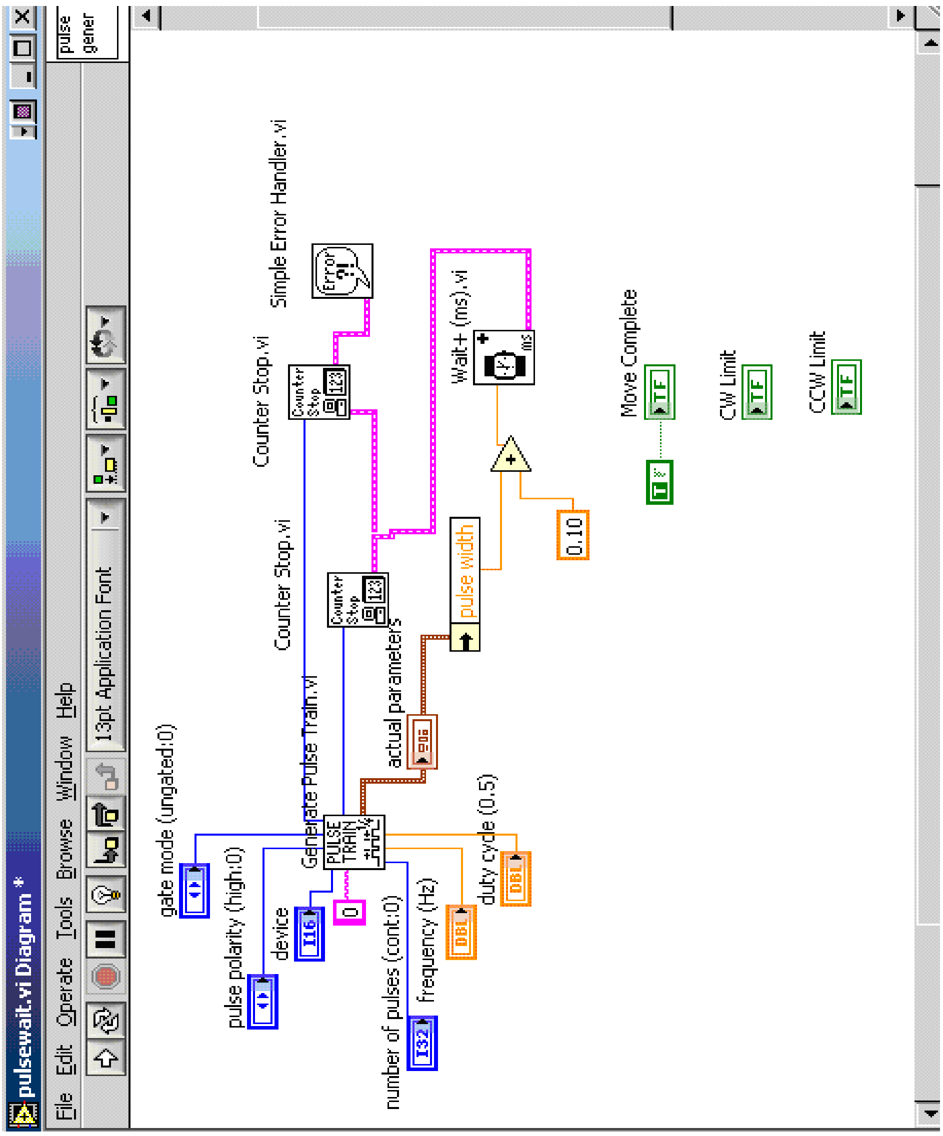

Diagram Panel for CMS EMU.VI

Details of the subvi called “ Pulse wait.vi”

Appendix G

Procedure Manual

Type of sensor

1st horizontal switch

	Left side for clinometer and Z sensor right side for the R1 and R2 sensors

2nd vertical switch: choose between

the two R sensors or
the Clinometer and the z sensor

	R1 sensor	R2 sensor	R2 Tower	Z1 sensor	Z2 sensor	Clinometer x	Clinometer y
Total Range inch	2.8	3.6	3.8	0.52	0.52	0.4	0.4
Scan every inch	0.02	0.02	0.02	0.005	0.005	0.004	0.004
Channel sensor	106	108	108	103	105	101	102
Channel Reference Voltage	107	109	109	104	104***	104*	104*

SCAN MODE swicth OFF

Motor Direction : Motor Controller --> 2nd switch up direction toward the motor (ccw)

	R1 sensor	R2 sensor	R2 Tower	Z1 sensor	Z2 sensor
Path	C:\Documents and Settings\All Users\Desktop\cms emu\ME-2\Rsensor\R1 sensor	C:\Documents and Settings\All Users\Desktop\cms emu\ME-2\Rsensor\R2 sensor	C:\Documents and Settings\All Users\Desktop\cms emu\ME-2\Rsensor\Tower	C:\Documents and Settings\All Users\Desktop\cms emu\ME-2\Zsensor\z1 SENSO	C:\Documents and Settings\All Users\Desktop\cms emu\ME-2\Zsensor\z2 SENSOR

Don't forget to add " \Foldername\File Name".txt (*)

RUN -->

End of the scan

SCAN MODE **Switch ON**

Change the direction of the motor : 2nd switch down

Change 'scan every (inch)' to = 'total range inch'

Change the Path File Name for each new sensor
Change the Text File Name for each new trial
Folder Name for example ME-2114-AN-OR
(*) label as " the Numbers on the plate".txt- for example : Trial1ME-2114-AN-OR.txt
>>>> Add ME-2114-AN-OR/Trial1ME-2114-AN-OR.TXT

NOTE Each sensors have to be calibrated 5 times. For each calibration, you have to check the absolute distance with the reference bar!

Remark :

- R2 tower range changed to 3.8 (from 2.2)
- R2 sensor range changed to 3.6 (from2.2)
- R2 sensor range changed to 3.6 (from2)
- *** keep Z1 connected during scan
- * with z sensor connected

Appendix H

Tolerance in the dowel hole/pin for R2 Tower sensors

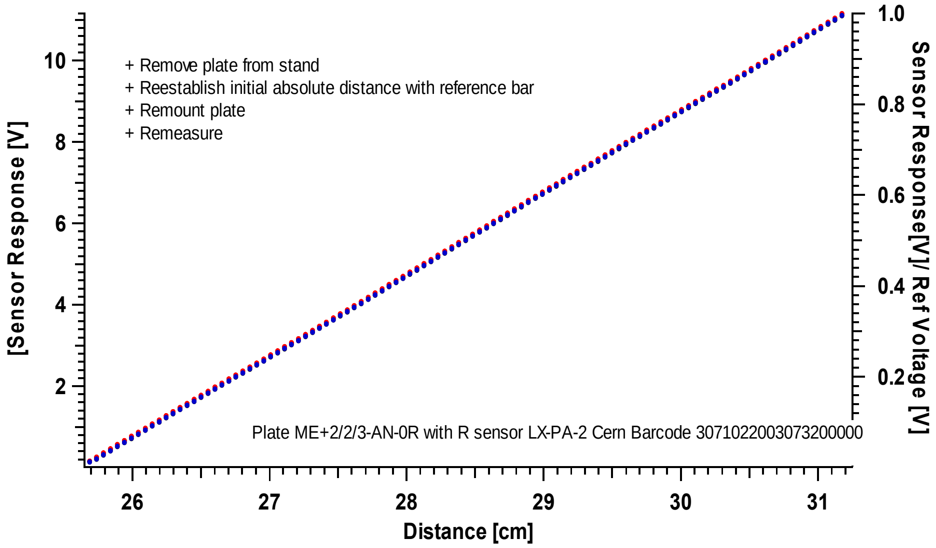

3 out of 30 trials of : Sensor Response vs. Distance for R2 Tower

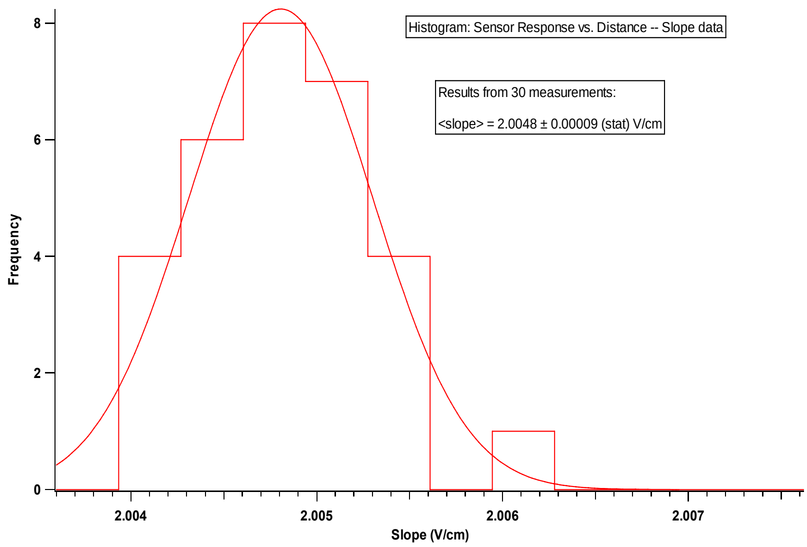

Histogram of 30 trials of the slope of the graph: Sensor Response vs. Distance.

$$\frac{\sigma < slope >}{< slope >} = 0.0045\%$$

$$\sigma_{\Delta x} = 2.46\mu m \ over \ a \ \ full \ range \ (50mm)$$

$$With \ 5 \ calibration \ measurements \ \ per \ \ sensor:$$

$$\rightarrow \sigma_{\Delta x} = 2.46 * \sqrt{\frac{30}{5}} = 6\mu m \ over \ a \ \ full \ range \ (50mm)$$

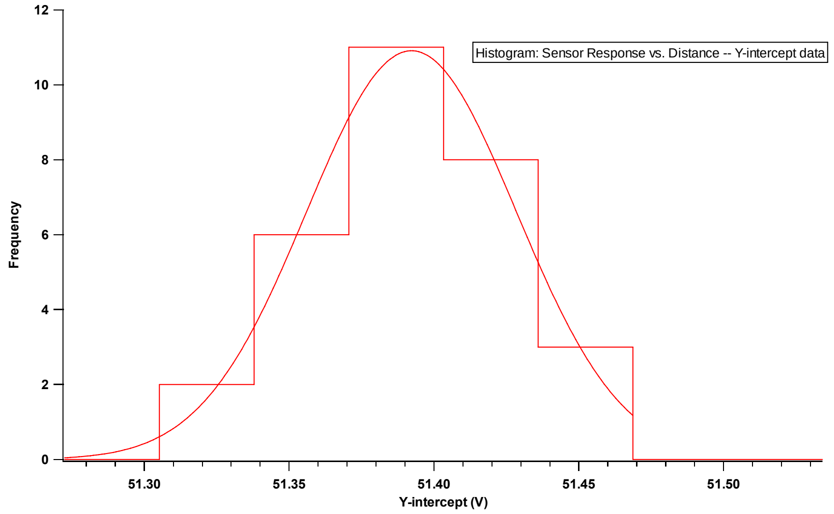

Histogram of 30 trials of the Y-intercept of the graph: Sensor Response vs. Distance.

$$\sigma(y - \text{int}\, cpt) = 0.036V$$

$$and < slope >= 2.0048V / cm$$

$$\rightarrow \sigma(x) = \frac{0.036V}{2.0048V / cm} 10^4 = 180\mu m$$